DESIGN, MODELING, AND OPTIMAL CONTROL ALLOCATION OF A HEAVY-LIFT AERIAL VEHICLE CONSISTING OF LARGE AND SMALL TILT-ROTORS

A THESIS SUBMITTED TO
THE GRADUATE SCHOOL OF NATURAL AND APPLIED SCIENCES
OF
MIDDLE EAST TECHNICAL UNIVERSITY

BY

GÖKHAN ÖZDOĞAN

IN PARTIAL FULFILLMENT OF THE REQUIREMENTS
FOR
THE DEGREE OF DOCTOR OF PHILOSOPHY
IN
ELECTRICAL AND ELECTRONICS ENGINEERING

SEPTEMBER 2021

Approval of the thesis:

DESIGN, MODELING, AND OPTIMAL CONTROL ALLOCATION OF A HEAVY-LIFT AERIAL VEHICLE CONSISTING OF LARGE AND SMALL TILT-ROTORS

submitted by **GÖKHAN ÖZDOĞAN** in partial fulfillment of the requirements for the degree of **Doctor of Philosophy in Electrical and Electronics Engineering Department, Middle East Technical University** by,

Prof. Dr. Halil Kalıpçılar
Dean, Graduate School of **Natural and Applied Sciences** _____

Prof. Dr. İlkay Ulusoy
Head of Department, **Electrical and Electronics Engineering** _____

Prof. Dr. Kemal Leblebicioğlu
Supervisor, **Electrical and Electronics Engineering, METU** _____

Examining Committee Members:

Assist. Prof. Dr. Yakup Özkazanç
Electrical and Electronics Engineering, Hacettepe University _____

Prof. Dr. Kemal Leblebicioğlu
Electrical and Electronics Engineering, METU _____

Prof. Dr. Mehmet Önder Efe
Computer Engineering, Hacettepe University _____

Assoc. Prof. Dr. İlkay Yavrucuk
Aerospace Engineering, METU _____

Assist. Prof. Dr. Mustafa Mert Ankaralı
Electrical and Electronics Engineering, METU _____

Date: 06.09.2021

I hereby declare that all information in this document has been obtained and presented in accordance with academic rules and ethical conduct. I also declare that, as required by these rules and conduct, I have fully cited and referenced all material and results that are not original to this work.

Name, Surname: Gökhan Özdoğan

Signature :

ABSTRACT

DESIGN, MODELING, AND OPTIMAL CONTROL ALLOCATION OF A HEAVY-LIFT AERIAL VEHICLE CONSISTING OF LARGE AND SMALL TILT-ROTORS

Özdoğan, Gökhan
Ph.D., Department of Electrical and Electronics Engineering
Supervisor: Prof. Dr. Kemal Leblebicioğlu

September 2021, 129 pages

We propose an unconventional heavy lifting aerial vehicle (HLAV), present the design and its control allocation analysis, and prove the concept by demonstration of the experimental test prototype in the outdoor environment. We aimed for a mechanically robust and simple vehicle design that efficiently performs heavy lifting compared to other common aerial vehicles under certain width constraints, without using a complex swashplate mechanism. The HLAV performs the task of carrying the main load with two large propellers that are efficient thanks to the greater disk area, and includes two small tilting propellers for controllability. This system has a "PPNN" (P: Clockwise, N: Counterclockwise) propeller arrangement to compensate for the reaction torques of equally sized propeller pairs placed on opposite sides. However, conventional quadcopters with the "PPNN" propeller arrangement lose their controllability upon hovering. Therefore, to ensure controllability, servo motors are integrated into the small propellers giving them the ability to tilt. The nonlinear dynamic model of the HLAV is built by the Newton-Euler approach, and the system is linearized around the hover equilibrium point, for controllability analysis. A control allocation strategy based on quadratic programming is developed to utilize HLAV capacity at maximum

performance with optimal power. Model parameters are estimated using closed-loop system identification tools. High-level controllers are designed with the “loop shaping” method.

Precise positioning of servo motors that are used in tilt mechanism, is a crucial parameter for reducing vibrations in the HLAV and improve overall flight performance. Due to size and weight limitations, the motor is required to be small but torque density is desired to be high. In high torque and inexpensive PMSM and BLDC motors, cogging torque and friction are usually the main challenging disturbance sources. Cogging torque and friction can be identified using position sensors that already exist in the tilt mechanism, so the cost of the system is not increased. We attack this problem by developing feedforward algorithms and show that with cogging torque compensation alone, 30-65% of the positional error can be removed in a feedback control system.

The proposed system, HLAV is experimentally tested and verified with a newly designed prototype. Sufficient trajectory tracking performance is achieved in a stable manner and the flight test results are presented.

Keywords: aerial robotics, design optimization, dynamic modeling, control allocation, tilt-rotor, cogging-torque, disturbance rejection

ÖZ

BÜYÜK VE KÜÇÜK PERVANELERDEN OLUŞAN AĞIR YÜK KALDIRAN HAVA ARACININ TASARIMI, MODELLENMESİ VE OPTİMAL KONTROL TAHSİSİ

Özdoğan, Gökhan
Doktora, Elektrik ve Elektronik Mühendisliği Bölümü
Tez Yöneticisi: Prof. Dr. Kemal Leblebicioğlu

Eylül 2021 , 129 sayfa

Bu tezde, yeni bir ağır yük kaldırma hava aracı (HLAV) tasarımı önerilmektedir, aracın modellenmesi ve kontrol tahsis analizi sunulmuştur. Deneysel bir prototip hazırlanmış ve uçuş testi ile HLAV konsepti kanıtlanmıştır. Alışılageldik helikopterlerde bulunan mekanik olarak karmaşık eğik plaka mekanizması kullanmadan, belirli genişlik kısıtlamaları altında diğer yaygın hava araçlarına kıyasla ağır kaldırma gücünü verimli bir şekilde gerçekleştiren sağlam, basit bir mekanik araç tasarımı hedefledik. HLAV, daha büyük disk alanı sayesinde verimli olan iki büyük pervane ile ana yükü taşıma görevini yerine getirir, ve kontrol edilebilirlik için iki küçük eğilebilen pervane içerir. Bu sistem, karşı taraflara yerleştirilmiş eşit büyüklükteki pervane çiftlerinin tepki torklarını telafi etmek için "PPNN" (P: Saat Yönünde, N: Saat yönünün tersine) pervane düzenine sahiptir. Bununla birlikte, "PPNN" pervane düzenine sahip geleneksel dört pervaneli robot helikopterler, havada asılı kalma durumunda kontrol edilebilirliklerini kaybederler. Bu nedenle, kontrol edilebilirliği sağlamak için servo motorlar, küçük pervanelere entegre edilerek onlara eğilme yeteneği kazandırılmıştır.

HLAV'ın doğrusal olmayan dinamik modeli Newton-Euler yaklaşımıyla oluşturulmuştur ve sistem kontrol edilebilirlik analizi için havada asılı kalma denge noktası etrafında doğrusallaştırılmıştır. HLAV kapasitesini optimum güçle maksimum performansta kullanmak için ikinci dereceden programlamaya dayalı bir kontrol tahsis stratejisi geliştirilmiştir. Model parametreleri, kapalı döngü sistem tanımlama araçları kullanılarak kestirilmiştir. Üst seviye kontrolcüler "döngü şekillendirme" yöntemi ile tasarlanmıştır.

Eğim mekanizmasında kullanılan servo motorların hassas yönlendirilebilmeleri, HLAV sistemindeki titreşimleri azaltmak ve genel uçuş performansını iyileştirmek için çok önemli bir parametredir. Boyut ve ağırlık sınırlamaları nedeniyle motorun küçük olması, ancak tork yoğunluğunun yüksek olması istenmektedir. Yüksek torklu ve ucuz PMSM ve BLDC motorlarda, vuruntu torku ve sürtünme genellikle başta gelen bozucu etkenlerdir. Vuruntu torku ve sürtünme, eğim mekanizmasında zaten mevcut olan konum sensörleri kullanılarak kestirilebilir, böylece sistemin maliyeti artmaz. Bu probleme, ileri beslemeli algoritmalar geliştirerek bir çözüm önerilmiştir ve sadece vuruntu tork kompanzasyonu ile, bir geri besleme kontrol sisteminde izleme hatasının %30-65'inin giderilebileceği gösterilmiştir.

Önerilen sistem, HLAV, deneysel olarak test edilmiş ve yeni tasarlanmış bir prototip ile doğrulanmıştır. Yeterli yörünge takibi performansı istikrarlı bir şekilde sağlanmıştır ve uçuş test sonuçları paylaşılmıştır.

Anahtar Kelimeler: hava robotiği, tasarım optimizasyonu, dinamik modelleme, kontrol tahsisi, eğimli-pervane mekanizması, vuruntu momenti, bozucu etki bastırma

To my parents

ACKNOWLEDGMENTS

I would like to express my deepest and sincerest gratitude to my supervisor, Prof. Dr. Kemal Leblebicioğlu for his guidance, understanding, insightful academic advice, and continuous support. His guidance on both my research and my career has been invaluable.

I am also very thankful to my thesis monitoring committee members, Assoc. Prof. Dr. İlkay Yavrucuk and Assist. Prof. Dr. Mustafa Mert Ankaralı for their critical comments, help, and encouragement throughout my study, and Prof. Dr. Mehmet Önder Efe and Assist. Prof. Dr. Yakup Özkazanç for their participation and contribution to the defense.

I am thankful to my colleagues at ASELSAN and ODTÜ; İsmail Çağdaş Yılmaz and Dr. Mehmet Baskın for numerous discussions and their part in building prototype system and throughout experimental tests; Emin Şen for helping with the 3-D mechanical design of tilt mechanism and main frame; Tuğçe Sözen for drone legs; Dr. Ferit Çakıcı for sharing experiences and advice; Raha Shabani, Akın Günönü and Murat Kalkan for all their support.

I would also like to thank my daughter, İlke, for being a loving and cheerful baby. And in the end, I owe everything to my beloved wife Sinem Sözen, who has always been by my side with her support. I wish her success in her thesis studies.

TABLE OF CONTENTS

ABSTRACT v

ÖZ vii

ACKNOWLEDGMENTS x

TABLE OF CONTENTS xi

LIST OF TABLES xv

LIST OF FIGURES xvi

LIST OF ALGORITHMS xx

LIST OF ABBREVIATIONS xxi

LIST OF SYMBOLS xxiii

CHAPTERS

1 INTRODUCTION 1

1.1 Motivation 1

1.2 Proposed System and Methods 2

1.3 Discussion: HLAV Efficiency Comparison Using Momentum Theory 5

1.4 Contributions and Novelties 10

1.5 The Outline of the Thesis 11

2 DYNAMIC SYSTEM MODELING 15

2.1 Notation and Definitions 15
2.2 Assumptions used in Modeling 16
2.3 6-DOF Rigid Body Dynamics 18
2.4 Nonlinear Model 24
3 LINEAR ANALYSIS AND SIMPLE CONTROL ALLOCATION DESIGN 27
3.1 Linearization 27
3.2 The Control Effectiveness Matrix 30
3.3 Simple Control Allocation 32
3.3.1 Pseudo-Inverse Control Allocation 32
3.3.2 Simplified Pseudo-Inverse Control Allocation 32
3.3.3 Results: General Forces and Moments 34
3.3.3.1 Force in z-axis 34
3.3.3.2 Roll torque 35
3.3.3.3 Pitch torque 35
3.3.3.4 Yaw torque 36
3.4 Autopilot and Simulation Results 36
4 ADVANCED CONTROL ALLOCATION DESIGN 43
4.1 Control System Structure 43
4.2 Control Allocation Algorithm 44
4.3 Quadratic Programming Control Allocation Implementation for HLAV 46
5 SYSTEM IDENTIFICATION AND HIGH LEVEL CONTROLLER DESIGN 55
5.1 Identification of Aerial Vehicle for High-Level Controller 55
5.2 High Level Controller Design 60

6 COGGING TORQUE DISTURBANCE REJECTION AND CONTROLLER DESIGN FOR SERVO MOTOR 65

6.1 Discussion 66

6.2 Experimental Test Setup 68

6.3 System Identification and Controller Design 69

6.3.1 Current Loop 69

6.3.2 Speed and Position Loop 70

6.4 Identification and Rejection of Cogging Torque 74

6.5 Identification and Rejection of Friction Torque 76

6.6 Conclusion 80

7 EXPERIMENTAL TESTS 81

7.1 Prototype Hardware 81

7.2 Experimental Test and Flight Results 88

8 CONCLUSION AND FUTURE WORK 101

8.1 Conclusion 101

8.2 Future Work 102

REFERENCES 105

APPENDICES

A CONTROLLABILITY ANALYSIS OF PPNN PROPULSOR ARRANGEMENT 113

A.1 Discussion 113

A.2 Controllability analysis with the classical method 114

A.2.1 Dynamic Model 115

A.2.2 Nonlinear Model 117

A.2.3 Linearization 121

A.3 Degree of Controllability 123

CURRICULUM VITAE 127

LIST OF TABLES

TABLES

Table 3.1 HLAV and propulsion system parameters used in simulation 37

Table 4.1 HLAV system parameters used in Control Allocation Analysis . . . 52

Table 6.1 Static friction parameters. 79

Table 7.1 Propulsion system 84

Table 7.2 Servo motor, FT5313M 86

Table A.1 System parameters 125

LIST OF FIGURES

FIGURES

Figure 1.1 HLAV: Proposed configuration with "PPNN" propeller arrangement 3

Figure 1.2 HLAV: Configuration overview 4

Figure 1.3 Configuration types 5

Figure 1.4 Comparison of hover efficiency (power loading) of the most common multi-copters and HLAV at the same weight using momentum theory under maximum width constraint, W. Parameters are normalized relative to single-rotor helicopter and sorted by efficiency. The methodology presented in [1] is followed. 7

Figure 2.1 HLAV: Proposed configuration with "PPNN" propeller arrangement 16

Figure 3.1 Trajectory tracking result 38

Figure 3.2 Angular velocity control 39

Figure 3.3 Attitude control 39

Figure 3.4 Linear velocity control 40

Figure 3.5 Position control 40

Figure 3.6 Brushless motor control (left: rad/s, right: throttle %) 41

Figure 3.7 Servo motor control 41

Figure 4.1 Control system structure 44

Figure 4.2 Attainable control set (ACS) in hover state, Blue: Pseudo-Inverse, Red: Quadratic programming. Volume is increased by (a) 4.4 times for the ACS cut at $F_z^N + mg = 0$, (b) 3.6 times for the ACS cut at $L = 0$, (c) 5.4 times for the ACS cut at $M = 0$, (d) 2.8 times for the ACS cut at $N = 0$ 53

Figure 5.1 Estimation data collected in closed loop control, input is rate command excitation signal and output is gyro measurement 58

Figure 5.2 FRF measurement and 3σ uncertainty. 59

Figure 5.3 Step responses of estimated parametric transfer function models . 59

Figure 5.4 Validation of closed loop model 60

Figure 5.5 Indirect approach and subspace method to estimate open loop system, with normalized magnitudes. 61

Figure 5.6 Inner rate loop control system structure. 61

Figure 5.7 Desired loop shape. 62

Figure 5.8 Bode Diagram of open loop system, $L = G \cdot C$ 63

Figure 5.9 Output disturbance sensitivity function of the feedback control system, $|1/(1 + L)|$ 63

Figure 6.1 Experimental test setup. 69

Figure 6.2 Open loop nonparametric FRF measurement Bode diagram. . . . 71

Figure 6.3 Control system structure. 72

Figure 6.4 Desired loop shape. 73

Figure 6.5 Bode Diagram of open loop system, GM = 14.5 dB (at 48.9 Hz), PM = 73.8 deg (at 9.3 Hz). 74

Figure 6.6 Output disturbance sensitivity function. 74

Figure 6.7 Cogging Torque Position Map, Left, cartesian plot, blue: backward, red: forward measurement. 76

Figure 6.8 Cogging Torque Position Map, Polar plot, blue: backward, red: forward measurement. 77

Figure 6.9 Anticogging performance test, tracking error when rate command is -1 deg/s. 78

Figure 6.10 Friction-velocity map and estimated static friction model, 98% fit. 79

Figure 7.1 Pixhawk 2 82

Figure 7.2 Thrust tests and parameter identification 85

Figure 7.3 Tilt-rotor servo motor mechanism from different perspectives . . 86

Figure 7.4 Servo Motor 86

Figure 7.5 Power board 87

Figure 7.6 The system used in field flight tests. A video showcasing is accompanied: `https://youtu.be/yRUwUlp7Ucc`. 90

Figure 7.7 Vehicle trajectory in NED frame (meters) 91

Figure 7.8 Position tracking in NED frame, x 91

Figure 7.9 Position tracking in NED frame, y 92

Figure 7.10 Position tracking in NED frame, z 92

Figure 7.11 Translational velocity tracking, V_x^N 93

Figure 7.12 Translational velocity tracking, V_y^N 93

Figure 7.13 Translational velocity tracking, V_z^N 94

Figure 7.14 Attitude tracking, Roll, ϕ 94

Figure 7.15 Attitude tracking, Pitch, θ 95

Figure 7.16 Attitude tracking, Yaw, ψ 95

Figure 7.17 Angular rate tracking, Roll, p 96

Figure 7.18 Angular rate tracking, Pitch, q 96

Figure 7.19 Angular rate tracking, Yaw, r 97

Figure 7.20 BLDC motor control throttle (throttle 1000 min, 2000 max) . . . 97

Figure 7.21 Servo tilt motor control (1000 min, 2000 max) 98

Figure 7.22 Battery 98

Figure 7.23 Power 99

Figure 7.24 PSD Estimate of linear vibrations on vehicle 99

Figure A.1 Previous version of HLAV Configuration - No tilt mechanism . . 114

Figure A.2 Left Figure: PNPN layout, Right Figure: PPNN layout 114

Figure A.3 PPNN Available Control Authority 126

LIST OF ALGORITHMS

ALGORITHMS

Algorithm 1 Search for maximum attainable control-set for pseudo-inverse allocation method 50

Algorithm 2 Search for maximum attainable control-set for quadratic-programming allocation method 51

LIST OF ABBREVIATIONS

ACS	Attainable control set
B-EMF	Back electromotive force
BLDC	Brushless direct current motor
CAD	Computer-aided design
CCW	Counter clockwise
CPU	Central processing unit
CW	Clockwise
DCM	Direction cosine matrix
DOF	Degrees of freedom
ECEF	Earth center earth fixed frame
ESC	Electronic speed control
FFT	Fast fourier transform
FRF	Frequency response function
GM	Gain margin
GNSS	Global navigation satellite system
GPS	Global positioning system
HLAV	Heavy-lifting aerial vehicle
IDE	Integrated development environment
IMU	Inertial measurement unit
LiPo	Lithium polymer
LP^1	Low-pass filter
LP^2	Linear programming
MAVLink	Micro air vehicle link

MTOW	Maximum takeoff weight
NED	North east down coordinate system
PI	Proportional derivative
PID	Proportional integral derivative
PM	Phase margin
PMSM	Permanent magnet synchronous motor
PNPN, PPNN	P: Clockwise, N: Counterclockwise - propeller arrangement
PSD	Power spectral density
PWM	Pulse width modulation
QP	Quadratic programming
RAM	Random-access memory
RF	Radio frequency
ROS	Robot operating system
RPM	Revolutions per minute
rms	root mean square value
SBEC	Switching battery eliminator circuit
SI	International system of units
SISO	Single input, single output
SNR	Signal-to-noise ratio
SSARX	Subspace identification based on autoregressive with exogenous variables modeling
UAV	Unmanned aerial vehicle
VTOL	Vertical take-off and landing

LIST OF SYMBOLS

DL	Disk loading
PL	Power loading
ρ	The density of air
$C_{s_1}^{s_2}$	Direction cosine matrix (DCM), that transforms one coordinate reference frame ("s_1"), to another ("s_2").
i-frame	The inertial frame, origin at the centre of the Earth, axes do not rotate relative to the stars.
e-frame	The Earth frame, origin at the centre of the Earth, axes are fixed with respect to the Earth.
n-frame	The navigation frame, origin at the centre of the navigation system of the vehicle, axes are aligned with the north, east and the local vertical (down).
b-frame	The body frame, axes are aligned with the roll, pitch and yaw axes of the vehicle.
h-frame	Hybrid frame of reference where vector elements can belong to different coordinate frames
$\mathbf{P}_{eb}^{e} = \mathbf{P}^{e} = [x,\, y,\, z]^{T}$	Translational position vector of vehicle in earth frame (for simplicity, subscripts are dropped).
$\mathbf{V}_{eb}^{e} = \mathbf{V}^{e} = [V_x,\, V_y,\, V_z]^{T}$	Translational velocity vector in earth frame
$\mathbf{V}_{eb}^{b} = \mathbf{V}^{b} = [u,\, v,\, w]^{T}$	Translational velocity vector in body frame
$\mathbf{\Theta} = [\phi,\, \theta,\, \psi]^{T}$	Angular position Euler angles forming a non-orthogonal vector, roll, pitch, and yaw respectively
$\mathbf{\Omega}_{ib}^{b} = [p,\, q,\, r]^{T}$	The angular velocity (orthogonal) of the b-frame relative to the i-frame, resolved in the b-frame (measured by the gyroscopes).
$(.)_i$	The i-th component of the vector in the expression.

$\mathbf{S}(.)$	The skew-symmetric operator.
m	Vehicle mass
$\mathbf{J} = \begin{bmatrix} I_{xx} & -I_{xy} & -I_{xz} \\ -I_{xy} & I_{yy} & -I_{yz} \\ -I_{xz} & -I_{yz} & I_{zz} \end{bmatrix}$	Body frame inertia matrix relative to the center of mass (for simplicity, superscript in $\mathbf{J}^b$ is dropped). The inertia matrix is time-invariant. When products of inertia terms are negligible, the inertia matrix consists only of diagonal elements
I_{xx}, I_{yy}, I_{zz}	Moments of inertia about (x, y, z) axes
I_{xy}, I_{yz}, I_{xz}	Products of inertia
ω_i	Angular speed of propeller i-th.
ξ_i	Tilt angle of servo motor i-th.
K_{t_b} / K_{t_s}	Thrust coefficient of big / small rotors ($N\,s^2/rad^2$)
K_{m_b} / K_{m_s}	Torque coefficient of big / small rotors ($Nm\,s^2/rad^2$).
d_b / d_s	Distance between big / small rotor and the body center (m).
$\boldsymbol{C}_\alpha$	$\cos(\alpha)$
$\boldsymbol{S}_\alpha$	$\sin(\alpha)$
$\boldsymbol{T}_\alpha$	$\tan(\alpha)$
$R_i(\alpha)$	Rotation matrix about one of the axes of a coordinate system ($i = x,\ y,\ z$) by an angle α.
$L,\ M,\ N$	Aerodynamic moments in the body frame acting on roll, pitch and yaw respectively
$\mathbf{I}_{n\times n}$	Identity matrix of size n
$\mathbf{0}_{m\times n}$	m-by-n matrix of zeros
$\mathbf{1}_{m\times n}$	m-by-n matrix of ones
M	Moment vector
F	Force vector
τ	Generalized vector consisting of force and torque parameters
H	Angular momentum

u	$u \in \mathbb{R}^{6\times 1}$ the input vector, $u = [\omega_1^2\ \omega_2^2\ \omega_3^2\ \omega_4^2\ \xi_1\ \xi_2]^T$
x	$x \in \mathbb{R}^{12\times 1}$ the state vector
A, B, C, D	State-space matrices of linear system
ζ	Generalized velocity vector
$\mathbf{M_h}$	System Inertia matrix
$\mathbf{C_h}(\zeta)$	The Coriolis-centripetal matrix
$\mathbf{G_h}$	The gravitational vector
$\bar{g}$	Gravitational acceleration
B_f	The control effectiveness matrix
P_{ca}	Control Allocation matrix
Q, W	Weighting matrices used in control allocation optimization problem
$G(s)$	Plant transfer function
$C(s)$	Controller transfer function
L	The open loop transfer function
T	The complementary sensitivity function
S	Sensivity transfer function

CHAPTER 1

INTRODUCTION

1.1 Motivation

Aerial robotics attract a fast-growing interest among academics and engineers due to their research challenges, commercial opportunities, and availability. Open-source hardware and software projects are revolutionizing Unmanned Aerial Vehicles (UAVs) technology, and advancements in avionics have significantly reduced the cost of aerial robotics. Beyond commercial uses such as agriculture, filmmaking, indoor or outdoor inspections, mapping, surveying, wireless coverage, delivery, and military, small robotic helicopters have found use even on planet Mars for 2021 missions of NASA [2].

Various types of UAV classifications can be found in the literature [3], focusing on different parameters such as size, shape, flight range, maximum take-off weight (MTOW), or mission. There exist two main categories of UAVs, fixed-wing and rotary-wing UAVs. Fixed-wing UAVs have the advantage of being able to fly at high speeds for longer periods of time, thus providing wider survey areas for each flight. On the other hand, rotary-wing UAVs (also called multicopters) have flight capabilities such as hovering, vertical take-off, and landing and agile maneuvering capability. There are also hybrid solutions that possess the strengths of both a rotary and fixed-wing aircraft on a single platform [4].

To improve the feasibility of commercial uses, there is a demand for reliable UAV platform solutions with improved flight time durability and increased payload capacity. The main challenges are to increase the available energy densities of power supplies and to increase the efficiency of converting this energy to the thrust of air

in a mechanically robust platform. Internal combustion engine based UAVs have longer endurance due to their higher energy densities. However, their design is more complex, requires frequent maintenance, and their thermal and acoustic signature is high compared to electric motors. A hybrid power architecture, by combining several power sources (battery, fuel cell, solar cells, and supercapacitor), is suggested to be the best option for providing endurance for a UAV in [5].

Multicopters have fixed blades with a pitch that is not possible to control as it does for a helicopter (through the swashplate). Instead, multicopters vary the speed of the rotors to achieve motion control. Varying-pitch propeller mechanism is a more efficient solution than changing the RPM of propellers. However, swashplate increases the mechanical complexity dramatically. The single main rotor with a vertical anti-torque tail rotor configuration has become the most common type of helicopter thanks to large diameter main propellers reducing disk load. Some engine power is allocated to counter the reaction torque of the main rotor though. Tandem rotor helicopters, however, use counter-rotating rotors (two sets), with each canceling out the other's torque. Therefore, all of the power from the engines can be used for lift, allowing even more efficiency. Coaxial helicopters with two stacked rotors suffer from the loss of efficiency due to the higher relative disk loading [6], it allows even more compact form though. The major disadvantage of both traditional single-rotor helicopters and tandem rotor helicopters for aerial robotics is that they require a mechanically complex swashplate mechanism with rotating joints, which decreases the reliability of aerial robotic platform.

The main motivation of this study is the research for an aircraft design that is efficient for the heavy lift in terms of power consumption, mechanically simple and robust enough to meet reliability requirements, and controllable enough to reject wind and other disturbances.

1.2 Proposed System and Methods

We attack the problem of efficiency and mechanical complexity by presenting a new UAV system design, HLAV (Heavy-lifting aerial vehicle), that will give robust re-

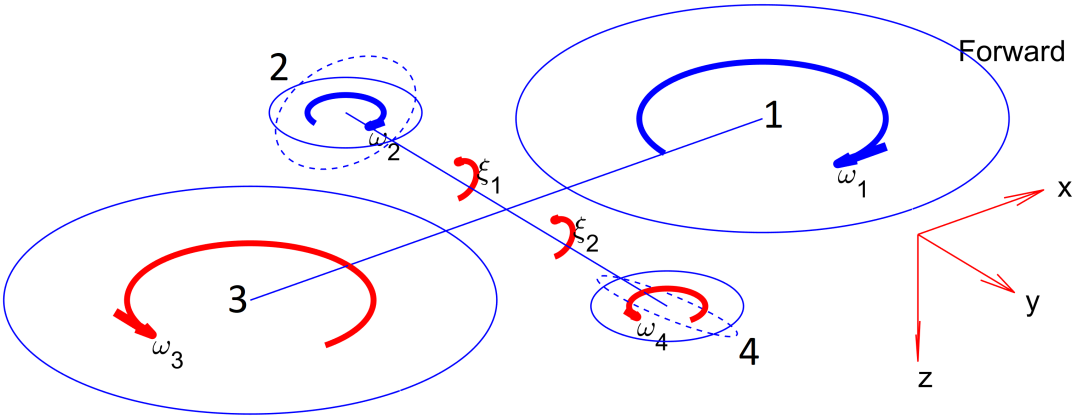

Figure 1.1: HLAV: Proposed configuration with "PPNN" propeller arrangement

sults in terms of flight time durability, payload capacity, and mechanical reliability. There will be no swashplates in the proposed design since our focus is to guarantee efficiency while reducing mechanical complexity. This system will carry the main payload with two large propellers (similar to a tandem rotor helicopter), but instead of stabilizing the attitude using complex swashplate mechanisms, we add two smaller rotors that can tilt [7]. Large propellers will be more efficient than smaller propellers thanks to their greater disk area. Therefore, the main lift will be provided by two large propellers. Proposed design is given in Fig. 1.1, explained in Fig. 1.2 and it is shown in flight test in Fig. 7.6. The proposed system given in Fig. 1.1 includes four propellers and two servo motors. Propellers 1 through 4 are positioned parallel to the xy-plane, at 0, 270, 180 and 90 degrees from the x-axis, respectively. The 1st and 2nd servo motors independently control the tilt angle of 2nd and 4th propellers in y-axis. The tilt angles are ξ_1 and ξ_2 radians respectively. The 1st and 2nd propellers rotate positively with respect to z axis at angular velocity ω_1 and ω_2 rad/s, and the 3rd and 4th propellers rotate negatively with respect to z axis at angular velocity ω_3 and ω_4 rad/s.

Conventional quadcopters have a "PNPN" (P: Clockwise, N: Counterclockwise) propeller arrangement (See Fig. 1.3a), that is, oppositely placed propellers rotate in the same direction. The system we propose has a "PPNN" propeller arrangement to compensate for the reaction torques of equally sized propeller pairs placed on opposite sides. However, the "PPNN" propeller arrangement loses controllability in hover state [8]. We provide the ability to tilt for small propellers with servo motors to en-

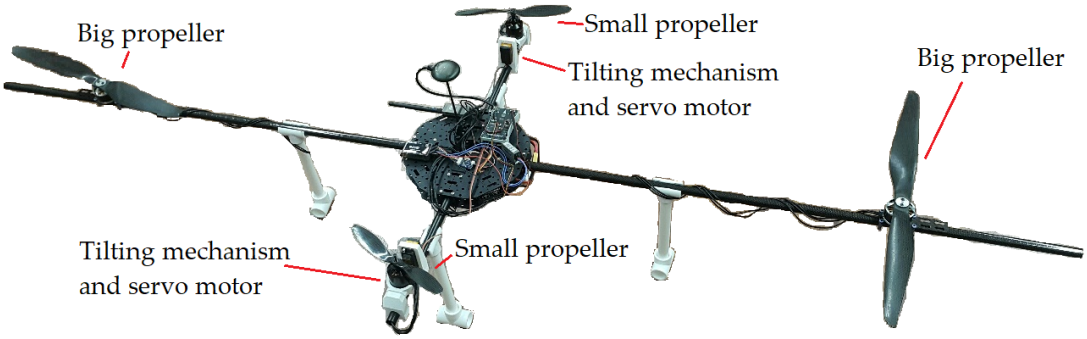

Figure 1.2: HLAV: Configuration overview

sure full state controllability (see Section 3.1).

Classical controllability analysis provides a binary output; either a system is controllable or it is uncontrollable, which is not practically useful alone. For example, the quadcopter with "PPNN" configuration given in Fig. 1.3b is not full state controllable, but if we extend one of the arms by ϵ meter (a very small amount), the system would be full state controllable in theory [9]. But in practice, we would require infinite bandwidth motors and no-delay sensors. Therefore, we need to rank the degree of controllability which is discussed in [10] in detail. In [11], a degree of controllability algorithm is proposed for multicopters. We inspect the controllability degree through control allocation analysis and inspect the attainable control set in hover (see Chapter 4).

Control allocation can be defined as distributing the redundant control effectors together to achieve the desired virtual control efforts. Control allocation has a matter of high importance, notably for control design of land, sea, or aerial vehicles [12–17], and their fault tolerance analysis [18]. Some control allocation methods are; direct allocation method, daisy chaining, pseudo-inverse [19]. When the control allocation problem is formulated as an optimization problem, references [17, 20–28] discuss various methods of solving it. Iterative numerical linear programming (LP) or quadratic programming (QP) algorithms are possible. Some popular methods are simplex, active-set, interior point, fixed-point. In this work, optimization-based control allocation algorithm based on quadratic programming is studied.

Precise positioning of servo motors that are used in tilt mechanism, is a crucial pa-

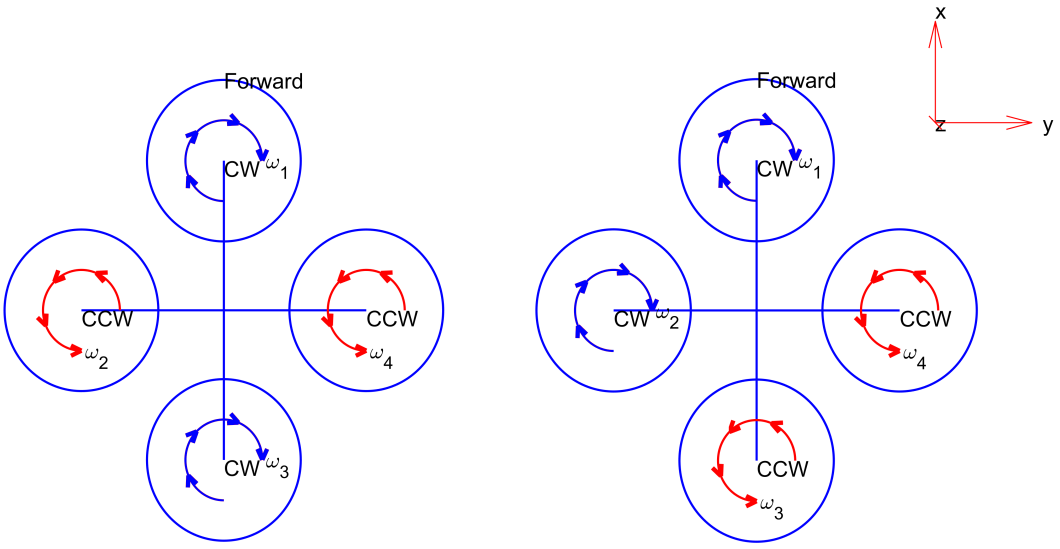

(a) "PNPN" configuration

(b) "PPNN" configuration

Figure 1.3: Configuration types

rameter for reducing vibrations in the HLAV and improve overall flight performance. Due to size and weight limitations, the motor is required to be small but torque density is desired to be high. In high torque and inexpensive PMSM and BLDC motors, cogging torque and friction are usually the main challenging disturbance sources. Cogging torque and friction can be identified using position sensors that already exist in the tilt mechanism, so the cost of the system is not increased. We attack this problem by developing feedforward algorithms and show that with cogging torque compensation alone, 30-65% of the positional error can be removed in a feedback control system.

1.3 Discussion: HLAV Efficiency Comparison Using Momentum Theory

Accurate estimation of power efficiency is by no means straightforward, as many parameters affect performance. However, the fundamental performance of the rotor can be predicted using the Rankine-Froude *momentum theory*, which gives a first-order prediction of thrust and power [6, pp. 59-81]. The rotor disk area is denoted by A, atmospheric density by ρ. The thrust required to hover is $T = mg$. The momentum

theory states that the power required to hover, P can be predicted using (1.1);

$$P = \frac{T^{3/2}}{\sqrt{2\rho A}} \tag{1.1}$$

Power loading, $PL = T/P$, can be considered as a rotor efficiency parameter that is desired to be high. Disk loading, $DL = T/A$ is the thrust force per unit area of the rotor disk. The Equation 1.2 is derived using Eq. 1.1 and the definitions of PL, DL. It is observed from (1.2) that a low disk loading is directly correlated with higher power loading, hence efficiency.

$$PL = \sqrt{\frac{2\rho}{DL}} \tag{1.2}$$

Therefore, it is often preferred to have larger propellers in terms of efficiency. In practice, hover efficiency will be less than the ideal value estimated by (1.2) since viscous losses and other non-ideal effects are neglected. However, according to many experimental tests, there exist a strong correlation between the theoretical predictions and measured values [1,6]. Therefore efficiency analysis using the momentum theory approach gives considerable confidence.

In order to be able to compare various aircraft with each other, it is required to set certain constraints. Otherwise, simply increasing the disk area of rotors will result in a more efficient system regardless of the aerial vehicle configuration. Therefore, comparison without a restriction is not feasible. The constraint we apply in this study is the vehicle width restriction, W. Vehicle width is a restrictive parameter particularly in congested environments such as in aircraft traffic, indoor applications, forests, corridors, and tunnels. Length is not a limiting parameter in these environments.

In the analysis, we use the convention that each rotor in a vehicle carries a weight proportional to its area, so that the disk loading will be the same for each rotor, simplifying calculations. For example, if the total weight of the vehicle is T, each rotor will produce thrust $T/4$ for a quadcopter, $T/2$ for a bi-copter, and so on. For the HLAV configuration, if the area of the big rotors is n times the area of the small rotors, then each big rotor will produce $nT/(2n + 2)$ of thrust, and the small rotors will generate $T/(2n + 2)$ of thrust. In Fig. 1.4, HLAV is compared for power consumption with other common multi-rotor configurations, using momentum theory, following the methodology presented in [1]. Comparison is made for the same

weight and width of various aircraft configurations. Parameters are normalized relative to single-rotor helicopter and sorted by efficiency parameter, PL.

Configuration	*Rotor radius*	*Total area*	PL	*Mechanical Complexity More "+" means better*
HLAV 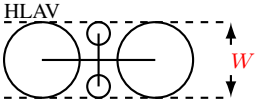	$r_s = 0.15W$ $r_b = 0.5W$	2.18	1.48	$+++$
Bi-copter 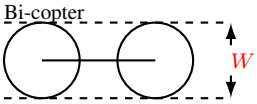	$r = 0.5W$	2	1.41	$+++$
Single-rotor helicopter 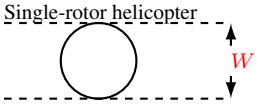	$r = 0.5W$	1	1	$+$
Quadcopter 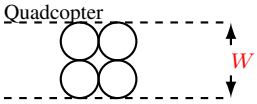	$r = 0.25W$	1	1	$+++$
Hexacopter 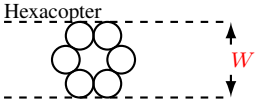	$r \approx 0.183W$	0.80	0.90	$++$
Tri-copter 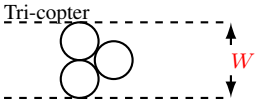	$r = 0.25W$	0.75	0.87	$+++$
Octocopter 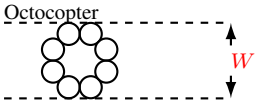	$r \approx 0.146W$	0.68	0.83	$++$

Figure 1.4: Comparison of hover efficiency (power loading) of the most common multi-copters and HLAV at the same weight using momentum theory under maximum width constraint, W. Parameters are normalized relative to single-rotor helicopter and sorted by efficiency. The methodology presented in [1] is followed.

According to the analysis presented in Fig. 1.4, HLAV appears to be the most efficient configuration under width constraints. For instance, HLAV can carry 48% more weight than a quadcopter for the same power, under certain constraints and assumptions. Quadcopter design requires some clearance between the rotors to avoid aerodynamic interference. If we take into account the required space between rotors in the analysis, the quadcopter's total disk area will be even smaller, leading to an even more inefficient configuration than HLAV. In terms of mechanical complexity, the single-rotor helicopter has the lowest mechanical structure reliability due to the swashplate mechanism with rotating joints. Hexacopter and octocopter can be con-

sidered mechanically less reliable than quadcopter, tri-copter, bi-copter, and HLAV due to their large number of rotors.

Bi-copter configuration seems to be the biggest competitor of HLAV according to the analysis in Fig. 1.4 in terms of power efficiency. Bi-copter configuration consists only of two rotors and two servo motors [1, 29]. Rotors are placed above the platform's center of mass to create a weight-based torque, which provides an inherently stable system [30]. Tandem rotors can be actuated by two servo motors (instead of a swash-plate mechanism), leading to an even more minimal design than HLAV. However, the bi-copter design also has some significant disadvantages compared to HLAV as follows;

- Bi-copter configuration roll controllability is dependent on the vertical distance between the center of mass of the body platform and the plane of the rotor's shaft. Due to structural limitations in bi-copter designs, this distance is usually small [29], resulting in a limited roll moment and reduced roll control authority.

- During the transient responses of the roll rotation of the bi-copter, an undesired thrust is projected onto the y-axis of the body frame. This is not the case for the HLAV system.

- The non-minimum phase dynamics in the roll axis poses control issues [31] for the bi-copter. Non-minimum phase dynamics stem from the servo motor reaction torque that is applied on the body. A similar problem is also present for HLAV since HLAV also possesses servo motors. But this is negligible for the HLAV as the servo motors are integrated into the small rotors, whereas bi-copter servo motors actuate the main rotors. For HLAV, the reaction torque coming from the servo motor tilt acceleration is negligible since the inertia is so small compared to the vehicle inertia I_{yy}.

- For the bi-copter design, the essential lifting force is applied through the tilt-mechanism. This extra intermediate mechanism causes the rigidity of the mechanical structure to decrease and may introduce vibration, resonance, and other structural problems in large dimensions. In the HLAV design, the main two large rotors that carry the main load are directly connected to the body.

In this way, HLAV provides a more rigid structure, enabling it to scale larger dimensions.

Multicopter is a general term for a family of unmanned aircraft, which include the numerous forms of bicopter, tricopter, quadcopter, hexacopter, octocopter, and various types of other VTOL (vertical take-off landing) aircraft that employ multiple rotors for lift and control. In literature, there exist detailed comparisons of candidate configurations, [8, 32]. In general, it can be predicted that the more rotor an UAV has, the better the flight characteristics and the more redundant it will be in case of rotor failure for safety. The downside, however, is a reduction in power efficiency and less flight time. In addition, costs increase significantly due to additional equipment and maintenance.

Tricopters are more common than the bicopters and have been studied a lot in the literature such as: [33–36]. The tricopter type UAV has the problem of yaw control caused by the reaction torque of an unpaired rotor. This is usually solved by adding a servo motor to one or more of the tails, which will improve the yaw movements significantly. Another design is called Coaxial Tri-Rotor UAV (Y6), which has two rotors placed on each rotor axis. Instead of using a servo motor to control the yaw axis, there are CW (clockwise) and CCW (counter clockwise) propellers on the same arm. This type of multicopter can be made as compact as a tricopter, and will have greater payload capacity. However, the Y6 configuration suffers from the loss of efficiency due to the coaxial rotor arrangement. According to [32], this Y6 configuration maximizes wind resistance property which is a very important feature for critical missions.

As can be seen from Fig. 1.4, HLAV has superior advantages in terms of power efficiency and mechanical reliability. As the HLAV prototype scales up to larger sizes, a more effective system for heavy lifting will emerge. However, larger sizes have a natural limit. In general, the larger the rotor size, the slower the rotor dynamic response and the lower the control agility. Fortunately, agility is not the HLAV's primary design goal, and the increased weight would help counter the wind disturbance. In very large rotors, blade flapping is another major issue, as it causes wear and tear on the rotor hub. Therefore, large rotors may require mechanical enhancements such

as flapping hinges to reduce the bending forces transferred to the platform body [8].

In Fig. 1.4, only commonly seen UAV configurations are outlined. In the literature, a wide variety of unconventional configurations of aircraft have also been proposed, such as the triangular quadrotor in [37], unmanned aerial robot (UAR) X5 in [38], and a novel compound hexacopter using propellers of different sizes for separate lift and attitude control in [39].

1.4 Contributions and Novelties

The preliminary version of this work and early ideas were presented at the international conferences; 6th International Conference on Control Engineering & Information Technology (CEIT-2018) [7], 12th Asian Control Conference (ASCC-2019) [40], and at several national conferences; Türkiye Robot Bilim Konferansı (TORK-2018), 9. Savunma Teknolojileri Kongresi (SAVTEK-2018), Otomatik Kontrol Türk Milli Komitesi Ulusal Toplantısı (TOK-2018).

This thesis fully develops our previously published work in several areas: first of all, we expand the discussion of the system, elaborate and improve the dynamic modeling of the system. The challenging part of this system is the optimal control allocation design specific to HLAV. In this study, we develop a control allocation strategy based on quadratic programming for HLAV and report the results. Finally, the proposed system is experimentally verified with a newly build prototype, and sufficient stability and trajectory tracking performance are achieved, proving the controllability concept with a demonstration.

Key contributions can be summarized as follows;

- Proposed HLAV configuration, a novel design. To the best of our knowledge, this system is unique.
- Derivation of nonlinear dynamic model and controllability analysis of the HLAV.
- A control allocation strategy based on quadratic programming for HLAV, and comparison with the pseudo-inverse method.

- A method development for cogging torque and friction identification and compensation for precise positioning of servo motors that can be used in tilt-rotors.

- Experimental flight tests and validation on the real prototype system, HLAV.

1.5 The Outline of the Thesis

Chapter 1 gives information about the motivation of a new aerial vehicle. The HLAV system is introduced and challenges behind this concept, such as controllability, control allocation, and tilt-rotor control are discussed. The efficiency of HLAV relative to various aircraft configurations under certain constraints is discussed using momentum theory. Contributions and novelties which resulted from this thesis are summarized.

Chapter 2 explains the mathematical model of the HLAV configuration. Kinematic and rigid body dynamic parts of the aerial vehicle are explained. The assumptions used in the modeling are given. 6-DOF rigid body dynamic equations are derived and the nonlinear model of the HLAV configuration is built by the Newton-Euler approach.

Chapter 3 includes the linear analysis and proposes a simplified control allocation method. The system is linearized around the equilibrium point and it is shown that controllability and observability matrices are full rank. The control effectiveness matrix for a reduced model is determined. The pseudo-inverse control allocation matrix which maps the torque and force parameters to motor parameters (propellers' speed and servo motor angles) is developed with some simplifications. Finally, the HLAV system is simulated with realistic parameters, and the degree of controllability and flight performance of the system under simple control allocation are verified. The pseudo-inverse control allocation method, discussed in this chapter, has some weaknesses and does not utilize the full available control set in the hover state which reduces the robustness of HLAV to large disturbances. It does not necessarily generate optimal performing input sets for effectors. It may also fail in maneuvering vehicle states and in other states different from the hovering state. The next chapter dives into this area and develops advanced control allocation algorithms.

Chapter 4 discusses improved control allocation strategies and shows how the control allocation strategy based on quadratic programming can be developed to utilize HLAV capacity in maximum performance with optimal power. This chapter starts with a description of control system architecture. It continues with the formulation of a general control allocation problem. Then, the optimization problem is reformulated according to the requirements and properties of HLAV. Algorithms to find the maximum attainable control set are given as pseudocode. It is shown that the control allocation strategy based on quadratic programming for HLAV utilizes the attainable control set better overall than the pseudo-inverse control allocation method. Implementation issues and practical considerations are discussed.

Chapter 5 consist of system identification and high-level controller design parts. Model parameters are estimated using closed-loop system identification tools. The system under study is open-loop unstable. Therefore, frequency response function (FRF) measurements should be realized under closed-loop operation. Closed-loop identification issues are overcome with the following strategies; the indirect approach and direct approach with subspace methods. High-level controllers are designed with the "manual loop shaping" method in cascaded control loop structure to satisfy robust performance and stability. Analysis results are presented.

Chapter 6 attacks the cogging torque and friction disturbance rejection problem for the low-level controllers of servo motors to be used in tilt-rotor mechanism. This chapter begins with a discussion and motivation followed by a brief literature review of developments. Precise positioning of servo motors that are used in tilt mechanism, is a crucial parameter for reducing vibrations in the HLAV and improve overall flight performance. Due to size and weight limitations, the motor is required to be small but torque density is desired to be high. In high torque and cheap PMSM and BLDC motors, cogging torque and friction are usually the main challenging disturbance sources. The chapter continues with an overview of the test and measurement setup. Cogging torque and friction can be identified using position sensors that already exist in the tilt mechanism, so the cost of the system is not increased. Current and speed controller designs are presented. The controller implementation issues are examined in an embedded world with their practical considerations. The results of the cogging torque identification and compensation are presented. The results of friction identification

and compensation are reported. This study shows that, by developing feedforward algorithms, with only cogging torque compensation, 30-65% of the tracking error can be removed in a feedback control system. The results presented in this chapter are published in our paper [40].

Chapter 7 starts with a brief description of the hardware and software of a newly built experimental test prototype. The experimental test results are presented and flight performance is analyzed, proving the HLAV concept by demonstration in the outdoor environment. The feasibility and performance of the system are verified.

Chapter 8 gives concluding remarks, summarizes this thesis, elaborates the importance of the work, and comments on the results. In addition, applications and extensions are suggested as a continuation of this work.

Appendix A presents the controllability analysis of the previous version of HLAV configuration. With the motivation explained in Section 1.1, the HLAV system is proposed to increase the flight time durability and payload capacity of existing solutions with a robust mechanics design. Before we arrived at the HLAV system, we studied several types of vehicle structures. For example, whether we need servo motors in the HLAV system has been decided as a result of the analysis made in this chapter. The main difference between the HLAV system and the system described here is that the system does not have servo motors, so we may assume ξ_1 and ξ_2 angles as 0 and fixed. We analyze the controllability using linear analysis and checking the controllability degree. It is found that indeed the PPNN configuration with no servo motor aerial vehicle is not controllable. This result revealed the necessity of using the tilt-rotor mechanism and led to the development of the HLAV system to its current state.

CHAPTER 2

DYNAMIC SYSTEM MODELING

This chapter explains the mathematical model of the HLAV configuration. Kinematic and rigid body dynamic parts of the aerial vehicle are explained. The assumptions used in the modeling are given. 6-DOF rigid body dynamic equations are derived and the nonlinear model of the HLAV configuration is built by the Newton-Euler approach.

2.1 Notation and Definitions

A general nomenclature followed in this dissertation is given in the list of abbreviations on page xxi and in the list of symbols on page xxiii to unambiguously identify quantities. The frame of reference in which the quantity is represented is indicated by the superscript. The second subscript denotes which coordinate frame moves relative to the coordinate frame given by the first subscript. We need to precisely define a set of Cartesian coordinate frames of reference. Each coordinate frame given in the list of symbols is an orthogonal, right-handed, co-ordinate frame or axis set [41]. The Earth frame rotates, relative to the inertial frame, at a rate ω_{ie}^{e}. The navigation frame rotates relative to the Earth-fixed frame, due to the translational velocity of the vehicle, at a rate ω_{en}^{n}. This is commonly referred to as the transport rate. In this study, we ignore the ω_{ie}^{e} and ω_{en}^{n}. Navigation reference frame and Earth frame is treated as an inertial frame, using the flat-Earth approximation.

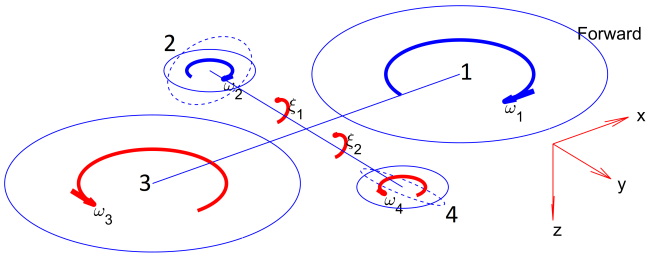

Figure 2.1: HLAV: Proposed configuration with "PPNN" propeller arrangement

2.2 Assumptions used in Modeling

The proposed system given in Fig. 2.1 includes four propellers and two servo motors. Propellers 1 through 4 are positioned parallel to the xy-plane, at 0, 270, 180 and 90 degrees from the x-axis, respectively. The 1st and 2nd servo motors independently control the tilt angle of 2nd and 4th propellers in y-axis. The tilt angles are ξ_1 and ξ_2 radians respectively. The 1st and 2nd propellers rotate positively with respect to z axis at angular velocity ω_1 and ω_2 rad/s, and the 3rd and 4th propellers rotate negatively with respect to z axis at angular velocity ω_3 and ω_4 rad/s.

During derivation of dynamic model, for simplification, some assumptions are useful [8, 34, 42–45];

- Rigid body assumption for modeling.
- The primary axes of the vehicle correspond to the principal axes of inertia. The mass is symmetrically distributed; i.e., products of inertia are considered negligible. Mass and the moments of inertia are constant.
- The thrust and reaction torque are proportional to the square of the angular velocity of the rotor.
- Tilting servo motor dynamics are independent of the rotational speed of the small rotors.
- The reaction torque coming from the servo motor tilt acceleration is not modeled since the inertia is small compared to the vehicle inertia I_{yy}. The reaction torque of the servo motor is treated as disturbance in the control system.

- We ignored known aerodynamic effects (blade flapping, airflow interference between each rotor, total thrust variation in translational flight) in modeling and treated them in the controller as input disturbance. In the hover state and in forward flight at small speeds with small pitch and roll angles, this assumption is found reasonable in the literature [45]. However, it is shown in [46] that for flights at fast speed, under aggressive and acrobatic maneuvers, ignoring aerodynamic effects prevents adequate control performance. However, it is shown in [46] that ignoring aerodynamic effects prevents high control performance from being achieved in high speed flights, under aggressive and acrobatic maneuvers. In [46], aerodynamics are modeled and they are compensated using feedback linearization controller techniques.

- The gyroscopic torques of the rotors are ignored in the model as they are mostly canceled out by counter-rotating big propellers and are negligible in magnitude for the small propellers. When the HLAV makes angular rotation in the inertial frame perpendicular to the rotor axis, the direction of angular momentum vectors of propeller changes resulting in creation of gyroscopic torque on the HLAV. No gyroscopic torque occurs when the vehicle rotation axis is aligned with the propeller rotation axis. For example, for big propellers which are fixed in the body frame, the rotation around the z_B axis (yaw) does not create gyroscopic torque, but the rotation around the x_B and y_B axes creates gyroscopic torque. Since small propellers can be tilted by ξ_i angle, they are treated after the transformation to the body frame. The gyroscopic (inertial) moment for big propellers ($i = 1, 3$) can be modeled as follows [45];

$$M^b_{i,G} = \vec{J}_{r,i} \left(\mathbf{\Omega}^b_{ib} \times \begin{bmatrix} 0 \\ 0 \\ 1 \end{bmatrix} \right) \omega_i \tag{2.1}$$

  The gyroscopic (inertial) moment for small propellers ($i = 2, 4$) can be modeled as follows;

$$M^b_{i,G} = \vec{J}_{r,i} \left(\mathbf{\Omega}^b_{ib} \times \begin{bmatrix} \boldsymbol{S}_{\xi_i} \\ 0 \\ \boldsymbol{C}_{\xi_i} \end{bmatrix} \right) \omega_i \tag{2.2}$$

Then the total gyroscopic torque acting on air-frame is as follows;

$$M_G^b = \sum_{i=1}^{4} M_{i,G}^b \tag{2.3}$$

where $\vec{J}_{r,i}$ is the gyroscopic inertia (rotating part of the rotor and propeller), i ($i = 1, 2, 3, 4$), $\mathbf{\Omega}_{ib}^b = [p, q, r]^T$, and ω_i is the angular rate of the rotor. If rotor rotates CW, ω_i is positive, otherwise it is negative.

- Ground effect significantly changes the aerial vehicle model at some low altitude region, so the model during normal flight differs from the model during takeoff and landing. In [47], mathematical model of ground effect is proposed as follows;

$$\frac{T}{T_\infty} = \frac{1}{1 - (R/4Z)^2} \tag{2.4}$$

Here R is the radius of the rotor, Z is the vertical distance from the ground, T is the thrust produced by the propeller in ground effect, and T_∞ is the thrust produced at the same power outside of ground effect. Note that for $Z/R = 2$ the predicted ratio between T and T_∞ is just 1.016. Therefore, this formula predicts that the ground effect is negligible when the rotor is more than one diameter off the ground. This gives us an idea of a reasonable hover test height.

2.3 6-DOF Rigid Body Dynamics

Under the assumptions presented in Section 2.2, rigid body dynamic model equations will be derived. For propellers from 1 to 4, thrust and reaction torque models in the body frame are given as follows;

$$f_1^b = \begin{bmatrix} 0 \\ 0 \\ -\mathrm{K}_{\mathrm{t_b}}\,\omega_1^2 \end{bmatrix} \qquad f_2^b = \begin{bmatrix} -\mathrm{K}_{\mathrm{t_s}}\,\omega_2^2\,\boldsymbol{S}_{\xi_1} \\ 0 \\ -\mathrm{K}_{\mathrm{t_s}}\,\omega_2^2\,\boldsymbol{C}_{\xi_1} \end{bmatrix} \tag{2.5}$$

$$f_3^b = \begin{bmatrix} 0 \\ 0 \\ -\mathrm{K}_{\mathrm{t_b}}\,\omega_3^2 \end{bmatrix} \qquad f_4^b = \begin{bmatrix} -\mathrm{K}_{\mathrm{t_s}}\,\omega_4^2\,\boldsymbol{S}_{\xi_2} \\ 0 \\ -\mathrm{K}_{\mathrm{t_s}}\,\omega_4^2\,\boldsymbol{C}_{\xi_2} \end{bmatrix} \tag{2.6}$$

$$M_1^b = \begin{bmatrix} 0 \\ \mathrm{K}_{\mathrm{t_b}}\,\mathrm{d_b}\,\omega_1^2 \\ -\mathrm{K}_{\mathrm{m_b}}\,\omega_1^2 \end{bmatrix} \qquad M_2^b = \begin{bmatrix} -\omega_2^2\,\left(\mathrm{K}_{\mathrm{m_s}}\,\boldsymbol{S}_{\xi_1} - \mathrm{K}_{\mathrm{t_s}}\,\mathrm{d_s}\,\boldsymbol{C}_{\xi_1}\right) \\ 0 \\ -\omega_2^2\,\left(\mathrm{K}_{\mathrm{m_s}}\,\boldsymbol{C}_{\xi_1} + \mathrm{K}_{\mathrm{t_s}}\,\mathrm{d_s}\,\boldsymbol{S}_{\xi_1}\right) \end{bmatrix} \tag{2.7}$$

$$M_3^b = \begin{bmatrix} 0 \\ -\mathrm{K}_{\mathrm{t_b}}\,\mathrm{d_b}\,\omega_3^2 \\ \mathrm{K}_{\mathrm{m_b}}\,\omega_3^2 \end{bmatrix} \qquad M_4^b = \begin{bmatrix} \omega_4^2\,\left(\mathrm{K}_{\mathrm{m_s}}\,\boldsymbol{S}_{\xi_2} - \mathrm{K}_{\mathrm{t_s}}\,\mathrm{d_s}\,\boldsymbol{C}_{\xi_2}\right) \\ 0 \\ \omega_4^2\,\left(\mathrm{K}_{\mathrm{m_s}}\,\boldsymbol{C}_{\xi_2} + \mathrm{K}_{\mathrm{t_s}}\,\mathrm{d_s}\,\boldsymbol{S}_{\xi_2}\right) \end{bmatrix} \tag{2.8}$$

Total thrust acting on the mass center on body coordinate system is given by;

$$\begin{aligned} F_{ext}^b &= \sum_{i=1}^{4} F_i^b \\ &= \begin{bmatrix} -\mathrm{K}_{\mathrm{t_s}}\,\left(\omega_2^2\,\boldsymbol{S}_{\xi_1} + \omega_4^2\,\boldsymbol{S}_{\xi_2}\right) \\ 0 \\ -\mathrm{K}_{\mathrm{t_b}}\,\omega_1^2 - \mathrm{K}_{\mathrm{t_b}}\,\omega_3^2 - \mathrm{K}_{\mathrm{t_s}}\,\omega_2^2\,\boldsymbol{C}_{\xi_1} - \mathrm{K}_{\mathrm{t_s}}\,\omega_4^2\,\boldsymbol{C}_{\xi_2} \end{bmatrix} \end{aligned} \tag{2.9}$$

Total torques acting on the mass center on body coordinate system is given by;

$$\begin{aligned} M_{ext}^b &= \sum_{i=1}^{4} M_i^b \\ &= \begin{bmatrix} \mathrm{K}_{\mathrm{m_s}}\,\omega_4^2\,\boldsymbol{S}_{\xi_2} - \mathrm{K}_{\mathrm{m_s}}\,\omega_2^2\,\boldsymbol{S}_{\xi_1} + \mathrm{K}_{\mathrm{t_s}}\,\mathrm{d_s}\,\omega_2^2\,\boldsymbol{C}_{\xi_1} - \mathrm{K}_{\mathrm{t_s}}\,\mathrm{d_s}\,\omega_4^2\,\boldsymbol{C}_{\xi_2} \\ \mathrm{K}_{\mathrm{t_b}}\,\mathrm{d_b}\,\left(\omega_1^2 - \omega_3^2\right) \\ \mathrm{K}_{\mathrm{m_b}}\,\omega_3^2 - \mathrm{K}_{\mathrm{m_b}}\,\omega_1^2 - \mathrm{K}_{\mathrm{m_s}}\,\omega_2^2\,\boldsymbol{C}_{\xi_1} + \mathrm{K}_{\mathrm{m_s}}\,\omega_4^2\,\boldsymbol{C}_{\xi_2} - \mathrm{K}_{\mathrm{t_s}}\,\mathrm{d_s}\,\omega_2^2\,\boldsymbol{S}_{\xi_1} + \mathrm{K}_{\mathrm{t_s}}\,\mathrm{d_s}\,\omega_4^2\,\boldsymbol{S}_{\xi_2} \end{bmatrix} \end{aligned} \tag{2.10}$$

Euler angles of ϕ, θ, ψ describe the roll, pitch and yaw angles from body to earth

coordinate system. Direction cosine matrix from body to earth is defined as;

$$\begin{aligned} C_b^e &= R_z(\psi)R_y(\theta)R_x(\phi) \\ &= \begin{bmatrix} \boldsymbol{C}_\psi \boldsymbol{C}_\theta & \boldsymbol{C}_\psi \boldsymbol{S}_\phi \boldsymbol{S}_\theta - \boldsymbol{C}_\phi \boldsymbol{S}_\psi & \boldsymbol{S}_\phi \boldsymbol{S}_\psi + \boldsymbol{C}_\phi \boldsymbol{C}_\psi \boldsymbol{S}_\theta \\ \boldsymbol{C}_\theta \boldsymbol{S}_\psi & \boldsymbol{C}_\phi \boldsymbol{C}_\psi + \boldsymbol{S}_\phi \boldsymbol{S}_\psi \boldsymbol{S}_\theta & \boldsymbol{C}_\phi \boldsymbol{S}_\psi \boldsymbol{S}_\theta - \boldsymbol{C}_\psi \boldsymbol{S}_\phi \\ -\boldsymbol{S}_\theta & \boldsymbol{C}_\theta \boldsymbol{S}_\phi & \boldsymbol{C}_\phi \boldsymbol{C}_\theta \end{bmatrix} \end{aligned} \tag{2.11}$$

We can transform the force vector to earth coordinate system as follows;

$$F_{ext}^e = C_b^e F_{ext}^b \tag{2.12}$$

$$= \begin{bmatrix} -\left(\boldsymbol{S}_\phi \boldsymbol{S}_\psi + \boldsymbol{C}_\phi \boldsymbol{C}_\psi \boldsymbol{S}_\theta\right)\left(\mathrm{K_{t_b}}\,\omega_1^2 + \mathrm{K_{t_b}}\,\omega_3^2 + \mathrm{K_{t_s}}\,\omega_2^2\,\boldsymbol{C}_{\xi_1} + \mathrm{K_{t_s}}\,\omega_4^2\,\boldsymbol{C}_{\xi_2}\right) - \mathrm{K_{t_s}}\,\boldsymbol{C}_\psi \boldsymbol{C}_\theta\,\left(\omega_2^2\,\boldsymbol{S}_{\xi_1} + \omega_4^2\,\boldsymbol{S}_{\xi_2}\right) \\ \left(\boldsymbol{C}_\psi \boldsymbol{S}_\phi - \boldsymbol{C}_\phi \boldsymbol{S}_\psi \boldsymbol{S}_\theta\right)\left(\mathrm{K_{t_b}}\,\omega_1^2 + \mathrm{K_{t_b}}\,\omega_3^2 + \mathrm{K_{t_s}}\,\omega_2^2\,\boldsymbol{C}_{\xi_1} + \mathrm{K_{t_s}}\,\omega_4^2\,\boldsymbol{C}_{\xi_2}\right) - \mathrm{K_{t_s}}\,\boldsymbol{C}_\theta \boldsymbol{S}_\psi\,\left(\omega_2^2\,\boldsymbol{S}_{\xi_1} + \omega_4^2\,\boldsymbol{S}_{\xi_2}\right) \\ \mathrm{K_{t_s}}\,\boldsymbol{S}_\theta\,\left(\omega_2^2\,\boldsymbol{S}_{\xi_1} + \omega_4^2\,\boldsymbol{S}_{\xi_2}\right) - \boldsymbol{C}_\phi \boldsymbol{C}_\theta\,\left(\mathrm{K_{t_b}}\,\omega_1^2 + \mathrm{K_{t_b}}\,\omega_3^2 + \mathrm{K_{t_s}}\,\omega_2^2\,\boldsymbol{C}_{\xi_1} + \mathrm{K_{t_s}}\,\omega_4^2\,\boldsymbol{C}_{\xi_2}\right) \end{bmatrix} \tag{2.13}$$

Now, we define an unified vector, $\tau_{ext} \in \mathbb{R}^{6\times 1}$, which consists of external forces in e-frame and moments in b-frame, produced jointly by the effectors.

$$\tau_{ext} = \begin{bmatrix} F_{ext}^e \\ M_{ext}^b \end{bmatrix} \tag{2.14}$$

Transformation matrix between angular body rates and Euler-rates can be derived as follows;

$$\begin{aligned} \begin{bmatrix} p \\ q \\ r \end{bmatrix} &= \begin{bmatrix} \dot{\phi} \\ 0 \\ 0 \end{bmatrix} + R_x(-\phi) \begin{bmatrix} 0 \\ \dot{\theta} \\ 0 \end{bmatrix} + R_x(-\phi)R_y(-\theta) \begin{bmatrix} 0 \\ 0 \\ \dot{\psi} \end{bmatrix} \\ &= \begin{bmatrix} \dot{\phi} \\ 0 \\ 0 \end{bmatrix} + \begin{bmatrix} 1 & 0 & 0 \\ 0 & \cos(\phi) & \sin(\phi) \\ 0 & -\sin(\phi) & \cos(\phi) \end{bmatrix} \begin{bmatrix} 0 \\ \dot{\theta} \\ 0 \end{bmatrix} + \\ &\begin{bmatrix} 1 & 0 & 0 \\ 0 & \cos(\phi) & \sin(\phi) \\ 0 & -\sin(\phi) & \cos(\phi) \end{bmatrix} \begin{bmatrix} \cos(\theta) & 0 & -\sin(\theta) \\ 0 & 1 & 0 \\ \sin(\theta) & 0 & \cos(\theta) \end{bmatrix} \begin{bmatrix} 0 \\ 0 \\ \dot{\psi} \end{bmatrix} \\ &= \underbrace{\begin{bmatrix} 1 & 0 & -\sin(\theta) \\ 0 & \cos(\phi) & \cos(\theta)\,\sin(\phi) \\ 0 & -\sin(\phi) & \cos(\phi)\,\cos(\theta) \end{bmatrix}}_{R_r} \begin{bmatrix} \dot{\phi} \\ \dot{\theta} \\ \dot{\psi} \end{bmatrix} \end{aligned} \tag{2.15}$$

We have obtained transformation matrix, R_r. Now we take the inverse of R_r to obtain euler-rates from body angular rates. Note that $R_r^{-1} \neq R_r^T$.

$$\begin{bmatrix} \dot{\phi} \\ \dot{\theta} \\ \dot{\psi} \end{bmatrix} = R_r^{-1} \begin{bmatrix} p \\ q \\ r \end{bmatrix} \tag{2.16}$$

$$= \begin{bmatrix} 1 & \boldsymbol{S}_\phi \boldsymbol{T}_\theta & \boldsymbol{C}_\phi \boldsymbol{T}_\theta \\ 0 & \boldsymbol{C}_\phi & -\boldsymbol{S}_\phi \\ 0 & \frac{\boldsymbol{S}_\phi}{\boldsymbol{C}_\theta} & \frac{\boldsymbol{C}_\phi}{\boldsymbol{C}_\theta} \end{bmatrix} \begin{bmatrix} p \\ q \\ r \end{bmatrix} \tag{2.17}$$

$$= \begin{bmatrix} p + \frac{\boldsymbol{S}_\theta \left(r \boldsymbol{C}_\phi + q \boldsymbol{S}_\phi \right)}{\boldsymbol{C}_\theta} \\ q \boldsymbol{C}_\phi - r \boldsymbol{S}_\phi \\ \frac{r \boldsymbol{C}_\phi + q \boldsymbol{S}_\phi}{\boldsymbol{C}_\theta} \end{bmatrix} \tag{2.18}$$

Translation equations of motion in earth frame is as follows;

$$\ddot{\mathbf{P}}_{eb}^e = \begin{bmatrix} \ddot{x} \\ \ddot{y} \\ \ddot{z} \end{bmatrix} = \begin{bmatrix} \dot{V}_x \\ \dot{V}_y \\ \dot{V}_z \end{bmatrix} = \frac{1}{m} F_{ext}^e + \begin{bmatrix} 0 \\ 0 \\ \bar{g} \end{bmatrix} \tag{2.19}$$

Moment equations of motion in the inertial frame is as follows;

$$M_{ext}^e = \frac{\mathrm{d}H^e}{\mathrm{d}t} \tag{2.20}$$

where H^e is the angular momentum about the system's mass center in e-frame. The equation (2.20) implies that the sum of the moments of all the external forces acting on a rigid body around a fixed point is equal to the time derivative of the total angular momentum of the body around that point. Coriolis theorem (also known as transport theorem) relates the derivative of a vector seen by an observer in a rotating coordinate system to that seen in inertial space. In order to derive M_{ext}^b, we apply Coriolis theorem to the (2.20) and obtain the following expression;

$$\begin{aligned} M_{ext}^b &= \frac{\mathrm{d}H^b}{\mathrm{d}t} + \boldsymbol{\Omega}_{ib}^b \times H^b \\ &= \mathbf{J}\dot{\boldsymbol{\Omega}}_{ib}^b + \boldsymbol{\Omega}_{ib}^b \times (\mathbf{J}\boldsymbol{\Omega}_{ib}^b) \end{aligned} \tag{2.21}$$

where M^b_{ext} is the applied torques, $\mathbf{J}$ is the inertia matrix, and $\mathbf{\Omega}^b_{ib}$ is the angular velocity about the principal axes. If we expand, the following equation is obtained [48];

$$\begin{aligned}
\sum M^b_{ext_1} =& I_{xx}\dot{p} - (I_{yy} - I_{zz})\, qr - I_{xy}\,(\dot{q} - rp) \\
&- I_{yz}\left(q^2 - r^2\right) - I_{zx}\,(\dot{r} + pq) \\
\sum M^b_{ext_2} =& I_{yy}\dot{q} - (I_{zz} - I_{xx})\, rp - I_{yz}\,(\dot{r} - pq) \\
&- I_{zx}\left(r^2 - p^2\right) - I_{xy}\,(\dot{p} + qr) \\
\sum M^b_{ext_3} =& I_{zz}\dot{r} - (I_{xx} - I_{yy})\, pq - I_{zx}\,(\dot{p} - qr) \\
&- I_{xy}\left(p^2 - q^2\right) - I_{yz}\,(\dot{q} + rp)
\end{aligned} \tag{2.22}$$

If the products of inertia are assumed zero, (2.22) becomes;

$$\begin{aligned}
\sum M^b_{ext_1} &= I_{xx}\dot{p} - (I_{yy} - I_{zz})\, qr \\
\sum M^b_{ext_2} &= I_{yy}\dot{q} - (I_{zz} - I_{xx})\, rp \\
\sum M^b_{ext_3} &= I_{zz}\dot{r} - (I_{xx} - I_{yy})\, pq
\end{aligned} \tag{2.23}$$

We derive dynamics using a hybrid frame of reference, h-frame, consisting of translational velocity in e-frame, and angular rate in b-frame. We define generalized velocity vector as follows;

$$\zeta = \begin{bmatrix} V_x \\ V_y \\ V_z \\ p \\ q \\ r \end{bmatrix} \tag{2.24}$$

Using the results of (2.14), (2.19), and (2.23), we define the dynamics of system in (2.25) in a generalized form;

$$\mathbf{M_h}\dot{\zeta} + \mathbf{C_h}(\zeta)\zeta = \tau_{ext} + \mathbf{G_h} \tag{2.25}$$

Hereafter, the definitions of all the quantities used in (2.25) are explained. System

Inertia matrix, $\mathbf{M_h}$ is as follows;

$$\begin{aligned}\mathbf{M_h} &= \begin{bmatrix} m\mathbf{I}_{3\times3} & \mathbf{0}_{3\times3} \\ \mathbf{0}_{3\times3} & \mathbf{J} \end{bmatrix} \\ &= \begin{bmatrix} m & 0 & 0 & 0 & 0 & 0 \\ 0 & m & 0 & 0 & 0 & 0 \\ 0 & 0 & m & 0 & 0 & 0 \\ 0 & 0 & 0 & I_{xx} & 0 & 0 \\ 0 & 0 & 0 & 0 & I_{yy} & 0 \\ 0 & 0 & 0 & 0 & 0 & I_{zz} \end{bmatrix}\end{aligned} \tag{2.26}$$

The Coriolis-centripetal matrix, $\mathbf{C_h}(\zeta)$, is defined as;

$$\begin{aligned}\mathbf{C_h}(\zeta) &= \begin{bmatrix} \mathbf{0}_{3\times3} & \mathbf{0}_{3\times3} \\ \mathbf{0}_{3\times3} & -\mathbf{S}\left(\mathbf{J}\boldsymbol{\Omega}_{ib}^{b}\right) \end{bmatrix} \\ &= \begin{bmatrix} 0 & 0 & 0 & 0 & 0 & 0 \\ 0 & 0 & 0 & 0 & 0 & 0 \\ 0 & 0 & 0 & 0 & 0 & 0 \\ 0 & 0 & 0 & 0 & I_{zz}r & -I_{yy}q \\ 0 & 0 & 0 & -I_{zz}r & 0 & I_{xx}p \\ 0 & 0 & 0 & I_{yy}q & -I_{xx}p & 0 \end{bmatrix}\end{aligned} \tag{2.27}$$

The gravitational vector, $\mathbf{G_h}$, is defined as;

$$\mathbf{G_h} = \begin{bmatrix} 0 \\ 0 \\ m\bar{g} \\ 0 \\ 0 \\ 0 \end{bmatrix} \tag{2.28}$$

By rearranging (2.25), the accelerations vector can be isolated;

$$\dot{\zeta} = \mathbf{M_h^{-1}}\left(-\mathbf{C_h}(\zeta)\zeta + \tau_{ext} + \mathbf{G_h}\right) \tag{2.29}$$

2.4 Nonlinear Model

We would like to derive the nonlinear function $\dot{x} = f(x, u)$ where the input vector is $u \in \mathbb{R}^{6\times1}$, and the state vector $x \in \mathbb{R}^{12\times1}$. We derive dynamics in a hybrid frame of reference, consisting of position and translational velocity quantities in e-frame, attitude in Euler angles, and angular rate quantities in b-frame as follows;

$$u = [\omega_1^2\ \omega_2^2\ \omega_3^2\ \omega_4^2\ \xi_1\ \xi_2]^T \tag{2.30}$$

$$x = [\underbrace{x\,y\,z}_{\text{pos}}\ \underbrace{\phi\,\theta\,\psi}_{\text{angle}}\ \underbrace{V_x\,V_y\,V_z}_{\text{vel.}}\ \underbrace{p\,q\,r}_{\text{angular vel.}}\ ]^T \tag{2.31}$$

$$= [\mathbf{P}^e\ \mathbf{\Theta}\ \mathbf{V}^e\ \mathbf{\Omega}_{ib}^b]^T \tag{2.32}$$

The output vector comprises variables of particular interest that can be physically measured or are required to behave in a specific manner. In our system, we will be able to measure angular rates (p, q, r) using gyroscope, yaw orientation (ψ^e) using magnetometer and earth position (x, y, z) using GPS. Then our measurement function can be defined as a 7×1 vector;

$$y = h(x) = [x\,y\,z\,\psi\,p\,q\,r]^T \tag{2.33}$$

In (2.29), we have already derived differential translational and rotational equations. Combining (2.14), (2.18), (2.29), and all the equations above, the nonlinear model can be explicitly derived in (2.34);

$$f(x,u) =$$

$$\begin{bmatrix} \dot{x} \\ \dot{y} \\ \dot{z} \\ \dot{\phi} \\ \dot{\theta} \\ \dot{\psi} \\ \dot{V}_x \\ \dot{V}_y \\ \dot{V}_z \\ \dot{p} \\ \dot{q} \\ \dot{r} \end{bmatrix} = \begin{bmatrix} V_x \\ V_y \\ V_z \\ p + \frac{\boldsymbol{S}_\theta \left(r\, \boldsymbol{C}_\phi + q\, \boldsymbol{S}_\phi \right)}{\boldsymbol{C}_\theta} \\ q\, \boldsymbol{C}_\phi - r\, \boldsymbol{S}_\phi \\ \frac{r\, \boldsymbol{C}_\phi + q\, \boldsymbol{S}_\phi}{\boldsymbol{C}_\theta} \\ -\frac{\left(\boldsymbol{S}_\phi\, \boldsymbol{S}_\psi + \boldsymbol{C}_\phi\, \boldsymbol{C}_\psi\, \boldsymbol{S}_\theta \right) \Delta_1 + \mathrm{K_{t_s}}\, \boldsymbol{C}_\psi\, \boldsymbol{C}_\theta \left(\omega_2^2\, \boldsymbol{S}_{\xi_1} + \omega_4^2\, \boldsymbol{S}_{\xi_2} \right)}{m} \\ \frac{\left(\boldsymbol{C}_\psi\, \boldsymbol{S}_\phi - \boldsymbol{C}_\phi\, \boldsymbol{S}_\psi\, \boldsymbol{S}_\theta \right) \Delta_1 - \mathrm{K_{t_s}}\, \boldsymbol{C}_\theta\, \boldsymbol{S}_\psi \left(\omega_2^2\, \boldsymbol{S}_{\xi_1} + \omega_4^2\, \boldsymbol{S}_{\xi_2} \right)}{m} \\ g + \frac{\mathrm{K_{t_s}}\, \boldsymbol{S}_\theta \left(\omega_2^2\, \boldsymbol{S}_{\xi_1} + \omega_4^2\, \boldsymbol{S}_{\xi_2} \right) - \boldsymbol{C}_\phi\, \boldsymbol{C}_\theta\, \Delta_1}{m} \\ -\frac{T_2\, \boldsymbol{S}_{\xi_1} - T_4\, \boldsymbol{S}_{\xi_2} - \mathrm{I_{yy}}\, q\, r + \mathrm{I_{zz}}\, q\, r - \mathrm{K_{t_s}}\, \mathrm{d_s}\, \omega_2^2\, \boldsymbol{C}_{\xi_1} + \mathrm{K_{t_s}}\, \mathrm{d_s}\, \omega_4^2\, \boldsymbol{C}_{\xi_2}}{\mathrm{I_{xx}}} \\ \frac{\mathrm{K_{t_b}}\, \mathrm{d_b}\, \omega_1^2 - \mathrm{K_{t_b}}\, \mathrm{d_b}\, \omega_3^2 - \mathrm{I_{xx}}\, p\, r + \mathrm{I_{zz}}\, p\, r}{\mathrm{I_{yy}}} \\ -\frac{T_1 - T_3 - \mathrm{I_{xx}}\, p\, q + \mathrm{I_{yy}}\, p\, q + T_2\, \boldsymbol{C}_{\xi_1} - T_4\, \boldsymbol{C}_{\xi_2} + \mathrm{K_{t_s}}\, \mathrm{d_s}\, \omega_2^2\, \boldsymbol{S}_{\xi_1} - \mathrm{K_{t_s}}\, \mathrm{d_s}\, \omega_4^2\, \boldsymbol{S}_{\xi_2}}{\mathrm{I_{zz}}} \end{bmatrix} \tag{2.34}$$

where;

$$\Delta_1 = \mathrm{K_{t_b}}\, \omega_1^2 + \mathrm{K_{t_b}}\, \omega_3^2 + \mathrm{K_{t_s}}\, \omega_2^2\, \boldsymbol{C}_{\xi_1} + \mathrm{K_{t_s}}\, \omega_4^2\, \boldsymbol{C}_{\xi_2}$$

$$T_1 = \mathrm{K_{m_b}}\, \omega_1^2,\ T_2 = \mathrm{K_{m_s}}\, \omega_2^2,\ T_3 = \mathrm{K_{m_b}}\, \omega_3^2,\ T_4 = \mathrm{K_{m_s}}\, \omega_4^2$$

CHAPTER 3

LINEAR ANALYSIS AND SIMPLE CONTROL ALLOCATION DESIGN

This chapter includes the linear analysis and proposes a simplified control allocation method. In Section 3.1, the system is linearized around the equilibrium point and it is shown that controllability and observability matrices are full rank. In Section 3.2, the control effectiveness matrix for a reduced model is determined. In Section 3.3, the pseudo-inverse control allocation matrix which maps the torque and force parameters to motor parameters (propellers' speed and servo motor angles) is developed with some simplifications. Finally, the HLAV system is simulated with realistic parameters, and the degree of controllability and flight performance of the system under simple control allocation are verified in Section 3.4.

3.1 Linearization

Inverse kinematics allow designing a control law that keeps the aerial vehicle in a certain attitude and position. Finding inverse function is not straightforward, and usually not possible in nonlinear systems. It is observed from Eq. 2.34 in Chapter 2 that, the nonlinear model is highly complicated. Nonlinear search is not feasible, therefore, vehicle dynamics need to be linearized.

The reference [49] performed linearization at four different equilibrium points and derived four different transfer-matrices, unlike linearization only in the hover state. The four different equilibrium points represent the different operating states commonly performed in typical flight missions. These states are;

1. Hover;

2. Constant velocity vertical motion;

3. Constant pitch angle, horizontal translation;

4. Constant roll angle, horizontal translation;

There are issues of controller switch between two linear systems. Therefore, [49] designs a one common linear time-invariant controller to stabilize all four systems. The concept of stabilizing different systems with one common controller is called the "simultaneous stabilization problem".

In this section, we present the linearization analysis in the equilibrium point of hovering flight, with the following states and inputs;

$$\begin{aligned} x_0 &= [x_0\ y_0\ z_0\ 0\ 0\ \psi_0\ 0\ 0\ 0\ 0\ 0\ 0]^T \\ u_0 &= \left[\omega_{1,0}^2\ \omega_{2,0}^2\ \omega_{3,0}^2\ \omega_{4,0}^2\ 0\ 0\right]^T \end{aligned} \tag{3.1}$$

Here, $\omega_{1,0} = \omega_{3,0}$ and $\omega_{2,0} = \omega_{4,0}$. In equilibrium point, first derivatives of the states are equal to zero;

$$f(x_0, u_0) \equiv 0 \tag{3.2}$$

Then the nonlinear model given in (2.33) and (2.34) can be linearized around the equilibrium point as follows;

$$A = \frac{\partial f(x_0, u_0)}{\partial x} \quad B = \frac{\partial f(x_0, u_0)}{\partial u} \quad C = \frac{\partial h(x_0)}{\partial x} \tag{3.3}$$

with the following dynamics;

$$\dot{z} = Az + Bv \tag{3.4}$$

$$z = x - x_0 \tag{3.5}$$

$$v = u - u_0 \tag{3.6}$$

Then, A, B, and C matrices are obtained as follows;

$$A = \begin{bmatrix} 0 & 0 & 0 & 0 & 0 & 0 & 1 & 0 & 0 & 0 & 0 & 0 \\ 0 & 0 & 0 & 0 & 0 & 0 & 0 & 1 & 0 & 0 & 0 & 0 \\ 0 & 0 & 0 & 0 & 0 & 0 & 0 & 0 & 1 & 0 & 0 & 0 \\ 0 & 0 & 0 & 0 & 0 & 0 & 0 & 0 & 0 & 1 & 0 & 0 \\ 0 & 0 & 0 & 0 & 0 & 0 & 0 & 0 & 0 & 0 & 1 & 0 \\ 0 & 0 & 0 & 0 & 0 & 0 & 0 & 0 & 0 & 0 & 0 & 1 \\ 0 & 0 & 0 & -\frac{\boldsymbol{S}_{\psi_0}\,\Delta_3}{m} & -\frac{\boldsymbol{C}_{\psi_0}\,\Delta_3}{m} & 0 & 0 & 0 & 0 & 0 & 0 & 0 \\ 0 & 0 & 0 & \frac{\boldsymbol{C}_{\psi_0}\,\Delta_3}{m} & -\frac{\boldsymbol{S}_{\psi_0}\,\Delta_3}{m} & 0 & 0 & 0 & 0 & 0 & 0 & 0 \\ 0 & 0 & 0 & 0 & 0 & 0 & 0 & 0 & 0 & 0 & 0 & 0 \\ 0 & 0 & 0 & 0 & 0 & 0 & 0 & 0 & 0 & 0 & 0 & 0 \\ 0 & 0 & 0 & 0 & 0 & 0 & 0 & 0 & 0 & 0 & 0 & 0 \\ 0 & 0 & 0 & 0 & 0 & 0 & 0 & 0 & 0 & 0 & 0 & 0 \end{bmatrix} \tag{3.7}$$

where;

$$\Delta_3 = \left(\mathrm{K_{t_b}}\,\omega_{1,0}^2 + \mathrm{K_{t_b}}\,\omega_{3,0}^2 + \mathrm{K_{t_s}}\,\omega_{2,0}^2 + \mathrm{K_{t_s}}\,\omega_{4,0}^2\right)$$

$$B = \begin{bmatrix} 0 & 0 & 0 & 0 & 0 & 0 \\ 0 & 0 & 0 & 0 & 0 & 0 \\ 0 & 0 & 0 & 0 & 0 & 0 \\ 0 & 0 & 0 & 0 & 0 & 0 \\ 0 & 0 & 0 & 0 & 0 & 0 \\ 0 & 0 & 0 & 0 & 0 & 0 \\ 0 & 0 & 0 & 0 & -\frac{\mathrm{K_{t_s}}\,\omega_{2,0}^2\,\boldsymbol{C}_{\psi_0}}{m} & -\frac{\mathrm{K_{t_s}}\,\omega_{4,0}^2\,\boldsymbol{C}_{\psi_0}}{m} \\ 0 & 0 & 0 & 0 & -\frac{\mathrm{K_{t_s}}\,\omega_{2,0}^2\,\boldsymbol{S}_{\psi_0}}{m} & -\frac{\mathrm{K_{t_s}}\,\omega_{4,0}^2\,\boldsymbol{S}_{\psi_0}}{m} \\ -\frac{\mathrm{K_{t_b}}}{m} & -\frac{\mathrm{K_{t_s}}}{m} & -\frac{\mathrm{K_{t_b}}}{m} & -\frac{\mathrm{K_{t_s}}}{m} & 0 & 0 \\ 0 & \frac{\mathrm{K_{t_s}\,d_s}}{\mathrm{I_{xx}}} & 0 & -\frac{\mathrm{K_{t_s}\,d_s}}{\mathrm{I_{xx}}} & -\frac{\mathrm{K_{m_s}}\,\omega_{2,0}^2}{\mathrm{I_{xx}}} & \frac{\mathrm{K_{m_s}}\,\omega_{4,0}^2}{\mathrm{I_{xx}}} \\ \frac{\mathrm{K_{t_b}\,d_b}}{\mathrm{I_{yy}}} & 0 & -\frac{\mathrm{K_{t_b}\,d_b}}{\mathrm{I_{yy}}} & 0 & 0 & 0 \\ -\frac{\mathrm{K_{m_b}}}{\mathrm{I_{zz}}} & -\frac{\mathrm{K_{m_s}}}{\mathrm{I_{zz}}} & \frac{\mathrm{K_{m_b}}}{\mathrm{I_{zz}}} & \frac{\mathrm{K_{m_s}}}{\mathrm{I_{zz}}} & -\frac{\mathrm{K_{t_s}\,d_s}\,\omega_{2,0}^2}{\mathrm{I_{zz}}} & \frac{\mathrm{K_{t_s}\,d_s}\,\omega_{4,0}^2}{\mathrm{I_{zz}}} \end{bmatrix} \tag{3.8}$$

$$C = \begin{bmatrix} 1 & 0 & 0 & 0 & 0 & 0 & 0 & 0 & 0 & 0 & 0 & 0 \\ 0 & 1 & 0 & 0 & 0 & 0 & 0 & 0 & 0 & 0 & 0 & 0 \\ 0 & 0 & 1 & 0 & 0 & 0 & 0 & 0 & 0 & 0 & 0 & 0 \\ 0 & 0 & 0 & 0 & 0 & 1 & 0 & 0 & 0 & 0 & 0 & 0 \\ 0 & 0 & 0 & 0 & 0 & 0 & 0 & 0 & 0 & 1 & 0 & 0 \\ 0 & 0 & 0 & 0 & 0 & 0 & 0 & 0 & 0 & 0 & 1 & 0 \\ 0 & 0 & 0 & 0 & 0 & 0 & 0 & 0 & 0 & 0 & 0 & 1 \end{bmatrix} \tag{3.9}$$

The origin of the input signal of the linear system ($v = \mathbf{0}_{6x1}$, (3.6)) is an interior point of the control constraint set. Therefore, we can apply the classical controllability techniques to the system. When we analyze the controllability and observability matrices using the "MATLAB symbolic toolbox", they result in full rank (See (3.10)). Therefore, the system is both controllable and observable.

$$\begin{aligned} &\text{Rank} \begin{bmatrix} B & AB & A^2B & \dots & A^{11}B \end{bmatrix} = 12 \\ &\text{Rank} \begin{bmatrix} C \\ CA \\ CA^2 \\ \vdots \\ CA^{11} \end{bmatrix} = 12 \end{aligned} \tag{3.10}$$

3.2 The Control Effectiveness Matrix

For the autopilot, we ignore the lateral and longitudinal translation states (x, y) and their derivatives (V_x, V_y). We define a new, reduced order, linear dynamic model of the aerial vehicle. We edit (3.4) such that input vector motor parameters, $v_{6\times1}$, are

converted into force and torque parameters, $u_{4\times1}$.

$$\dot{z} = Az + \underbrace{B}_{=GB_f} v \tag{3.11}$$

$$= Az + G\underbrace{B_f v}_{=\tau} \tag{3.12}$$

$$= Az + G\tau \tag{3.13}$$

Here;

$$z = [z\ \phi\ \theta\ \psi\ V_z\ p\ q\ r]^T \in \mathbb{R}^8 \tag{3.14}$$

$$\tau = [F^e_{des_3}\ M^b_{des_1}\ M^b_{des_2}\ M^b_{des_3}]^T \in \mathbb{R}^4 \tag{3.15}$$

$$A = \begin{bmatrix} \mathbf{0}_{4\times4} & \mathbf{I}_{4\times4} \\ \mathbf{0}_{4\times4} & \mathbf{0}_{4\times4} \end{bmatrix} \in \mathbb{R}^{8\times8} \tag{3.16}$$

$$G = \begin{bmatrix} \mathbf{0}_{4\times4} \\ J_f^{-1} \end{bmatrix} \in \mathbb{R}^{8\times4} \tag{3.17}$$

$$J_f = diag(m, I_{xx}, I_{yy}, I_{zz}) \in \mathbb{R}^{4\times4} \tag{3.18}$$

For the input vector, τ consist of desired force input in e-frame and desired torque inputs in b-frame. The control effectiveness matrix, B_f maps the rotor and servo control parameters to the system total thrust/moment;

$$\tau = B_f\, v \tag{3.19}$$

where, τ is given in (3.15), and v is given in (3.6).

We first take the last 4 row of B matrix in (3.3) and obtain $\bar{B}$. We can derive control effectiveness matrix, $B_{f_{4\times6}}$ by left multiplying $\bar{B}$ by J_f.

$$B_f = J_f\, \bar{B} = \begin{bmatrix} -\mathrm{K_{t_b}} & -\mathrm{K_{t_s}} & -\mathrm{K_{t_b}} & -\mathrm{K_{t_s}} & 0 & 0 \\ 0 & \mathrm{K_{t_s}d_s} & 0 & -\mathrm{K_{t_s}d_s} & -\mathrm{K_{m_s}}\omega^2_{2,0} & \mathrm{K_{m_s}}\omega^2_{4,0} \\ \mathrm{K_{t_b}d_b} & 0 & -\mathrm{K_{t_b}d_b} & 0 & 0 & 0 \\ -\mathrm{K_{m_b}} & -\mathrm{K_{m_s}} & \mathrm{K_{m_b}} & \mathrm{K_{m_s}} & -\mathrm{K_{t_s}d_s}\omega^2_{2,0} & \mathrm{K_{t_s}d_s}\omega^2_{4,0} \end{bmatrix} \tag{3.20}$$

3.3 Simple Control Allocation

3.3.1 Pseudo-Inverse Control Allocation

Control allocation matrix, P_{ca}, maps the thrust/moment inputs to the rotor and servo control parameters. The rank of control effectiveness matrix, B_f is 4, i.e., it is not a full rank matrix. Control allocation matrix, P_{ca}, is not unique. One possible control allocation matrix can be obtained by calculating the pseudo-inverse of B_f, given in (3.21). This will result in a minimum norm solution, which may not be the minimum power solution.

$$P_{ca} = B_f^T (B_f \, B_f^T)^{-1} \tag{3.21}$$

Pseudo-inverse control allocation matrix is calculated only once in the initiliazion of the autopilot software. Therefore, in real-time control system, (3.21) will not consume CPU time. Control allocation matrix will map the desired force and torque commands to the motor parameters with $v = P_{ca}\tau$. Combining this with the (3.6), we obtain (3.22) as follows;

$$u = u_0 + P_{ca}\,\tau \tag{3.22}$$

where u_0 is the equilibrium point input vector for the linearized system.

3.3.2 Simplified Pseudo-Inverse Control Allocation

Now we perform some simplifications for a simpler and more robust autopilot in terms of implementation. These simplifications are not ideal and introduce some errors in control allocation. But these errors can be treated as input disturbances which will be compensated by feedback control. The assumptions for simplification are as follows;

- The yaw moment resulting from the thrust terms of 2nd and 4th rotors will dominate all the yaw moment resulting from the reaction torques of 1st, 2nd, 3rd and 4th rotors. Therefore, assume that the yaw moment depends only on the angles of ξ_1 and ξ_2.

- The roll moment resulting from the reaction torque of small rotors (2nd and 4th) are negligible.

Then, the simplified control effectiveness matrix becomes as follows:

$$B_f = \begin{bmatrix} -\mathrm{K}_{\mathrm{t_b}} & -\mathrm{K}_{\mathrm{t_s}} & -\mathrm{K}_{\mathrm{t_b}} & -\mathrm{K}_{\mathrm{t_s}} & 0 & 0 \\ 0 & \mathrm{K}_{\mathrm{t_s}}\,\mathrm{d_s} & 0 & -\mathrm{K}_{\mathrm{t_s}}\,\mathrm{d_s} & 0 & 0 \\ \mathrm{K}_{\mathrm{t_b}}\,\mathrm{d_b} & 0 & -\mathrm{K}_{\mathrm{t_b}}\,\mathrm{d_b} & 0 & 0 & 0 \\ 0 & 0 & 0 & 0 & -\mathrm{K}_{\mathrm{t_s}}\,\mathrm{d_s}\,\omega_{2,0}^2 & \mathrm{K}_{\mathrm{t_s}}\,\mathrm{d_s}\,\omega_{4,0}^2 \end{bmatrix} \tag{3.23}$$

The null space of B_f is:

$$\text{Null}(B_f) = \begin{bmatrix} -\frac{\mathrm{K}_{\mathrm{t_s}}}{\mathrm{K}_{\mathrm{t_b}}} & 0 \\ 1 & 0 \\ -\frac{\mathrm{K}_{\mathrm{t_s}}}{\mathrm{K}_{\mathrm{t_b}}} & 0 \\ 1 & 0 \\ 0 & \frac{\omega_{4,0}^2}{\omega_{2,0}^2} \\ 0 & 1 \end{bmatrix} \tag{3.24}$$

The rank of B_f is 4. Control allocation matrix, P_{ca}, is not unique. One possible control allocation matrix can be obtained by calculating the pseudo-inverse (this will result in minimum norm solution, which may not be the minimum energy solution);

$$P_{ca} = B_f^T (B_f\, B_f^T)^{-1} \tag{3.25}$$

Then, the mapping from desired force/torque to rotor/servo parameters are obtained as follows:

$$u = u_0 + P_{ca}\,\tau$$

$$\begin{bmatrix} \omega_1^2 \\ \omega_2^2 \\ \omega_3^2 \\ \omega_4^2 \\ \xi_1 \\ \xi_2 \end{bmatrix} = \begin{bmatrix} \omega_{1,0}^2 \\ \omega_{2,0}^2 \\ \omega_{3,0}^2 \\ \omega_{4,0}^2 \\ 0 \\ 0 \end{bmatrix} + \begin{bmatrix} -\frac{K_{t_b}}{2\left({K_{t_b}}^2+{K_{t_s}}^2\right)} & 0 & \frac{1}{2\,K_{t_b}\,d_b} & 0 \\ -\frac{K_{t_s}}{2\left({K_{t_b}}^2+{K_{t_s}}^2\right)} & \frac{1}{2\,K_{t_s}\,d_s} & 0 & 0 \\ -\frac{K_{t_b}}{2\left({K_{t_b}}^2+{K_{t_s}}^2\right)} & 0 & -\frac{1}{2\,K_{t_b}\,d_b} & 0 \\ -\frac{K_{t_s}}{2\left({K_{t_b}}^2+{K_{t_s}}^2\right)} & -\frac{1}{2\,K_{t_s}\,d_s} & 0 & 0 \\ 0 & 0 & 0 & -\frac{\omega_{2,0}^2}{K_{t_s}\,d_s\left({\omega_{2,0}^2}^2+{\omega_{4,0}^2}^2\right)} \\ 0 & 0 & 0 & \frac{\omega_{4,0}^2}{K_{t_s}\,d_s\left({\omega_{2,0}^2}^2+{\omega_{4,0}^2}^2\right)} \end{bmatrix} \begin{bmatrix} f_z \\ \tau_x \\ \tau_y \\ \tau_z \end{bmatrix} \tag{3.26}$$

3.3.3 Results: General Forces and Moments

The following results are valid when the simplifications previously discussed in Section 3.3.2 are accepted and the system is around the hovering state equilibrium point (See Eqs. 3.1, 3.2).

In autopilot, there will exist position and rate closed loop controllers which will manipulate the f_z, τ_x, τ_y and τ_z. So, the uncertainties in the parameters of K_{t_b}, K_{t_s}, K_{m_b}, K_{m_s}, d_b, d_s will be compensated by adjusting the controller parameters.

3.3.3.1 Force in z-axis

$$\tau = \begin{bmatrix} f_z \\ 0 \\ 0 \\ 0 \end{bmatrix} \tag{3.27}$$

$$u = u_0 + P_{ca}\,\tau$$

$$\begin{bmatrix} \omega_1^2 \\ \omega_2^2 \\ \omega_3^2 \\ \omega_4^2 \\ \xi_1 \\ \xi_2 \end{bmatrix} = \begin{bmatrix} \omega_{1,0}^2 \\ \omega_{2,0}^2 \\ \omega_{3,0}^2 \\ \omega_{4,0}^2 \\ 0 \\ 0 \end{bmatrix} + \begin{bmatrix} -\frac{\mathrm{K_{t_b}\,fz}}{2\left(\mathrm{K_{t_b}}^2+\mathrm{K_{t_s}}^2\right)} \\ -\frac{\mathrm{K_{t_s}\,fz}}{2\left(\mathrm{K_{t_b}}^2+\mathrm{K_{t_s}}^2\right)} \\ -\frac{\mathrm{K_{t_b}\,fz}}{2\left(\mathrm{K_{t_b}}^2+\mathrm{K_{t_s}}^2\right)} \\ -\frac{\mathrm{K_{t_s}\,fz}}{2\left(\mathrm{K_{t_b}}^2+\mathrm{K_{t_s}}^2\right)} \\ 0 \\ 0 \end{bmatrix} \tag{3.28}$$

3.3.3.2 Roll torque

$$\tau = \begin{bmatrix} 0 \\ \tau_x \\ 0 \\ 0 \end{bmatrix} \tag{3.29}$$

$$u = u_0 + P_{ca}\,\tau$$

$$\begin{bmatrix} \omega_1^2 \\ \omega_2^2 \\ \omega_3^2 \\ \omega_4^2 \\ \xi_1 \\ \xi_2 \end{bmatrix} = \begin{bmatrix} \omega_{1,0}^2 \\ \omega_{2,0}^2 \\ \omega_{3,0}^2 \\ \omega_{4,0}^2 \\ 0 \\ 0 \end{bmatrix} + \begin{bmatrix} 0 \\ \frac{\tau_\mathrm{x}}{2\,\mathrm{K_{t_s}\,d_s}} \\ 0 \\ -\frac{\tau_\mathrm{x}}{2\,\mathrm{K_{t_s}\,d_s}} \\ 0 \\ 0 \end{bmatrix} \tag{3.30}$$

3.3.3.3 Pitch torque

$$\tau = \begin{bmatrix} 0 \\ 0 \\ \tau_y \\ 0 \end{bmatrix} \tag{3.31}$$

$$u = u_0 + P_{ca}\,\tau$$

$$\begin{bmatrix} \omega_1^2 \\ \omega_2^2 \\ \omega_3^2 \\ \omega_4^2 \\ \xi_1 \\ \xi_2 \end{bmatrix} = \begin{bmatrix} \omega_{1,0}^2 \\ \omega_{2,0}^2 \\ \omega_{3,0}^2 \\ \omega_{4,0}^2 \\ 0 \\ 0 \end{bmatrix} + \begin{bmatrix} \frac{\tau_y}{2\,K_{t_b}\,d_b} \\ 0 \\ -\frac{\tau_y}{2\,K_{t_b}\,d_b} \\ 0 \\ 0 \\ 0 \end{bmatrix} \tag{3.32}$$

3.3.3.4 Yaw torque

$$\tau = \begin{bmatrix} 0 \\ 0 \\ 0 \\ \tau_z \end{bmatrix} \tag{3.33}$$

$$u = u_0 + P_{ca}\,\tau$$

$$\begin{bmatrix} \omega_1^2 \\ \omega_2^2 \\ \omega_3^2 \\ \omega_4^2 \\ \xi_1 \\ \xi_2 \end{bmatrix} = \begin{bmatrix} \omega_{1,0}^2 \\ \omega_{2,0}^2 \\ \omega_{3,0}^2 \\ \omega_{4,0}^2 \\ 0 \\ 0 \end{bmatrix} + \begin{bmatrix} 0 \\ 0 \\ 0 \\ 0 \\ -\frac{\tau_z\,\omega_{2,0}^2}{K_{t_s}\,d_s\left(\omega_{2,0}^{2\,2}+\omega_{4,0}^{2\,2}\right)} \\ \frac{\tau_z\,\omega_{4,0}^2}{K_{t_s}\,d_s\left(\omega_{2,0}^{2\,2}+\omega_{4,0}^{2\,2}\right)} \end{bmatrix} \tag{3.34}$$

3.4 Autopilot and Simulation Results

In order to verify the feasibility of the proposed design, the nonlinear system (Eq. 2.34) has been simulated with realistic parameters in a MATLAB/SIMULINK environment. After building the prototype, those parameters may change. The HLAV and the propulsion system parameters are given in Table 3.1.

Controllers consist of traditional cascaded PIDs (proportional-integral-derivative).

Table 3.1: HLAV and propulsion system parameters used in simulation

Description	***Symbol***	***Value***	***Unit***
Total mass	m	7.293	kg
Central principal moment of inertia	I_{xx}	0.13	kg·m^2
Central principal moment of inertia	I_{yy}	0.25	kg·m^2
Central principal moment of inertia	I_{zz}	0.55	kg·m^2
Propeller radius	r_b	0.41	m
Propeller radius	r_s	0.20	m
Distance from mass center	d_b	0.55	m
Distance from mass center	d_s	0.45	m
Thrust coefficient	K_{t_b}	0.001	N·s^2/rad^2
Thrust coefficient	K_{t_s}	6.6e-05	N·s^2/rad^2
Torque coefficient	K_{m_b}	3.04e-05	Nm·s^2/rad^2
Torque coefficient	K_{m_s}	9.66e-07	Nm·s^2/rad^2
Max angular velocity	$\max(\omega_{1,3})$	372	rad/s
Max angular velocity	$\max(\omega_{2,4})$	770	rad/s

From position control, desired roll and pitch angles (ϕ_d, θ_d) are produced such that vehicle velocity does not exceed 5 m/s and roll and pitch angles do not exceed 0.3 rad. Attitude control stabilizes the vehicle and executes the desired angle commands. Desired altitude thrust is limited by 0.75 of the maximum thrust of the rotors so that the remaining thrust is left as a buffer for orientation control. In control allocator block, desired thrust and torque commands are mapped to rotor/servo parameters by $u = u_0 + P_{ca}\,\tau$ (Eq. 3.22). Equilibrium point, $u_0 = \left(\omega_{1,0}^2\ \omega_{2,0}^2\ \omega_{3,0}^2\ \omega_{4,0}^2\ \xi_{1,0}\ \xi_{2,0}\right)^T$, is selected such that, in hover, big rotors carry the 0.85 of total mass and small rotors carry the 0.15 of the total mass.

According to simulation results given in Fig. 3.1, multicopter is stable and trajectory tracking performance is sufficient. From inner to outer, the cascaded control loops are as follows; angular velocity (Fig. 3.2), attitude (Fig. 3.3), linear velocity (Fig. 3.4) and position (Fig. 3.5), in decreasing closed-loop control bandwidths. According to propeller angular velocities given in Fig. 3.6, the system can be controlled with small

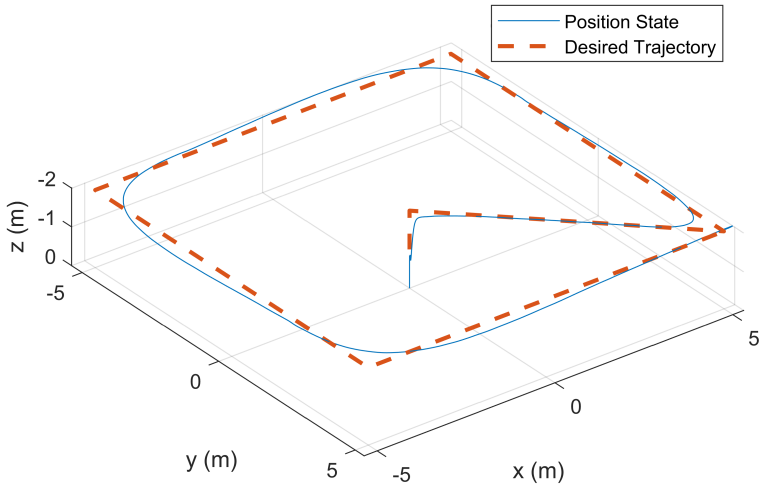

Figure 3.1: Trajectory tracking result

variations in motor speeds. As the disturbances such as wind increase, the variations in motor speeds will increase. Servo motor angles are given in Fig. 3.7. The main purpose of servo motors is to control the yaw axis. Angles ξ_1 and ξ_2 are mostly inverse of each other. This is why we need two separate tilting rotors instead of using the same tilting (1 servo motor) for both small rotors.

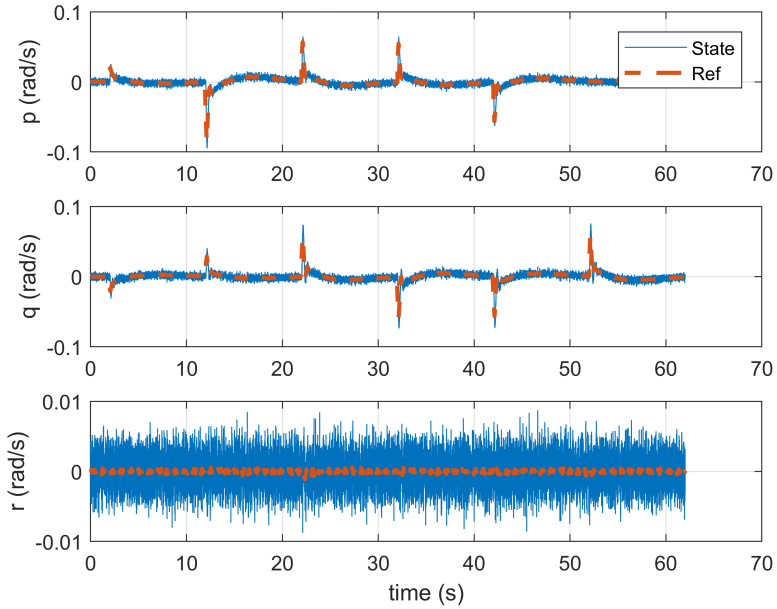

Figure 3.2: Angular velocity control

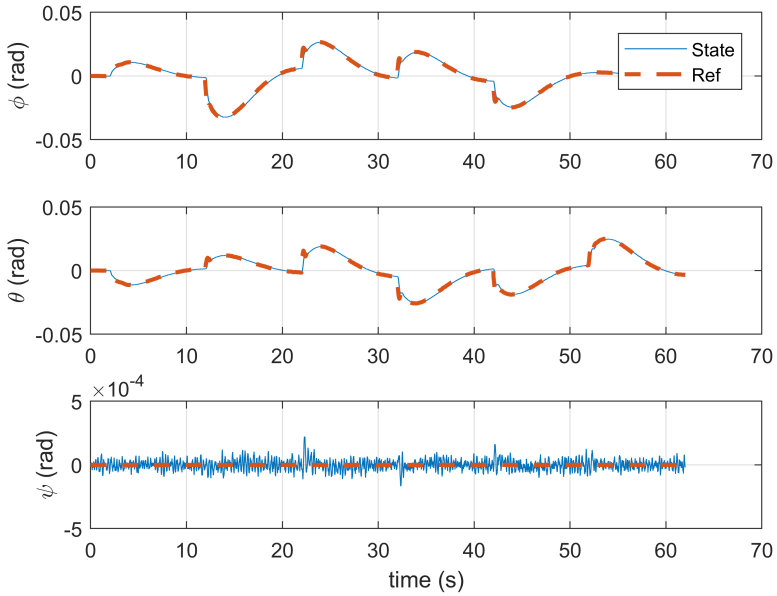

Figure 3.3: Attitude control

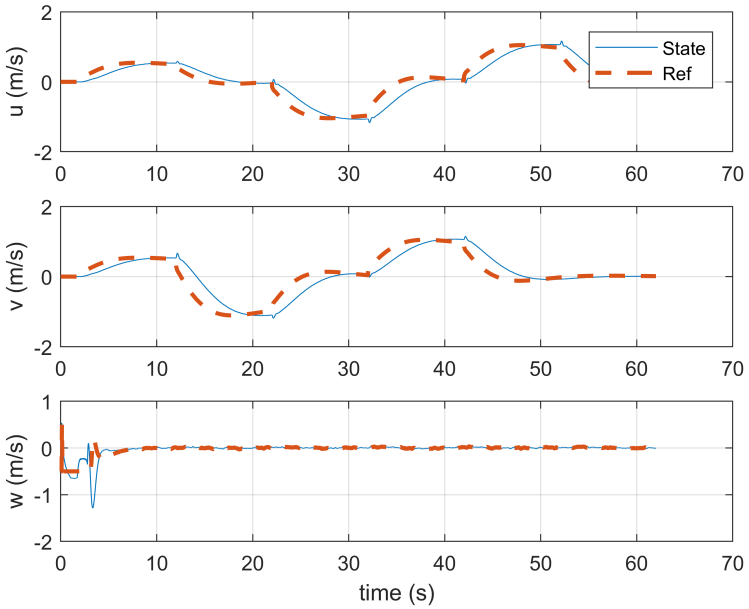

Figure 3.4: Linear velocity control

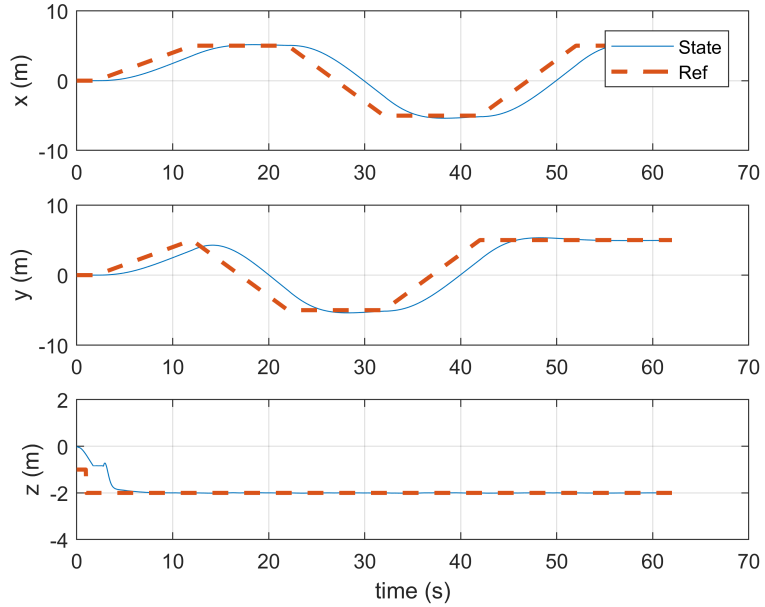

Figure 3.5: Position control

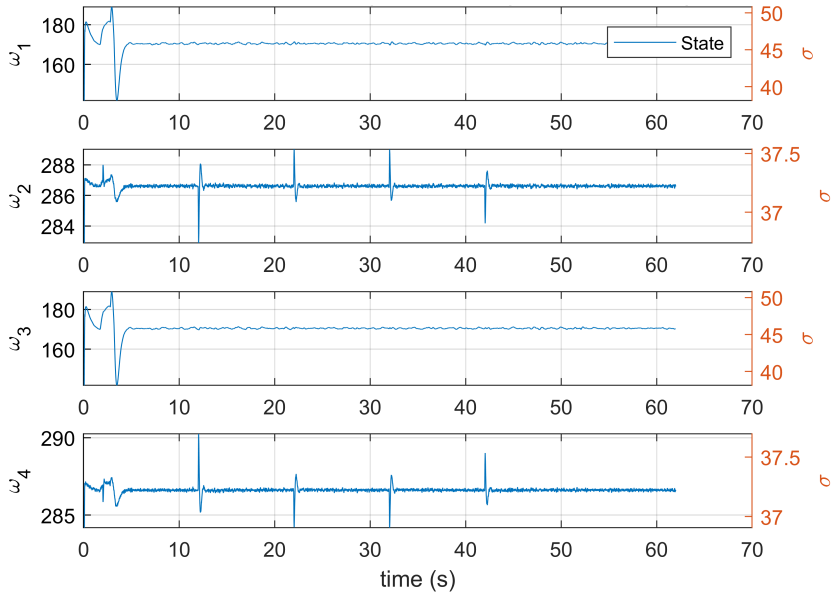

Figure 3.6: Brushless motor control (left: rad/s, right: throttle %)

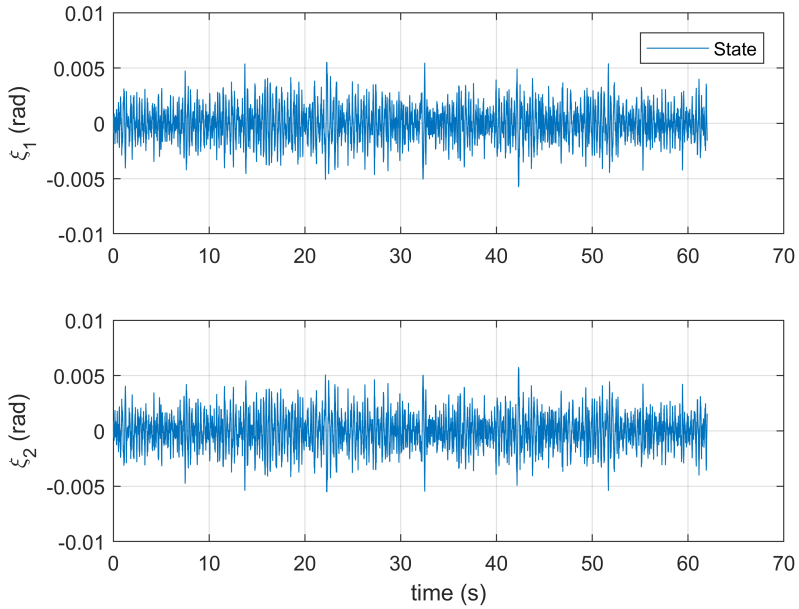

Figure 3.7: Servo motor control

CHAPTER 4

ADVANCED CONTROL ALLOCATION DESIGN

This chapter discusses improved control allocation strategies and shows how the control allocation strategy based on quadratic programming can be developed to utilize HLAV capacity in maximum performance with optimal power. The pseudo-inverse control allocation method, discussed in the previous Chapter 3, has some weaknesses and does not utilize the full available control set in the hover state which reduces the robustness of HLAV to large disturbances. It does not necessarily generate optimal performing input sets for effectors. It may also fail in maneuvering vehicle states and in other states different from the hovering state. This chapter dives into this area and develops advanced control allocation algorithms. This chapter starts with a description of control system architecture in Section 4.1. Section 4.2 formulates a general control allocation problem. In Section 4.3, an optimization problem is reformulated according to the requirements and properties of HLAV. Algorithms to find the maximum attainable control set are given as pseudocode. It is shown that the control allocation strategy based on quadratic programming for HLAV utilizes the attainable control set better overall than the pseudo-inverse control allocation method. Implementation issues and practical considerations are discussed.

4.1 Control System Structure

The control algorithm architecture can be designed in three levels for the over-actuated dynamic systems which is summarized in Fig. 4.1, and can be further explained as follows;

- The first block is a high-level controller that produces virtual control signals

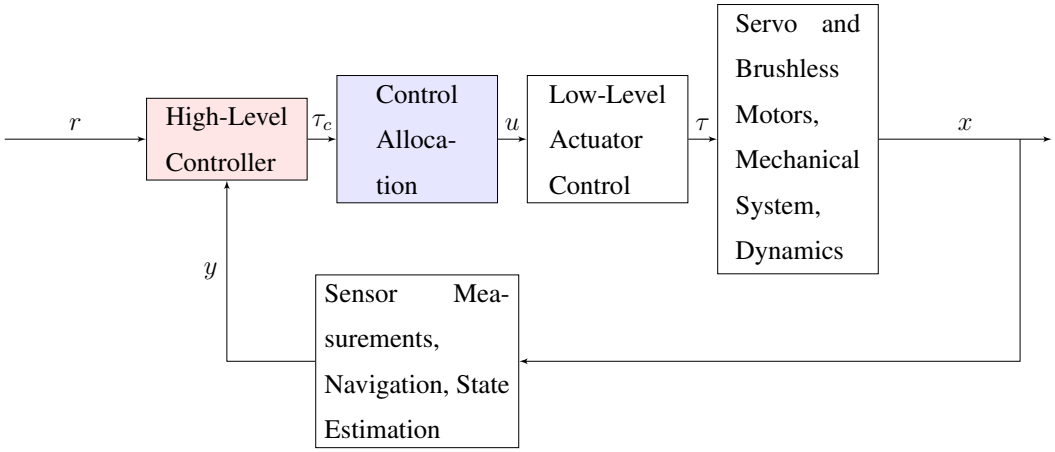

Figure 4.1: Control system structure

(i.e. moments and forces) to accomplish the desired motion.

- The second block is a control allocation algorithm that manages redundant effectors together (i.e. rotors, servo motors) to achieve the desired virtual reference commands, coming from the first block.

- The third block consist of low-level controllers which control each effector individually. This step is usually shipped in motor driver card and includes current control of each motor.

We mostly follow the nomenclature presented in [20]; $\tau_c \in \mathbb{T} \subset \mathbb{R}^m$ is the commanded virtual control effort, and $\mathbb{T}$ is the reachable set of virtual control efforts. $u \in \mathbb{U} \subset \mathbb{R}^p$ is the control input, and $\mathbb{U}$ is the constraints due to actuators limits. $\tau \in \mathbb{T} \subset \mathbb{R}^m$, actual allocated control effort. $x \in \mathbb{R}^n$, is the state vector. $y \in \mathbb{R}^m$, is the outputs, desired to be controlled.

4.2 Control Allocation Algorithm

Control allocation can be defined as distributing the redundant control effectors together to achieve the desired virtual control efforts. Control allocation has a matter of high importance, notably for control design of land, sea, or aerial vehicles [12–17], and their fault tolerance analysis [18]. Some control allocation methods are; direct

allocation method, daisy chaining, pseudo-inverse [19]. When the control allocation problem is formulated as an optimization problem, references [17, 20–28] discuss various methods of solving it. Iterative numerical linear programming (LP) or quadratic programming (QP) algorithms are possible. Some popular methods are simplex, active-set, interior point, fixed-point.

In this study, optimization-based control allocation algorithms are studied, as they are a highly promising area of research due to the increasing computational power of embedded computers.

Effector models can be commonly approximated as linear systems in u such that;

$$\tau = h(u, x, t) = B_f(x, t)u \tag{4.1}$$

where $B_f \in \mathbb{R}^{m \times p}$ is the same control effectiveness matrix defined in (3.3). Notice that, B_f depends on the state matrix, inputs vector, and parameters that change over time. Thus, B_f is regularly adjusted in the control allocation optimization to cover various flight states besides hovering state.

In over-actuated systems in which $p > m$, solutions of finding $u \in \mathbb{U}$ given $\tau = \tau_c$ may be infinite. It is advantageous to exploit the feature of the ill-posed inverse problem in some possible ways;

- It gives a chance to achieve secondary goals such as "power efficiency" or "minimizing wear and tear".

- Fault resistant system can be designed and actuator constraints can be dealt with more freedom.

We can formulate a general control allocation problem as follows [20];

$$
\begin{aligned}
&\text{minimize}(u, s); && \|Qs\| + J(x, u, t)) \\
&\text{where;} \\
&\qquad\qquad s &&= \tau_c - h(u, x, t) \\
&\qquad J(x, u, t) &&= \tfrac{1}{2}\left(u - u_p\right)^T W \left(u - u_p\right) \\
&\qquad\qquad u &&= u_\ell + \Delta u \\
&\text{such that;} \\
&\qquad\qquad u &&\in \mathbb{U} \\
&\qquad\qquad \Delta u &&\in \mathbb{C}
\end{aligned}
\tag{4.2}
$$

Here, $\|.\|$ is some norm, usually selected as 1-norm, 2-norm, or ∞-norm. The priority of control allocation block is to find an input, u, such that $\tau = \tau_c$, i.e., the slack variable $s \to 0$. However, this goal may fail when actuator constraints do not allow it. In this case, Q can be used as a weight matrix to prioritize the elements of τ_c among themselves.

Actuator limits are modeled in an optimization problem with $u \in \mathbb{U}$. The static actuator model is common in the literature, i.e., actuators are approximated to have infinite control bandwidth. However, it is better to consider the actuator dynamics, in the optimization problem. This can be implemented using the rate constraints for the input, by saturating the change in input by $\Delta u \in \mathbb{C}$ from the last control input, u_ℓ.

Since we have an over-actuated system, we have the freedom to meet secondary objectives when $\|Qs\|$ is reduced to zero. This is realized by using the J which represents secondary objectives. Vector u_p is the preferred value of u, and the weighting matrix, $W \in \mathbb{R}^{p \times p}$. W should be designed fairly small relative to Q to reflect prioritization.

4.3 Quadratic Programming Control Allocation Implementation for HLAV

The control allocation algorithm design takes into account the specific characteristics of the HLAV system (See Fig. 1.1), for optimal performance. Large propellers are more efficient than small propellers owing to their greater disk area. For this reason, the main lifting will be achieved by two large propellers. The basic motion control

objectives of the flight control system are 3 attitudes and 1 vertical stability, then the dimension of the virtual control state is $m = 4$. We have more effectors, $p = 6$, than the motion control goals, $p > m$.

The control allocation problem is developed as a parametric program in Eq. (4.2). Some important points to take into consideration while tuning the parameters are as follows;

- Roll and pitch control are slightly more important for flight safety than altitude control, and similarly, altitude control is more important than yaw control. This requirement should be reflected in Q matrix.
- J represents secondary objectives. For this reason, W should be designed fairly small relative to Q.
- Preferred value, u_p is zero angle for the servo motors and minimum energy hover thrust for each propulsion system.
- Small rotor propulsion systems are less efficient for weight lifting than big rotor propulsion systems. This priority is reflected in W.
- The sets $\mathbb{U}$ and $\mathbb{C}$ are chosen according to saturation and rate limits of each effector.

In (4.1), we have approximated the nonlinear model as a linear effector model, that will bring some minor error in finding the optimal solution. But thanks to that, we have freed ourselves from nonlinearities which could lead to a non-convex cost function, and optimization being stuck in local minimums. In the linear effector model, the optimal solution of a linear programming problem lies at one of the vertices of the feasible set, which results in using a smaller number of effector use in vehicle control which is an undesired property. Multicopters work on the principle of differential control. Therefore, in this study, we preferred a quadratic programming approach which favors using evenly distributed control effort on effectors. Optimization problem formulation, (4.2), can be reformulated as follows [20];

$$\min_{u,s} \left(\sum_{i=1}^{m} q_i s_i^2 + \sum_{j=1}^{p} w_j u_j^2 \right) \tag{4.3}$$

such that;

$$B_f u = \tau_c + s, \quad u_{\min} \leq u \leq u_{\max}, \delta_{\min} \leq u - u_\ell \leq \delta_{\max} \tag{4.4}$$

This formulation can be converted into a standard quadratic programming form as follows [20];

$$\min_{u,s} \frac{1}{2} \left(u^T, s^T\right) H \begin{pmatrix} u \\ s \end{pmatrix} \tag{4.5}$$

such that;

$$(B_f, -I) \begin{pmatrix} u \\ s \end{pmatrix} = \tau_c \tag{4.6}$$

$$\begin{pmatrix} I, & 0 \\ -I, & 0 \end{pmatrix} \begin{pmatrix} u \\ s \end{pmatrix} \geq \begin{pmatrix} \max\left(u_{\min}, u_\ell + \delta_{\min}\right) \\ -\min\left(u_{\max}, u_\ell + \delta_{\max}\right) \end{pmatrix} \tag{4.7}$$

where $H = 2 \cdot \mathrm{diag}\left(w_1, \ldots, w_p, q_1, \ldots, q_m\right)$.

Optimization-based control allocation has key challenges, such as implementation in an embedded system, verification, and validation. We can discuss two possible ways of implementation methods;

1. Real-time optimization. In a discrete-time control system, the control allocation block needs to be completed within a certain period of time, so some sub-optimality is inevitable if the search is not finished in time. In order to increase the convergence rate in optimization, the solution from the previous sample can be used as a starting search point, since the problem parameters do not vary considerably from the previous instance. We use MATLAB function "quadprog", and MATLAB Coder for C++ code generation and implementation. Single objective algorithms suit more to real-time implementation.

2. Using look-up tables. For various vehicle states, x, and reference commands, τ_c, the optimization problem can be solved offline and the generated look-up tables can be stored in RAM. This method requires excessive memory for the flight controller cards, but interpolation between look-up tables is possible. Some advantages are; execution time will be much faster, and since control

allocation will not rely on an online optimization algorithm to succeed, the reliability of the system will increase. Time-consuming multi-objective optimization algorithms are possible since optimization problems are solved offline.

We implement the quadratic programming, described in (4.5), (4.6), (4.7) and find the maximum attainable control set in each direction for the nominal hovering conditions without exceeding saturation limits of effectors. In order to find the maximum control set allowed by the control allocation method in each direction, an additional optimization problem is simply solved. The pseudo-code explaining this two-layer optimization structure is given in the Algorithm 1 for the pseudo-inverse method and in the Algorithm 2 for the quadratic programming allocation method. This pseudocode allows the user to evaluate the dynamic capabilities of the HLAV system when using the corresponding allocation algorithm.

The vehicle and propulsion system parameters are given in Table 4.1.

Rate constraints, $\delta_{\max}$, and $\delta_{\min}$ are ignored for analysis purposes. Since the admissible set is 4-D, in order to visualize the solution set, we slice through attainable control set (ACS) at $F_z^N + mg = 0$, $L = 0$, $M = 0$, $N = 0$ and present the results in 3-D in Fig. 4.2 for better illustration. When quadratic programming solution set is compared with the classical Moore-Penrose pseudo-inverse solution for static control allocation problem, we observe that ACS volume is increased by between 2.8 to 5.4. For example, volume of torque envelope is increased from 22259.2 Nm^3 to 98872.1 Nm^3 in Fig. 4.2a.

When the vehicle is exposed to large disturbances, such as wind, etc., maximum control effort may be required. Also, during maneuvering flight, appropriate control allocation will permit greater stability margins and better stabilization. In these aspects, the optimization-based control allocation method presented in this study substantially improves the attainable control set for the HLAV system. We also show that the traditional pseudo-inverse method is very limited in exploiting the full capacity of the vehicle. It is important to note that control allocation is not a control law itself and it only indirectly affects the design parameters of the high-level controller, such as robust stability and performance, which is discussed in the next chapter.

Algorithm 1: Search for maximum attainable control-set for pseudo-inverse allocation method

Input: n // n^3: Number of directions, choose n > 20 for better resolution.

Output: Set_τ // available force and torque envelope

BEGIN // preallocate persistent variables and init. parameters

$D :=$ CreateNormalizedDirectionMatrix(n) // $D \in \mathbb{R}^{4\times n^3}$. D is a matrix containing every possible direction of control set. One of the rows in D is set to zero to slice at one of the followings: $F_z^N + mg = 0$, $L = 0$, $M = 0$, $N = 0$.

$D :=$ EliminateRedundantDirections(D) // the size of D is reduced for computation efficiency. $D \in \mathbb{R}^{4\times N}, N < n^3$

for $i :=$ 1 *to* N **do**

$\tau_c := D(:, i)$

$u_{unity} := P_{ca}\,\tau_c$ // Pseudo-inverse allocation, See Eq. 3.22

$f := -1$

$A := [-u_{unity}, u_{unity}]^T$

$b := [u_0 - u_{min}, u_{max} - u_0]^T$

$k :=$ LinProg(f, A, b) // $\min_k f^T k$ such that $\begin{cases} A \cdot k \le b \\ 0 \le k \end{cases}$

$u := u_0 + k \cdot u_{unity}$

$\dot{x} := f(x_0, u)$ // See Eq. 2.34

$\tau := [m, I_{xx}, I_{yy}, I_{zz}]^T \odot \dot{x}(9:12)$ // Element-wise multiplication, to find force and torque parameters from accelerations and inertia

$Set_\tau :=$ UpdateAttainableControlSet(Set_τ, τ)

return Set_τ

Algorithm 2: Search for maximum attainable control-set for quadratic-programming allocation method

Input: n // n^3: Number of directions, choose n > 20 for better resolution.

Output: Set_τ // available force and torque envelope

BEGIN // preallocate persistent variables and init. parameters

$D :=$ CreateNormalizedDirectionMatrix(n) // $D \in \mathbb{R}^{4\times n^3}$. D is a matrix containing every possible direction of control set. One of the rows in D is set to zero to slice at one of the followings: $F_z^N + mg = 0$, $L = 0$, $M = 0$, $N = 0$.

$D :=$ EliminateRedundantDirections(D) // the size of D is reduced for computation efficiency. $D \in \mathbb{R}^{4\times N}, N < n^3$

for $i :=$ 1 *to* N **do**

$\tau_c := D(:, i)$

Search $\underbrace{\max}_{k}(\|k \cdot \tau_c\|)$ such that;

$$\begin{cases} k > 0 \text{ // See Eq. 4.5, 4.6, 4.7 for QuadProgAllocation} \\ [u, s] := \text{QuadProgAllocation}(k \cdot \tau_c, B_f, u_{min}, u_{max}, w_{1\to p}, q_{1\to m}) \\ \|s\| < \epsilon \text{ // Small Number} \end{cases}$$

$\dot{x} := f(x_0, u)$ // See Eq. 2.34

$\tau := [m, I_{xx}, I_{yy}, I_{zz}]^T \odot \dot{x}(9:12)$ // Element-wise multiplication, to find force and torque parameters from accelerations and inertia

$Set_\tau :=$ UpdateAttainableControlSet(Set_τ, τ)

return Set_τ

Table 4.1: HLAV system parameters used in Control Allocation Analysis

Description	***Symbol***	***Value***	***Unit***
Total mass	m	7.293	kg
Principal moment of inertia	I_{xx}	0.13	kg·m^2
Principal moment of inertia	I_{yy}	0.25	kg·m^2
Principal moment of inertia	I_{zz}	0.55	kg·m^2
Propeller radius	r_b	0.41	m
Propeller radius	r_s	0.20	m
Distance from mass center	d_b	0.55	m
Distance from mass center	d_s	0.45	m
Thrust coefficient	K_{t_b}	0.001	N·s^2/rad^2
Thrust coefficient	K_{t_s}	6.6e-05	N·s^2/rad^2
Torque coefficient	K_{m_b}	3.04e-05	Nm·s^2/rad^2
Torque coefficient	K_{m_s}	9.66e-07	Nm·s^2/rad^2
Min / Max angular velocity	min/max$(\omega_{1,3})$	18/372	rad/s
Min / Max angular velocity	min/max$(\omega_{2,4})$	36/770	rad/s
Min / Max tilt angle	min/max$(\xi_{1,2})$	$\pm\pi/4$	rad

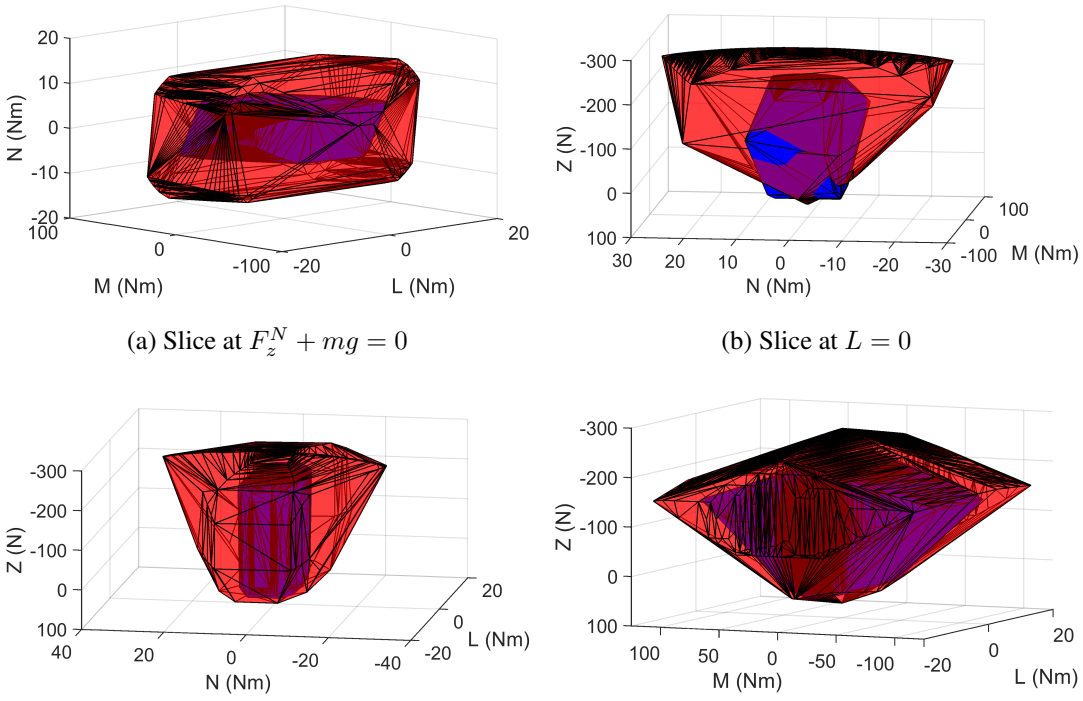

(a) Slice at $F_z^N + mg = 0$

(b) Slice at $L = 0$

(c) Slice at $M = 0$

(d) Slice at $N = 0$

Figure 4.2: Attainable control set (ACS) in hover state, Blue: Pseudo-Inverse, Red: Quadratic programming. Volume is increased by (a) 4.4 times for the ACS cut at $F_z^N + mg = 0$, (b) 3.6 times for the ACS cut at $L = 0$, (c) 5.4 times for the ACS cut at $M = 0$, (d) 2.8 times for the ACS cut at $N = 0$

CHAPTER 5

SYSTEM IDENTIFICATION AND HIGH LEVEL CONTROLLER DESIGN

This chapter consists of system identification and high-level controller design parts. In Section 5.1, model parameters are estimated using closed-loop system identification tools. The system under study is open-loop unstable. Therefore, frequency response function (FRF) measurements should be realized under closed-loop operation. Closed-loop identification issues are overcome with the following strategies; the indirect approach and direct approach with subspace methods. In Section 5.2, high-level controllers are designed with the "manual loop shaping" method in cascaded control loop structure to satisfy robust performance and stability. Analysis results are presented.

5.1 Identification of Aerial Vehicle for High-Level Controller

A mathematical model is the first step of simulation and control. A robust controller design requires a precise, unbiased measurement of FRF (frequency response function) and its uncertainty estimation [50]. A mechanical model designed in solid modeling CAD (computer-aided design) program, datasheet parameters of instruments, and theoretical system parameters can be used to develop nonlinear models. However, most parameters are hardly obtained or not available. System identification allows one to estimate models directly from measurement test data. The cross-couplings in the system presents difficulty on the SISO (single-input single-output) estimation, but most of them can be treated as disturbances.

Consider the following linear, dynamic system;

$$y(t) = G(q)u(t) + v(t) \tag{5.1}$$

The FRF measurement, $\widehat{G}(f)$;

$$\widehat{G}(f) = \frac{\widehat{S}_{yu}(f)}{\widehat{S}_{uu}(f)} \tag{5.2}$$

where $\widehat{S}_{yu}(f)$ is the output-input cross-spectrum and $\widehat{S}_{uu}(f)$ is the input spectrum. The estimate of $\widehat{G}(f)$ is bias free since the system presented in (5.1) is linear, there exist no input noise, and output noise is uncorrelated. The output noise spectrum (spectrum of $v(t)$) is given as follows [51]

$$\widehat{S}_{vv}(f) = \widehat{S}_{yy}(f) - \frac{|\widehat{S}_{yu}(f)|^2}{\widehat{S}_{uu}(f)} \tag{5.3}$$

Frequency response function measurement quality can be assessed using the coherence function;

$$\widehat{\gamma}^2_{yu}(f) = \frac{|\widehat{S}_{yu}(f)|^2}{\widehat{S}_{yy}(f)\widehat{S}_{uu}(f)} \tag{5.4}$$

Coherence below a value of 0.6 typically indicate poor measurement quality [45]. Bias and random errors become visible in a decrease of the coherence values at the affected frequencies.

The system under study is open-loop unstable. Therefore, experiments should be realized under closed loop control. There are known issues with closed-loop identification;

- Identifying the inverse of the controller, $-1/C$, when the reference spectrum can not excite the system enough compared to disturbances, [51];

$$\begin{aligned} \widehat{G} &= \frac{G_0\widehat{S}_{rr}(f) - C\widehat{S}_{vv}(f)}{\widehat{S}_{rr}(f) + |C|^2\widehat{S}_{vv}(f)} \\ \widehat{S}_{vv}(f) = 0 \quad &\Rightarrow \quad \widehat{G} = G_0 \\ \widehat{S}_{rr}(f) = 0 \quad &\Rightarrow \quad \widehat{G} = -1/C \end{aligned} \tag{5.5}$$

- Correlation between v, and u cause bias in estimation.

Closed loop identification issues can be overcome with the following strategies;

1. The Indirect Approach; We use controller information, C, to reconstruct an open-loop plant model from closed-loop response [51];

$$\widehat{G}_{ol} = \frac{\widehat{G}_{cl}(f)}{C(1 - \widehat{G}_{cl}(f))} \tag{5.6}$$

2. Direct approach with Subspace SSARX (Subspace identification based on autoregressive with exogenous variables modeling); We estimate a state-space model using the subspace algorithm SSARX which allows unbiased estimates [52], while using data collected in a closed-loop process. "SSARX" is a subspace identification method that uses an algorithm based on ARX (autoregressive with exogenous variables) estimation to calculate the weighting.

We perform the indirect approach system identification for 3 rotational axes and 1 translational axis in a closed-loop system where PID controller parameters are loosely tuned for the experiment. The pseudo-inverse method for the control allocation block is used. In the rest of the chapter, we present the results of the pitch and roll axis but the methodology followed for other axes are similar. Experiments are performed separately for each axis, in a 1-DOF test rig.

Excitation signal design is a crucial parameter for high-quality FRF measurements. In general, a high signal-to-noise ratio (SNR) excitation signal reduces bias error and noise in FRF measurement, reaching a specified accuracy in shorter time periods. However, excitation signal should not exceed normal operation conditions and saturation limits. The crest factor property given in (5.7) can be used to quantify the quality of the input signal [53]. Higher crest factor values indicate extreme peaks in the excitation signal.

$$C = \frac{|u_{\text{peak}}|}{u_{\text{rms}}} = \frac{\|u\|_\infty}{\|u\|_2} \tag{5.7}$$

Broadband perturbation signals can be categorized into three groups: transient signals; nontransient aperiodic signals; periodic signals [54]. Each category has its own advantages and disadvantages. The power spectrum of a periodic signal can be easily shaped. In addition, periodic signals do not produce a leakage error when measuring an integer number of signal periods [53]. Reducing noise variance in FRF measurements with averaging methods is also a common technique when frequency resolution is not a limiting parameter. Non-transient non-periodic signals will cause

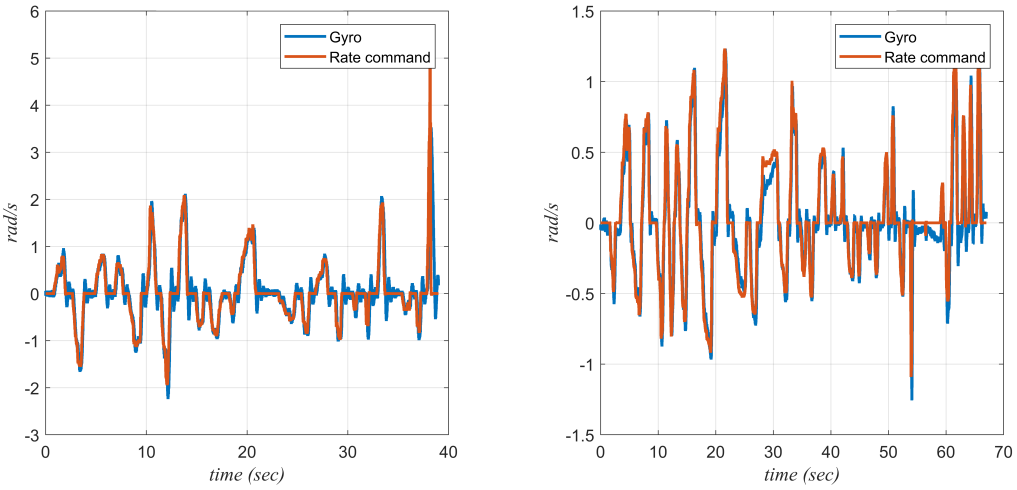

(a) Roll axis

(b) Pitch axis

Figure 5.1: Estimation data collected in closed loop control, input is rate command excitation signal and output is gyro measurement

leakage error, but if there is no restriction on the measurement time, the leakage error will decrease as the measurement time increases.

The system is excited at each axis with a rate command (deg/s) as input and angular velocity (deg/s) is measured synchronously as output in 250 Hz. Excitation signal injects power in the frequency range of interest 0.1 to 10 Hz. Aperiodic signals and periodic signals of swept sine, multi-sine, and PRBS (pseudo-random binary sequence) excitation signals proposed in [50] are developed for identification. Different data sets are used for validation and estimation. Input excitation signal and output measurement data are given in Fig. 5.1a, 5.1b.

For pitch and roll axes, closed-loop FRF measurements from angular rate command to gyro and disturbance spectrum with a confidence interval of 3 standard deviations (light blue color) are given in Fig. 5.2a, 5.2b. We also fit the nonparametric FRF measurement into a parametric model, transfer function of 2nd order, given by red color in Fig. 5.2a, 5.2b. The step response of estimated parametric model are given in Fig. 5.3a, 5.3b

In Fig. 5.4a, 5.4b, validation data set and closed-loop simulation are given. The rate

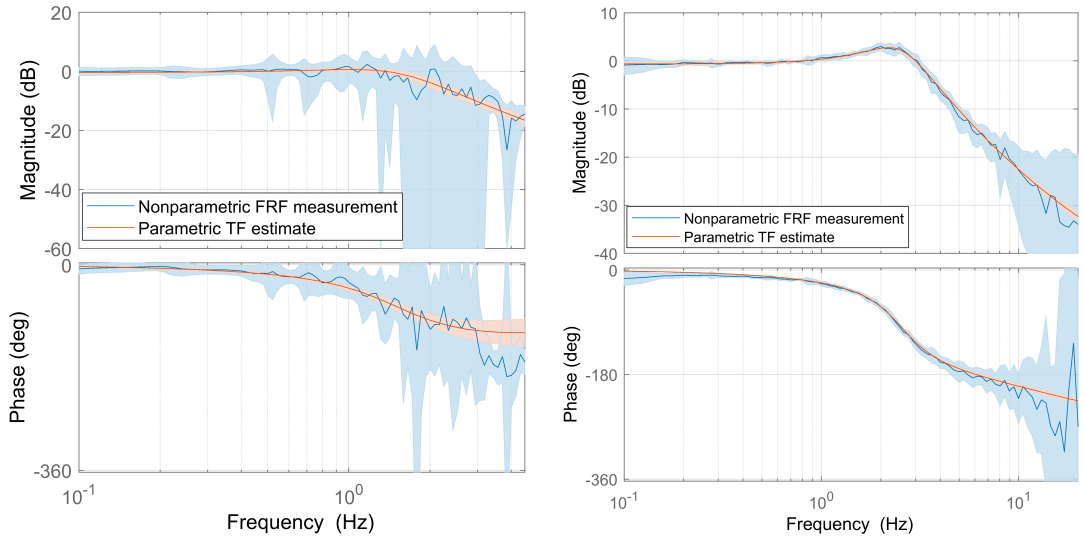

(a) Roll axis (b) Pitch axis

Figure 5.2: FRF measurement and 3σ uncertainty.

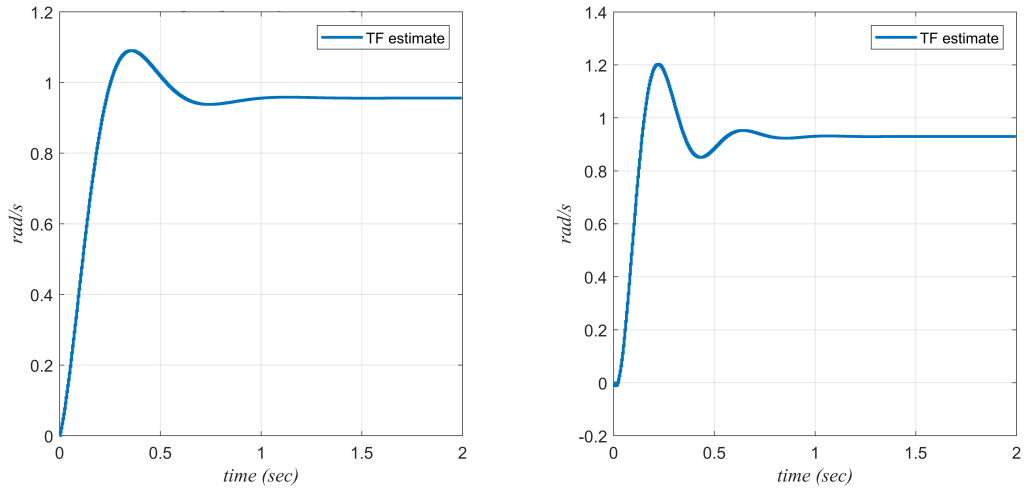

(a) Roll axis (b) Pitch axis

Figure 5.3: Step responses of estimated parametric transfer function models

response gives almost a perfect match, but it may be misleading, as it is mostly dominated by the controller. The rate response is less sensitive to changes in the open-loop model than the controller. However, the identification of the time delay is quite accurate.

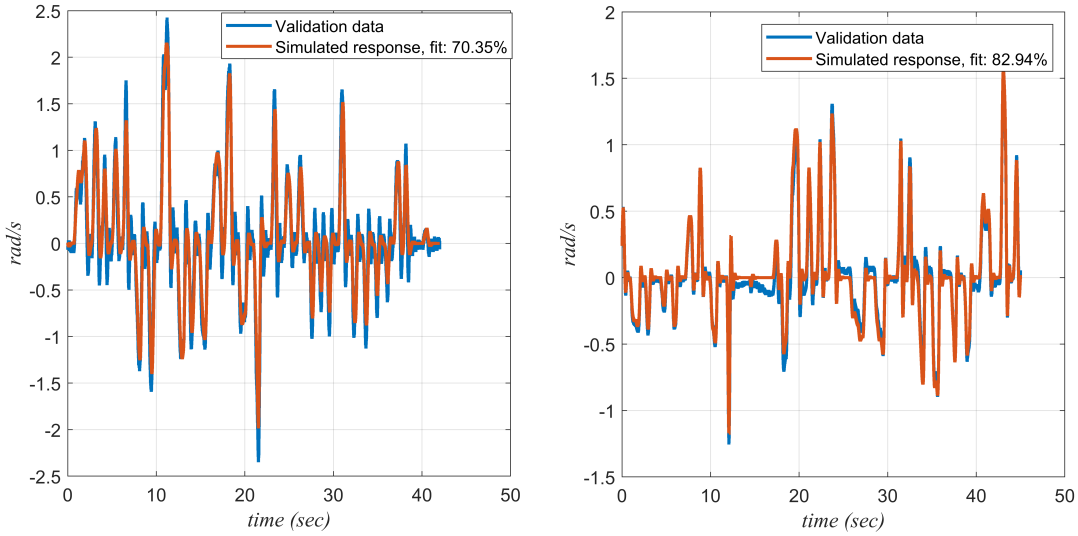

(a) Roll axis

(b) Pitch axis

Figure 5.4: Validation of closed loop model

The input of the open-loop system is the virtual torque command to the control allocation block and the output is the inertial angular rate. We estimate the open-loop state-space model from measurements collected in closed-loop. The subspace algorithm SSARX is compared with the indirect approach in Fig. 5.5a, 5.5b. When cross-coupling interactions are ignored, the mathematical model of the system for pitch axis can be simplified to $\frac{1}{I_{yy}s + B}$ where I_{yy} is inertia and B is the drag coefficient. Above the B/I_{yy} rad/s, the drag loses its significance and the magnitude slope is -20 dB/dec and the phase is -90 degrees as expected. Phase decreases more in higher frequencies due to time delay in the system. The same analysis is valid for the roll axis as well.

5.2 High Level Controller Design

Tiltrotor aerial vehicles are subjected to stability problems that make an efficient control system design fundamental [55]. For the high-level controller, controllers are designed in a cascaded control loop structure with the “manual loop shaping” method to satisfy robust performance and stability.

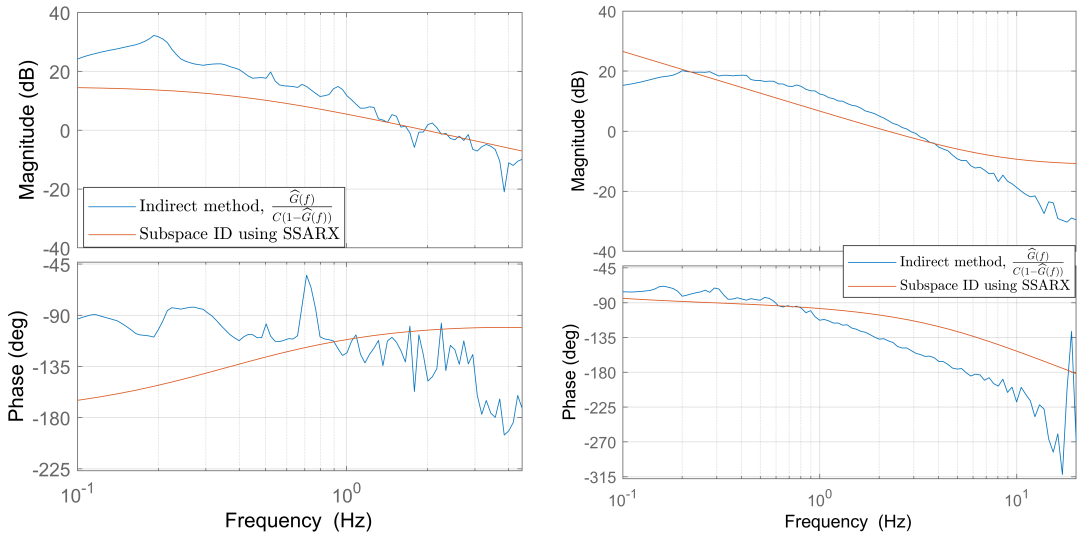

(a) Roll axis

(b) Pitch axis

Figure 5.5: Indirect approach and subspace method to estimate open loop system, with normalized magnitudes.

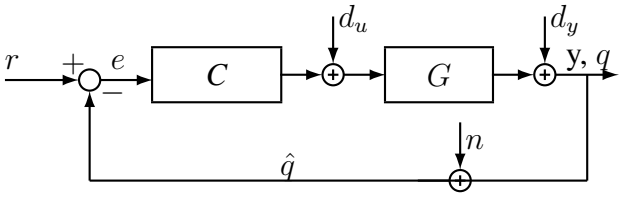

Figure 5.6: Inner rate loop control system structure.

A basic control system for rate loop control is given in Fig. 5.6. Some notions will be given as follows to explain properties of the control system;

$$L = G(s) \cdot C(s) \tag{5.8}$$

$$S = (1 + L)^{-1} \tag{5.9}$$

$$T = L \cdot (1 + L)^{-1} \tag{5.10}$$

where $C(s)$ is the rate loop controller under study and $G(s)$ is the open loop model identified in Section 5.1. S is the transfer function from output disturbance d_y, to output y or from reference r to error e. T is the complementary sensitivity function of r to y or n to y. L is the open loop transfer function from error e to output y. Control system can be designed considering the following principles and trade-offs;

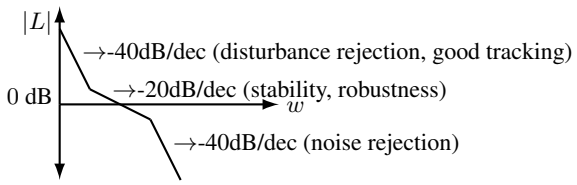

Figure 5.7: Desired loop shape.

- L should not exceed the value which satisfy nominal and robust stability.
- Sensitivity function is desired to be $S \to 0$ on low frequencies and be minimum on higher frequencies where output disturbance exists.
- We desire $T \to 1$, for good reference tracking.
- Noise effect on output measurements should be minimized, $T \to 0$.
- Controller should be strictly proper, $\lim_{\omega \to \infty} C = 0$.
- There is $S + T = 1$ constraint.

In order to satisfy these conflicting requirements, we aim for the open-loop shape given in Fig. 5.7.

The designed controller consists of the followings; 1 PI filter (with anti-windup implementation) to satisfy -40 dB/dec slope target shape which will allow high disturbance rejection in low frequencies, 1 lead filter with a critical frequency lying on crossover frequency of open-loop gain to increase phase margin, 1 low pass filter to reduce noise effects and be robust to unmodeled dynamics and reduce the vibrations in the system. Open-loop transfer functions, L, are given in Fig. 5.8a, 5.8b. The angular rate roll controller is designed such that the gain margin is 8.07 dB at 4.87 Hz, and the phase margin is 41.7 degrees at 1.37 Hz. The angular rate pitch controller is designed such that the gain margin is 12.6 dB at 7.54 Hz, and the phase margin is 45.2 degrees at 2.52 Hz. Output disturbance sensitivity function, S are given in Fig. 5.9a, 5.9b. According to S, for the pitch axis, an output disturbance at 0.5 Hz attenuates into 0.18 of its magnitude. Disturbances up to 2 Hz are rejected, 2-15 Hz range is amplified by 1-1.6 in magnitude which does not coincide with the propeller main disturbance frequencies. Above 15 Hz, the controller will have a minor effect on output disturbance.

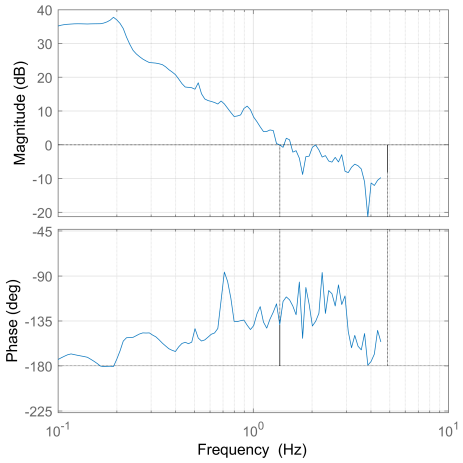

(a) Roll axis, GM = 8.07 dB (at 4.87 Hz), PM = 41.7 deg (at 1.37 Hz).

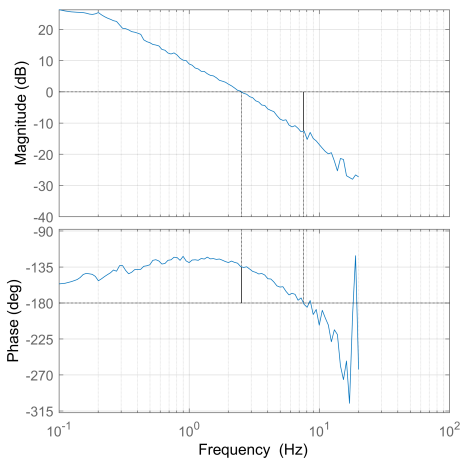

(b) Pitch axis, GM = 12.6 dB (at 7.54 Hz), PM = 45.2 deg (at 2.52 Hz).

Figure 5.8: Bode Diagram of open loop system, $L = G \cdot C$

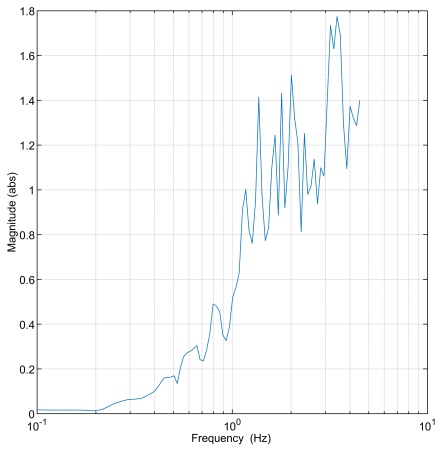

(a) Roll axis.

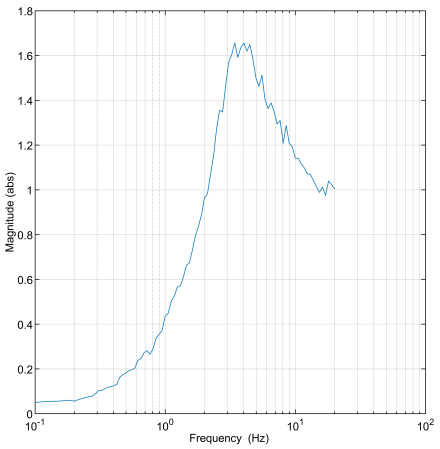

(b) Pitch axis.

Figure 5.9: Output disturbance sensitivity function of the feedback control system, $|1/(1+L)|$

After designing a satisfactory angular rate loop, the angular position loop is trivial. Position loop controller consists of a simple proportional gain and easily satisfies the control system requirements.

CHAPTER 6

COGGING TORQUE DISTURBANCE REJECTION AND CONTROLLER DESIGN FOR SERVO MOTOR

Chapter 6 attacks the cogging torque and friction disturbance rejection problem for the low-level controllers of servo motors to be used in tilt-rotor mechanism. Section 6.1 begins with a discussion and motivation followed by a brief literature review of developments. Precise positioning of servo motors that are used in tilt mechanism, is a crucial parameter for reducing vibrations in the HLAV and improve overall flight performance. Due to size and weight limitations, the motor is required to be small but torque density is desired to be high. In high torque and cheap PMSM and BLDC motors, cogging torque and friction are usually the main challenging disturbance sources. Section 6.2 gives an overview of the test and measurement setup. Cogging torque and friction can be identified using position sensors that already exist in the tilt mechanism, so the cost of the system is not increased. Current and speed controller designs are covered in Section 6.3. The controller implementation issues are examined in an embedded world with their practical considerations. The results of the cogging torque identification and compensation are presented in Section 6.4. The results of friction identification and compensation are reported in Section 6.5. This study shows that, by developing feedforward algorithms, with only cogging torque compensation, 30-65% of the tracking error can be removed in a feedback control system. The importance of the work is elaborated and applications and extensions are suggested in Section 6.6. The results presented in this chapter are published in our paper [40].

6.1 Discussion

In many robotic, and electro-optic gimbal systems, precise positioning, and high performance speed control are of great importance [56, 57]. Most of these applications do have volume constraints, therefore, electric motors are desired to be small but produced torque is required to be high. One way to achieve this is to use ratio-driven systems, such as gear, belts, or screw mechanisms. However, backlash in ratio-driven motor systems prevents precise positioning. Other disadvantages are increased friction, mechanism complexity, and lower torsional resonant frequencies. On the other hand, direct-drive motors provide greater torsional stiffness, less motion transmission errors, and no backlash [58]. Due to size and cost limitations and torque requirements, generally, direct-drive PMSM (Permanent Magnet Synchronous Motor) and BLDC (Brushless DC electric motor) motors are preferred in robotic systems which are able to produce high torque in small size. The PMSM and BLDC motors have similar construction with permanent magnet rotors and polyphase stator windings. The PMSM motor has a sinusoidal distribution of windings resulting in a sinusoidal B-EMF (counter-electromotive force) waveform, whereas the BLDC motor has a rectangular distribution of windings resulting in trapezoidal B-EMF waveform.

Torque ripple in PMSM and BLDC motors is a common problem that notably degrades the system performance [59]. Four main torque sources are as follows; mutual torque, reluctance torque, cogging, and friction. Any mismatch in the B-EMF waveform and stator's current waveform contributes to torque ripple. Therefore, PMSM motors are driven with sinusoidal current waveform, generally with FOC (field-oriented-control) method, and BLDC motors are driven with trapezoidal current waveform. Both mutual and reluctance torque are produced when the motor is energized. When the current is zero, they do not exist. Contrarily, cogging torque and friction occur also in un-energized motors. Cogging torque, also known as detent torque, arises from the attraction of the rotor magnets to the steel teeth on the stator. In the presence of cogging, the rotor tends to align itself in a number of stable points (depending on the number of poles), resulting in reduced controller performance, apparent particularly at light load and low speed. Cogging torque is position dependent, whereas friction torque is a velocity dependent nonlinear disturbance. When the mo-

tor rotation direction is inverted, cogging torque does not change but friction torque does.

In the literature, various techniques for producing a specified average torque with minimal torque ripple and minimum average current power are considered and discussed [60–62]. These are current related torque ripples which can be reduced by finding optimal current waveform taking into account motor structure and measured or theoretical B-EMF waveform profile of stator windings. The effect of magnet pole shaping and magnet arc length on the output torque and torque ripple is discussed by [63]. The influence of motor design parameters (the slot and the pole number, the width of the stator slot openings, the magnet arc, skew angle, etc.) for the minimization of cogging torque is examined in [64]. Skewing the stator slots is an effective method to reduce cogging torque, but the manufacturing cost is increased and the maximum available torque is decreased. Slotless and coreless motors do not have cogging torque, but again, the manufacturing cost increases, and produced torque in the same size decreases dramatically. For high torque, small size, and cheap BLDC and PMSM motors, cogging torque and friction are two main disturbance sources. Therefore, this study focuses on the identification and rejection of cogging torque and friction disturbances.

The motivation of this study is to aid feedback controllers with feedforward methods to minimize cogging and friction disturbance, show the significant improvements in controller performance of a low-cost small-size brushless motor, and discuss the results. Cogging torque and friction can be measured by using a torque sensor, but this will increase the cost of the system. In this study, cogging torque and friction are identified using a position sensor which already exists in precise positioning robotic systems, so the cost of the system is not increased. Cogging torque is measured with an online procedure by scanning 360 degrees in the position feedback loop and measuring the required torque to stay in each position. This procedure generates a cogging-position map to be used in the feedforward algorithm. The reference [65] studied a similar approach in two ways; position based approach with a simpler controller (only high gain, no speed control), and acceleration based approach, good results are obtained. The reference [66] uses state-periodic adaptive compensation, illustrated through a simulation example for cogging compensation. For the friction

compensation, we have generated a velocity-friction map by commanding the motor at varying speeds, measuring and averaging the required torque to accomplish the desired speed. Identified disturbances are rejected with feedforward algorithms. With only cogging torque compensation, in speed control, 30-65% of the tracking error is removed in a feedback control system. Measurement and test results are presented. In addition to these internal disturbances, one should pay attention to the external ones. For example, if the motor is used in a helicopter platform, there will be low-frequency wind and platform disturbances and high-frequency propeller vibrations (at angular revolution frequency and its harmonics). For this reason, it is crucial to design a robust controller with output disturbance sensitivity function, suppressing low-frequency disturbances and not amplifying specific vibration frequencies coming from the platform. A common way to compensate for these external disturbances is robust controller synthesis [67, 68]. This study also touches upon the development of a controller design for a low-cost motor besides cogging and friction disturbance rejection. The following topics are discussed in this respect; FRF (frequency response function) measurement of a precise positioning system, controller design with "loop shaping" method according to system requirements, output disturbance sensitivity analysis.

The rest of the chapter is organized as follows: First, we give an overview of the test and measurement setup in Section 6.2. Then we cover the current and speed controller designs in Section 6.3. We also examine the controller implementation issues in an embedded world with their practical considerations. We describe and present the results of the cogging torque identification and compensation in Section 6.4. Then, we discuss and report the results of friction identification and compensation in Section 6.5. We elaborate on the importance of the work and suggest applications and extensions in Section 6.6.

6.2 Experimental Test Setup

Experiments have been performed on the test setup given in Fig. 6.1. For the motor driver card, the C2000 32-bit microcontroller of Texas Instruments is used. For measuring angular position, the rotary incremental magnetic encoder is used. The 1-bit

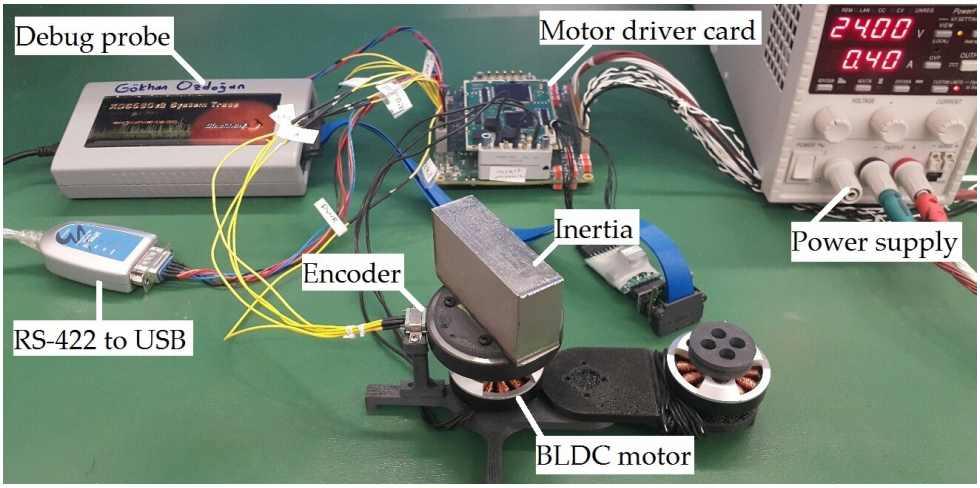

Figure 6.1: Experimental test setup.

resolution of the encoder is 34μRAD. The motor tested in this study is a BLDC motor, GBM3506-130T of iPower firm. The motor has 14 rotor permanent magnets (7 pole pairs) and 12 stator electromagnets (12N14P configuration). As of September 2018, the unit price of this motor is 18 USD, so the item can be considered as low-cost. 24 V power supply is used for the motor driver card. In order to simulate a useful payload (it may be tilt-mechanism for UAV, camera, or some other device), 400-gram pseudo weight is used. The rest of the mechanism is produced in a 3-D printer using sufficiently rigid material. Measurements are recorded at 2 kHz (position-rate control loop frequency) using the RS-422 communication protocol.

6.3 System Identification and Controller Design

6.3.1 Current Loop

First, we have verified the B-EMF waveform of the motor to be close to sinusoidal by driving it externally in constant speed using another motor linked with belt and measuring its line-to-line voltage by oscilloscope. We have preferred FOC method in current loop control which is most suitable to sinusoidal B-EMF waveform brushless motor. Ground-peak voltage level is measured to be 2.3 V and $V_{rms} = 2.3/\sqrt{2} = 1.62$ V in RMS. Number of pole pairs, N_p, is 7. The frequency of waveform is measured to be $F = 20.78$ Hz, which corresponds to $\omega = (F \times 2\pi)/N_p = (20.78 \times$

$2\pi)/7 = 18.6$ rad/s. Then, voltage B-EMF constant can be determined as $K_e = V_{rms}/(\omega\sqrt{3}) = 1.62/(18.6\sqrt{3}) = 0.05$ V/(rad/s). In SI base unit, from conversation of energy, motor torque constant is equal to 3 times voltage B-EMF constant (since it is 3 phase brushless motor), $K_t = 3K_e = 3 \times 0.05 = 0.15$ Nm/A. The definitions of these parameters may vary from producer to producer, but in this context, when $K_t = 0.15$ Nm/A, we expect 0.15 Nm torque to be produced from 1 A of quadrature current.

The PWM (pulse width modulation) frequency is 60 kHz, the current loop frequency is 20 kHz, and the speed-position control loop frequencies are selected as 2 kHz. In order to achieve high bandwidth speed loop control without amplifying noises too much, we aimed our current loop bandwidth to be 500 Hz. The resistance of motor is $R_m = 12.5$ ohm, and inductance is $L_m = 4.5$ mH. Quadrature (torque) and direct (flux) current loop controllers consist of a standard PI (proportional-integral) filter. PI parameters are selected such that $R_m/L_m = 2.7 \times 10^3$ rad/s pole of motor is canceled and satisfies 500 Hz current closed-loop bandwidth.

6.3.2 Speed and Position Loop

The motor rotation speed is estimated using an incremental encoder and linear Kalman filter with a constant acceleration model. State vector is sized 3×1. Covariance matrices of the process and measurement noise, R, Q, are determined using the results of [69]. In our system, encoder data is available in every cycle, therefore Kalman gain converges to a constant value. In order to consume the computation power of the microcontroller efficiently, we do not call Kalman update and predict functions, but use constant pre-calculated Kalman gain.

For an efficient robust controller, one requires an accurate FRF (frequency response function) measurement with its uncertainty for the dynamical system of interest. It is beneficial to increase the SNR (signal-to-noise ratio) in the frequency band of interest for the input excitation signal while satisfying constraints specific to the application such as the current limit. We have followed the results of [50] for open-loop nonparametric FRF measurement and its uncertainty. The system is excited with quadrature current command (A) and angular velocity (deg/s) is measured synchronously. The

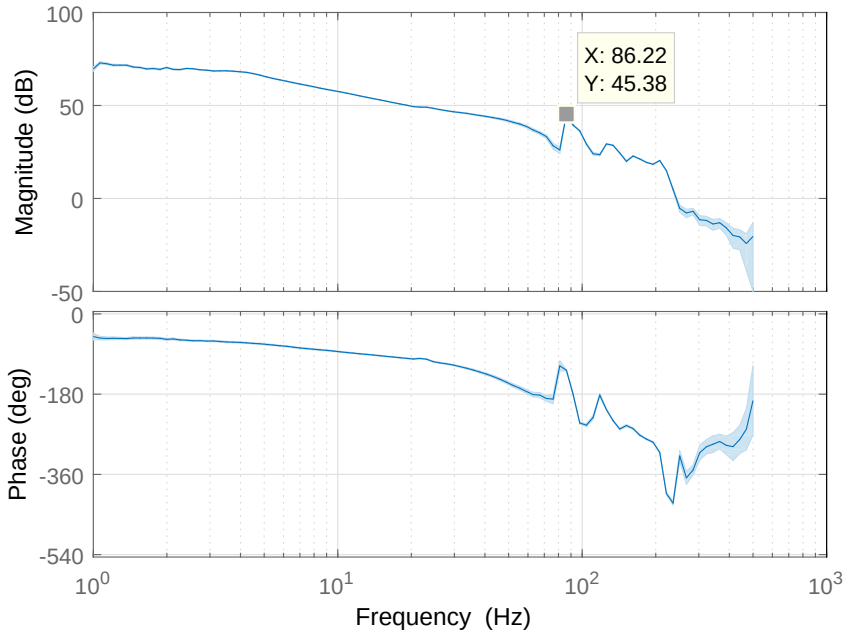

Figure 6.2: Open loop nonparametric FRF measurement Bode diagram.

excitation signal is a chirp that covers from 1 to 500 Hz logarithmically with 0.02 A amplitude. The mathematical model of the system is $\frac{1}{Js+B}$ where J is inertia and B is viscous friction coefficient. The FRF measurement is given in Fig. 6.2. Above the B/J rad/s, the friction loses its significance and the magnitude slope is -20 dB/dec, and the phase is -90 degrees as expected. Phase decreases more in higher frequencies due to time delay in the system. There also exists an antiresonance-resonance pair at 80 Hz and 86 Hz respectively due to the torsional stiffness of the system. 3σ uncertainty of the FRF measurement is given with light blue color in Fig. 6.2 which is greater in high frequencies. The unit of FRF measurement, (deg/s)/A is transformed to (rad/s)/Nm by multiplying $K_t^{-1}(\pi/180)$ and we fit the measurement into the mathematical model using MATLAB System Identification toolbox. Inertia is estimated to be $J = 1.5 \times 10^{-4}$ kg·m^2.

The control system structure is given in Fig. 6.3. Based on this figure, some notions

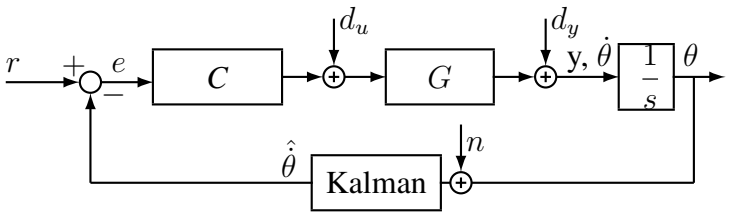

Figure 6.3: Control system structure.

will be given to explain properties of the control system.

$$L = G(s) \cdot C(s) \tag{6.1}$$

$$S = (1 + L)^{-1} \tag{6.2}$$

$$T = L \cdot (1 + L)^{-1} \tag{6.3}$$

where S is the transfer function from d_y to output y or from reference r to error e. T is the complementary sensitivity function of r to y or n to y. L is the open loop transfer function from error e to output y. Then linear control system design have some trade-offs as follows;

- L should not be greater than the value which satisfy nominal and robust stability.
- We desire sensitivity function to be $S \to 0$ on frequencies where output disturbance exists.
- We desire high bandwidth closed loop for good reference tracking, $T \to 1$.
- Sensor noise effect on output should be minimized, $T \to 0$.
- Controller should be strictly proper, $\lim_{\omega \to \infty} C = 0$.
- We also have $S + T = 1$ constraint.

In order to meet these conflicting requirements, we target the open-loop shape given in Fig. 6.4.

The controller designed according to requirements consists of the followings; 2 PI filters (with anti-windup implementation) to satisfy -40 dB/dec slope target shape

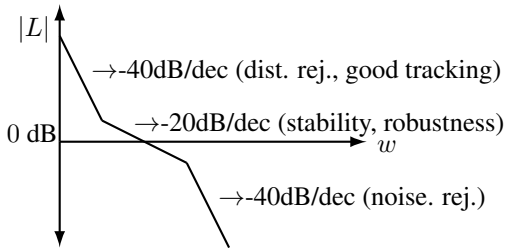

Figure 6.4: Desired loop shape.

which will allow high disturbance rejection in low frequencies, 1 lead filter with a critical frequency lying on crossover frequency of open-loop gain to increase phase margin, 1 low pass filter to reduce noise effects and be robust to unmodeled dynamics, and 1 notch filter at 86 Hz to dampen torsional resonance of the system. For an aggressive controller, we could have aimed 5-6 dB and 30-45 degrees for the gain and phase margins, but we have set them 12 dB and 75 degrees for even higher robustness. For digital filter implementation, we used tustin transform with pre-warp. High-order filters suffer coefficient sensitivity problems due to the limited number of bits that represent the coefficients. Small errors in the coefficients cause large errors in the locations of the poles and zeros of the filter. Therefore, high-order filters are decomposed in series into 1st and 2nd order filters to reduce the errors in realizing digital controller. Open-loop transfer function, L, is given in Fig. 6.5. L is a minimum phase system with 2 phase crossover frequency at 1.5 and 48.9 Hz. When the nyquist diagram is analyzed, we observed that the gain margin should be calculated from 48.9 Hz which is 14.5 dB, and the phase margin is 73.8 degrees at 9.3 Hz.

Output disturbance sensitivity function, S is given in Fig. 6.6. According to S, an output disturbance at 1 Hz attenuates into 0.038 of its magnitude. Disturbances up to 14.5 Hz are rejected, 14.5-70 Hz range is amplified by 1-1.24 in magnitude, and above 70 Hz controller will have a minor effect on output disturbance.

After designing a satisfactory rate loop, the position loop is trivial. Position loop controller contains a single proportional gain, outside the rate loop (a cascaded control structure). There exists no steady-state error in the position loop owing to integral action in the rate loop.

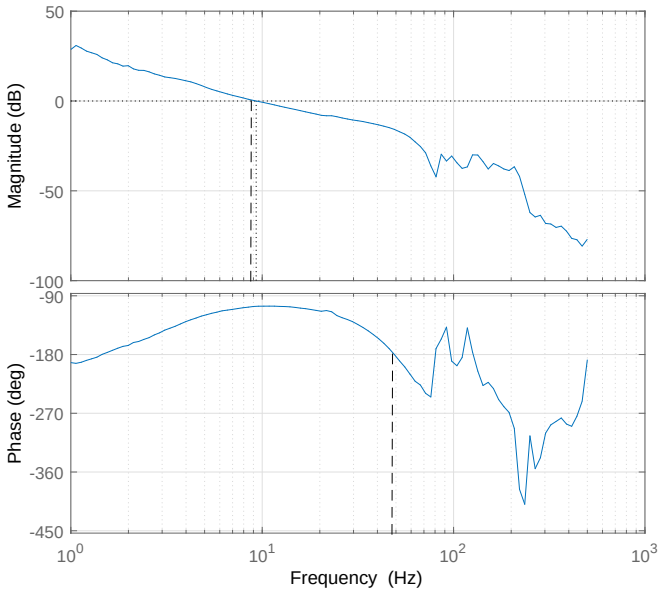

Figure 6.5: Bode Diagram of open loop system, GM = 14.5 dB (at 48.9 Hz), PM = 73.8 deg (at 9.3 Hz).

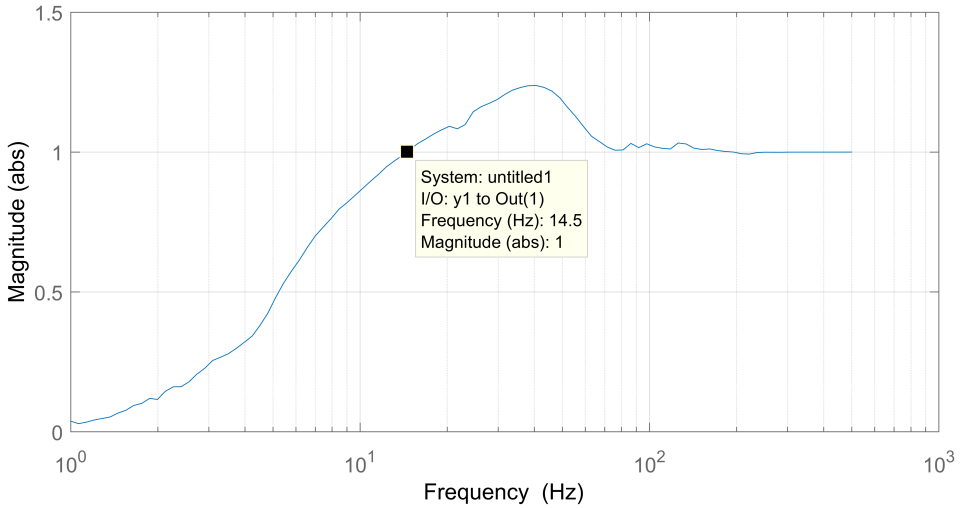

Figure 6.6: Output disturbance sensitivity function.

6.4 Identification and Rejection of Cogging Torque

We identify cogging torque with an online procedure by scanning 360 degrees in both directions and measuring the required average torque to stay in each position. This

procedure generates a cogging-position map to be used in the feedforward algorithm. We have the following assumptions for cogging identification algorithm;

- There exist no steady-state error in the position control loop.
- Quadrature current and produced motor torque have a linear relationship by motor torque constant, $T_{mtr} = K_t \times I_{q,cmd}$.
- Current related torque ripples are minimized by applying optimal current waveform taking into account motor structure. In this system, FOC is used since the B-EMF waveform of the motor is sinusoidal.

The positioning system is commanded to scan 360 degrees with 1 degrees increments, waiting 4 seconds in each reference. First, 2 seconds are omitted to remove the transient effects. The controller output, quadrature current command in the last 2 seconds is averaged and saved in a look-up table. System settles to each commanded position with 0 steady-state error and 0.02 degrees peak-to-peak small oscillations. Although the cogging torque is the dominant disturbance source, friction and unbalance are also present. This procedure is realized in both forward and backward directions. Generated position-cogging maps are given in Fig. 6.7 and 6.8. There exist an offset between forward and backward measurements resulting from static friction. As it can be seen, cogging torque map is mainly shaped by the motor structure of 14 rotor permanent magnets and 12 stator electromagnets.

The cogging-position map is stored in RAM with a 360×1 sized 16-bit resolution vector where its index corresponds to the position in degrees. Intermediate values are estimated using linear interpolation. A cogging-position map has a periodic characteristic, hence, instead of storing the map in a look-up table, it is also reasonable to use an FFT (fast fourier transform) curve fit with 6-8 coefficients and calculate intermediate values. FFT curve fit would reduce RAM usage at the expense of slightly increased computation time and intermediate value estimation error.

In the rate loop control, we feedforward the negative of estimated cogging torque to the motor torque command and reduce the effect of cogging disturbance. Several tests have been performed, one of the test scenarios is as follows; 1 deg/s rate command is applied for 360 seconds. The integral of the error signal (difference between rate

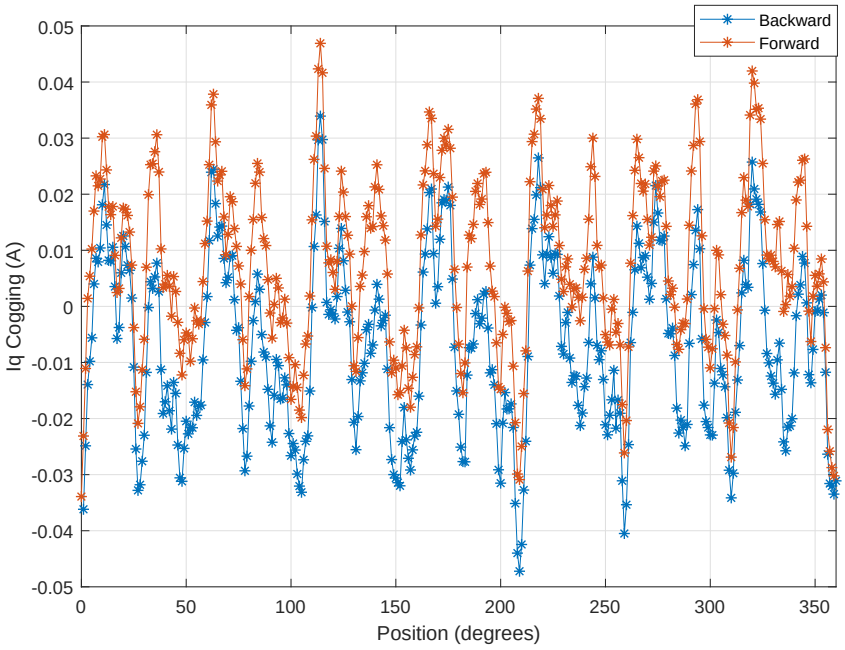

Figure 6.7: Cogging Torque Position Map, Left, cartesian plot, blue: backward, red: forward measurement.

command and rate feedback) is computed and displayed in Fig. 6.9 which shows that 55% improvement is obtained with anti-cogging. Rate feedback controller and test conditions are the same except that the anti-cogging algorithm is enabled in one (blue line) and disabled in the other (orange line). In sinusoidal and constant rate command with various amplitudes test scenarios, 30-65% improvements are obtained.

6.5 Identification and Rejection of Friction Torque

In this study, we estimate the steady-state static friction parameters based on the data collected from rate loop constant velocity measurements. Dynamic friction parameter identification topic is left as a future study. The assumptions presented in cogging identification procedure are also required for friction identification. In the rate loop, the rate reference is increased from 0.015 deg/s to 57 deg/s logarithmically in 15 steps, waiting 4 seconds in each reference. First, 2 seconds are omitted to remove the transient effects. The quadrature current command in the remaining 2 seconds is multiplied by K_t, averaged, and saved. Measurements are realized in both directions.

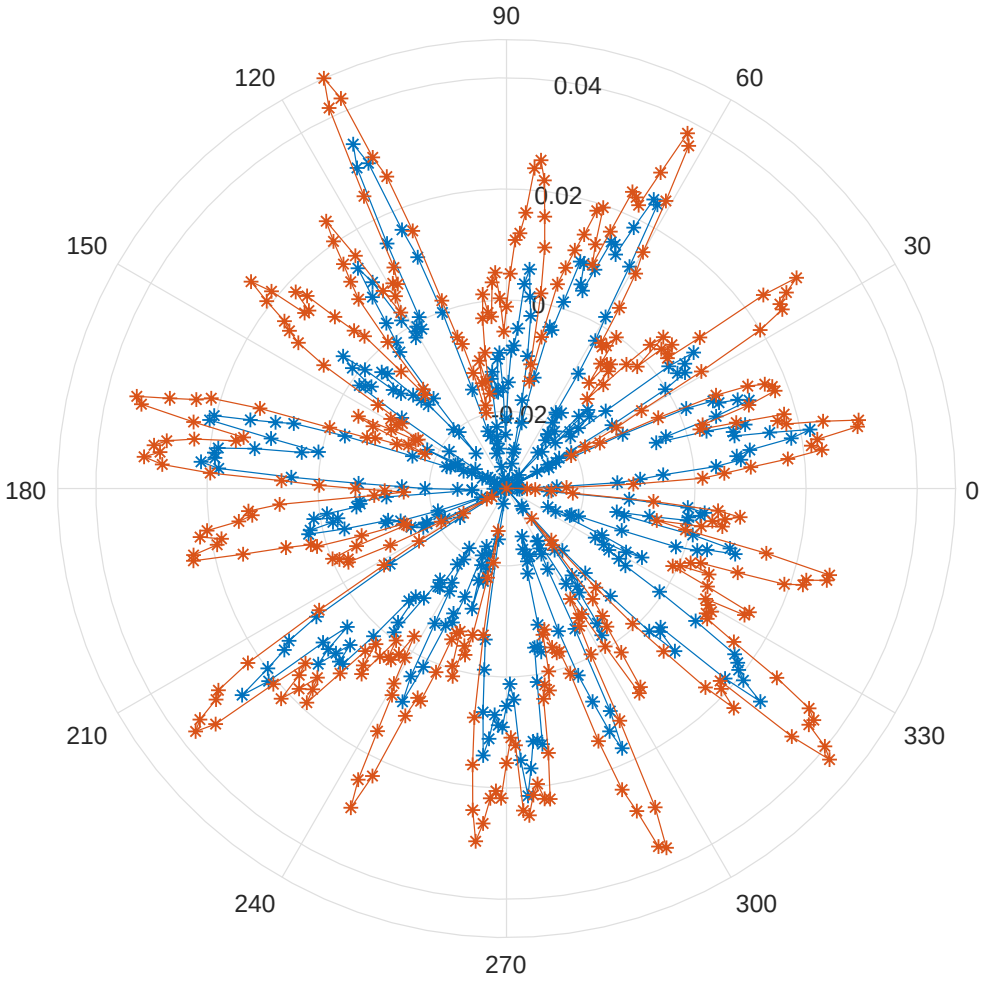

Figure 6.8: Cogging Torque Position Map, Polar plot, blue: backward, red: forward measurement.

Steady-state angular velocity - friction map is given in Fig. 6.10.

In literature, there exist numerous friction models. Discontinuous models perform poorly for the high performance requiring applications. We preferred the continuously differentiable model given in (6.4) with 6 parameters to describe the friction behavior of the brushless motor. Here, ω is the steady-state angular velocity, and T_f is the corresponding friction torque.

$$T_f = (T_c + (T_s - T_c)e^{-|\omega/\omega_s|^\delta}\text{sign}(\omega) + (\sigma_2\omega) + T_g \tag{6.4}$$

These coefficients are estimated using grey-box nonlinear modeling functions of MATLAB. Parameter definitions and their estimated values are given in Table 6.1. Static

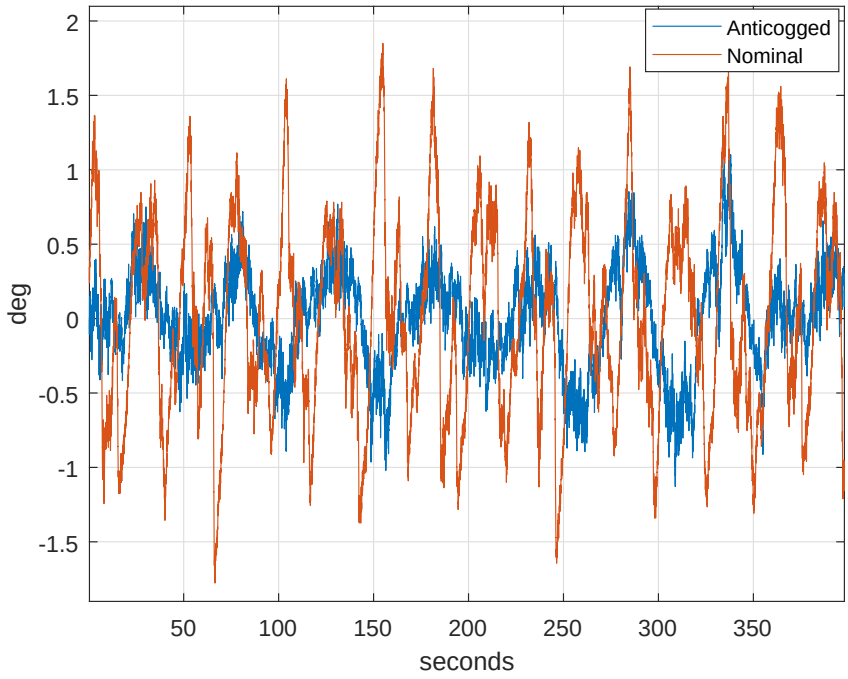

Figure 6.9: Anticogging performance test, tracking error when rate command is -1 deg/s.

friction model parameters given in (6.4) are estimated from measurements in 13 iterations with 98.4% fit. The cost function used in estimation is given in (6.5).

$$\underbrace{\min}_{\sigma_2, \omega_s, T_s, T_c, T_g} \sum_{i=1}^{n} [T_{fss}(\omega_i) - \hat{T}_{fss}(\omega_i)]^2 \tag{6.5}$$

In the rate loop control, the feedforward of the negative of estimated friction torque corresponding to the angular velocity reference command will reduce the effects of friction disturbance. Successful application highly depends on the quality of estimated parameters and the model used. The feedforward friction compensation has been shown to be successful in gyro-stabilized gimbal systems by [70] and in telescope applications by [71]. In our tracking and velocity tests, friction compensation improved the controller performance slightly, no more than 5%. This enhancement is not as significant as the anti-cogging improvement of 30-65%. There may be several reasons for this situation. The first reason is that the dominant disturbance in this system is cogging torque with its 0.007 Nm peak ripples, and friction torque is around 0.002 Nm level. Another reason is that the model does not cover the dynamic prop-

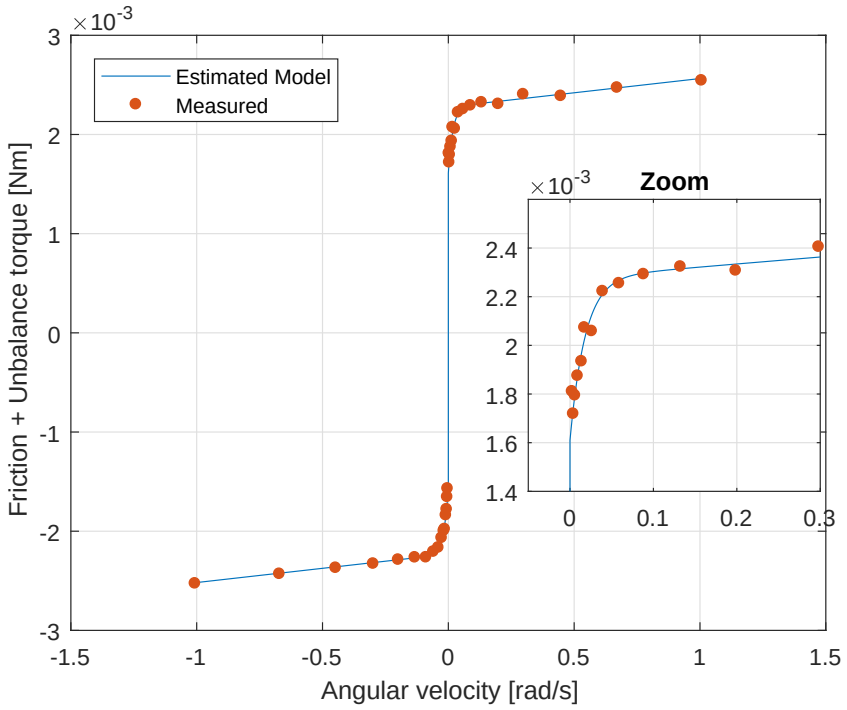

Figure 6.10: Friction-velocity map and estimated static friction model, 98% fit.

Table 6.1: Static friction parameters.

Definition	***Symbol***	***Value***	***Unit***	***Freedom***	***Range***
Input signal	ω	-	rad/s	-	-
Output signal	T_f	-	Nm	-	-
Viscous coefficient	σ_2	2.9×10^{-4}	Nm.s/rad	(est)	[0,∞]
Stribeck velocity	ω_s	1.8×10^{-2}	rad/s	(est)	[0,∞]
Static friction	T_s	1.6×10^{-3}	Nm	(est)	[0,∞]
Coulomb friction	T_c	2.3×10^{-3}	Nm	(est)	[0,∞]
Stribeck factor	δ	1	-	(fix)	[0,∞]
Bias torque	T_g	2.3×10^{-5}	Nm	(est)	[$-\infty$,∞]

erties of friction. For the same velocity, the friction torque in the accelerating profile is greater than the friction torque in decelerating profile. This hysteresis is called friction lag or friction memory. We predict that using the LuGre friction model will improve the results since it captures this kind of dynamic friction properties. LuGre friction model contains σ_0 bristle stiffness, σ_1 bristle micro damping parameters and

z internal friction state in addition to parameters given in (6.4), [72].

6.6 Conclusion

In many robotic applications, size and weight limitations are put together with high-density torque and high-performance control requirements. This study is concerned with the accurate identification of cogging and friction torque, and their compensation using model-based feedforward techniques. The position sensor is used for identification which already exists in precise positioning systems, so the cost of the system is not increased. Cogging torque can also be decreased by changing motor structure, but the manufacturing cost increases, and produced torque in the same size decreases dramatically. With only cogging torque compensation, in speed control, 30-65% of the tracking error is removed in a feedback control system. Friction compensation did not perform as well as cogging compensation, reasons are discussed in Section 6.5. In systems where friction disturbance is the dominant disturbance source, friction compensation would be more beneficial. Nevertheless, explicit identification of friction is always valuable information for controller design.

The controller design procedure using loop shaping, cogging, and friction disturbance rejection algorithm depicted in this study is applicable not only to cheap brushless motors that are used in tilt-mechanisms but also to all servo motors requiring high performance but suffer from aforementioned disturbances. For example, in an inertially stabilized gimbal system that uses gyro feedback, we can reject cogging torque and increase stabilization performance using a relative position sensor.

CHAPTER 7

EXPERIMENTAL TESTS

This chapter starts with Section 7.1 which gives a brief description of the hardware and software of a newly built experimental test prototype. Section 7.2 presents the experimental test results and discusses flight performance, proving the HLAV concept by demonstration in the outdoor environment. The feasibility and performance of the system are verified.

7.1 Prototype Hardware

In this section, we will briefly present the hardware and software used in developing the prototype. While designing an air vehicle, the parameters of the sub-parts such as the motor, motor driver card, propeller and battery cannot be chosen with infinite freedom. The system designer usually has limited options for various components and makes a choice between them using their data-sheets. In the system design, besides the flight efficiency, the motor time constant parameters that affect the agility of the system and the prices of the components are also important parameters that affect the selection. In [73], a mixed-integer programming approach is used for multicopter design optimization from available components.

Various types of prototypes were developed over the lifetime of the HLAV project, and a few unfortunate crash accidents occurred during the development phase which is quite a common phenomenon in projects like this. The hardware presented in this section is one of the intended prototype designs among many of them. There may be reasonable differences from the prototype that we conducted the flight field tests, especially the parameters of the motors and propellers since we replaced some parts

Figure 7.1: Pixhawk 2

with what we have in similar from the lab. For the system design introduced in this section, payload capacity is 4.05 kg and flight time can be 18 minutes at hover in theory. The total system weight is expected to be 7.29 kg, with a payload it is 11.34 kg. Hover current consumption is 52.2A and max current consumption is 247.6A which are both below battery constant discharge rate and peak discharge rate of the battery. Airframe (vehicle body) is custom designed using aluminum material.

This prototype is used for the proof of concept of controllability. As this prototype is scaled to larger dimensions, a more effective system will emerge for heavy lifting. For future study, it is planned to work on a larger HLAV system, where internal combustion engine propulsion alternatives will be evaluated.

Flight controller. There exist many different autopilot boards, open hardware or closed hardware. Open-source hardware and software projects are revolutionizing Unmanned Aerial Vehicles (UAVs) technology, and advancements in avionics have significantly reduced the cost of aerial robotics. In this project, we preferred Pixhawk as autopilot hardware. Pixhawk is an open hardware project that aims to provide the high-end autopilot for academics, hobbyists and commercial use in industry (See Fig. 7.1). It is one of the most popular Linux Foundation DroneCode projects. PixHawk is armed with an advanced 32 bit ARM processor, 32-bit failsafe co-processor, support multiple flight stacks: PX4 and APM, micro SD card for logging, necessary sensors with sensor redundancy for safety, and plenty of interface capabilities.

Autopilot software. PX4 and ArduPilot are two open-source, unmanned vehicle autopilot software packages supported by strong communities. In this study, we worked

with PX4 which is freely available to anyone under a BSD (Berkeley Software Distribution) license. PX4 allows the user to make the necessary changes and developments which is necessary for advanced research projects for special requirements. Another specification that makes PX4 attractive is the way it could communicate with Robot Operating System (ROS) which is an open source robotics middleware suite consisting of frameworks of tools, libraries, and many robotic algorithms to aid in robot software development. ROS can be used with PX4 and the Gazebo simulator. It is also possible for MATLAB to communicate with a ROS network. From the Simulink model, C++ code generation for a standalone ROS application is realizable. Recommended PX4 development platform is Ubuntu Linux. The software development programming language is C/C++ and it is possible to build code with or without using an integrated development environment (IDE). QGroundControl program that is installed in ground-control-station (laptop or tablet) provides vehicle setup, full flight control, mission planning utilities, and it is compatible with PX4.

Motor, propeller, and ESCs. To achieve the aim of a heavy payload, the key component, besides the flight controller, is the brushless motor. To the best of our knowledge, the most powerful motors are supplied by KDEDirect and T-Motor companies. T-Motor U Pro Series motors are well suited to heavy lifting applications. Larger diameter, slower turning propellers are generally much more efficient than smaller, faster turning propellers. However, oversized propellers will cause overheating of the motor and reduce the control bandwidth. T-Motor company shares extensive test reports and makes recommendations for optimum performance motor propeller matches according to requirements. Big slow propellers can also induce vibration which will increase gyro and accelerometer noises, decreasing stability and navigation performance. They also have response rate issues (low bandwidth). Propellers exist in different materials, weight, rigidity, length, and pitch. The number of blades is usually 2 or 3. The propellers should be chosen based on the description of the motors and performance of them for the applied battery and overall lift power we expected from each motor according to our design. Propeller noise should also be taken into account in the design as it affects sensors, aircraft frame and causes pollution over residential areas. Ducts are useful for enhancing the efficiency of thrust, protecting the blade, and ensuring personal safety. But we did not prefer them in our

Table 7.1: Propulsion system

Description	***Big rotors***	***Small rotors***
Brushless Motor	U13 KV85, T-Motor	U5 KV400, T-Motor
Weight including cables (kg)	1.280	0.195
Rated Voltage	6-12S Lipo	3-8S Lipo
ESC		
Weight (kg)	0.110	0.055
Throttle response speed (s)	0.3	0.12
Propeller	G32×11	G16×5.4
Weight (kg)	0.129	0.028
Optimum RPM	1200-3000	4000-6000
Budget $ (2 motor, 2 ESCs, prop pair)	1286	407
Thrust at 50% throttle (kg)	4.4	1.2
Thrust at 100% throttle (kg)	14.6	2.85
Efficiency at 50% throttle (kg)	10.71	10.4

design since they do not fit large sizes.

ESCs (Electronic Speed Control) are also very important. ESCs must be properly selected so that they can provide the current and power required. Especially for "Heavy Lift" applications, cooling is very important and ESCs may need to be placed in areas with high airflow. When choosing ESCs, a safety margin should be left to the maximum current to efficiently avoid burnout of the power tube.

While selecting the propulsion system, we aimed G/W (gram/watt) efficiency to be above 10 at 50% throttle. We also target our copter design to hover at around 50% throttle for optimum efficiency and reasonable flight time. According to those considerations, we have many options, but for now, we choose the following components given in Table 7.1. More information is given on the T-Motor website.

In order to fully understand the performance of propulsion system components (ESC, motor, propeller, battery), we have performed several tests and measured the thrust, rotation speed, current, and voltage, calculating vital metrics like power, motor ef-

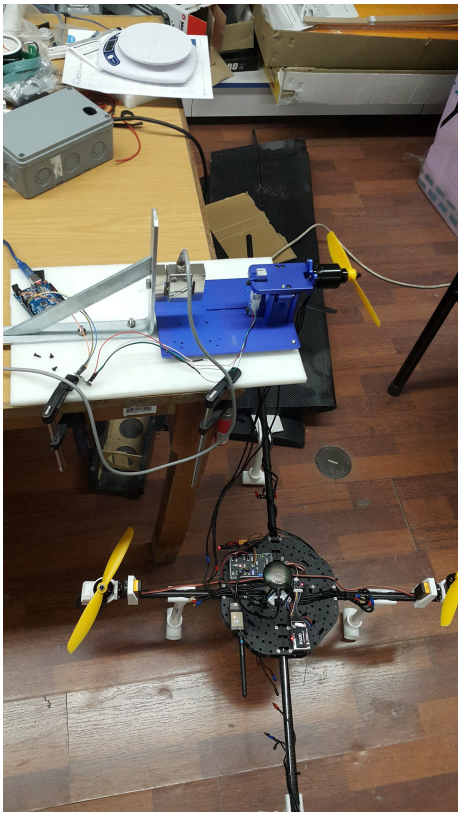

(a) Small Rotor

(b) Big rotor.

Figure 7.2: Thrust tests and parameter identification

ficiency, and propeller efficiency. The measurement test setup is given in Fig. 7.2a, 7.2b.

Servo motor and its mechanism. In order to tilt small rotors, we need a servo mechanism and servo motor. We developed our own custom design mechanism in CAD and print it in a 3-D printer which is given in Fig. 7.3. It is able to be installed on any 16mm tail boom size and suitable for any round carbon fiber or fiberglass frame.

Servo motor is a very important part of the system, and it should be as reliable as possible. One of the reliable servo motor producers is Dynamixel firm. Their products need serial TTL communication to be operated which needs a bit more study to hack PX4 software. We preferred a servo motor that can communicate using PWM protocol. FEETECH is a new firm but is producing quality motors. We chose the

Figure 7.3: Tilt-rotor servo motor mechanism from different perspectives

Figure 7.4: Servo Motor

Table 7.2: Servo motor, FT5313M

Description	***Specification***
Operating temperature	-15° / +70°
Weight	60g
Budget	46$
Stall torque (4.8V)	12.5 kg·cm
Speed	0.13s / 60°
Stall current	1.5A
Pulse width range	900-2100μsec
Running degree	120°

FT5313M digital servo motor which has metal gear, important for reliability. The specifications are given in Table 7.2.

The mechanism and servo motor described in this section were used in the design of this prototype. But in future studies, when a more efficient and larger system is to be designed, instead of choosing off-the-shelf servo motors, we aim to use our

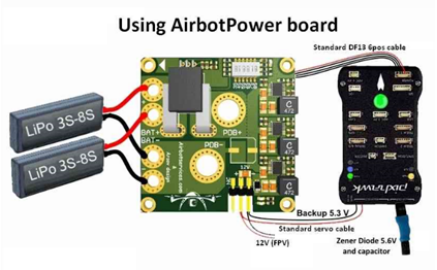

Figure 7.5: Power board

own design with the PMSM torque motor and disturbance compensation techniques suggested in Chapter 6.

Batteries. Lithium Polymer (LiPo) batteries are currently the preferred power sources for most lightweight, high-current, high-capacity power storage. They offer a high energy-storage/weight ratio and high discharge rate. To achieve the aim of a 10-20 minute flight time under full payload, battery specifications will be selected accordingly. "Multistar High Capacity 16000mAh 6S 10C Multi-Rotor Lipo Pack XT90" battery is the current choice of the system. It weighs 2.05 kg and the price is about 150 USD. The battery constant discharge rate is 160A and the peak discharge rate is 320A.

In our system, big and small motors do have different rated voltages (3-8S for small and 6-12S for big ones). Therefore we may only prefer 6-8S batteries. Providing different batteries for different motors may cause extra weight and furthermore, pixhawk can only measure one battery voltage and current status to warn the user about low battery.

We will also need to power 1 or 2 servo motors, pixhawk, and other possible UAV components. Therefore, we need a reliable and efficient power board or several SBECs (switching battery eliminator circuitry) to provide lower voltages (~5V). AirbotPower board is one option for that (see Fig. 7.5). It provides two 5.3V and one 12V (up to 3.5A each) with ~91% efficiency. It provides current and voltage measurements through the main power port, up to 150A and 8S. Servo motor and pixhawk both require 5V, but we should not power them using the same source as the voltage spikes due to servo motor control may cause pixhawk to reset and lose UAV.

Communications. We need to transmit commands from the remote pilot to the corresponding receiver, then the receiver passes the commands to the autopilot after decoding them, finally, the HLAV flies according to the commands. The most common choice is to use RF (radio frequency) which includes 72 MHz and 2.4 GHz. 2.4 GHz is more popular. In this project, we have used 3DR telemetry and FrSky 2.4GHz TARANIS Radio System transmitter, receiver.

As a communication protocol, MAVLink (Micro Air Vehicle Link) is an attractive option due to its lightweight message structure. Another appealing option for controlling the drone is to use the cellular network (4G) which will increase the communication bandwidth dramatically and the range will be anywhere on earth where a 4G cellular network is supported. Using a 4G network connection seems to eliminate the problem of distance restriction RF communication suffers. This could be a huge advantage in some of the more critical missions, like patrolling and search & rescue.

GNSS. For the GNSS module, we have used 3DR UBlox GPS + Compass Module. This module allows the GPS to be mounted separately from the flight control for a clear view of the sky and allows the compass to be placed away from interfering magnetic fields coming from motor cables.

Supplementary components. In order to improve the navigational positioning of the drone, GPS-Vision-based solutions can be tried. With vision capability, the drone will be able to land on a landing pad autonomously and will be able to accomplish vision-based tasks. For image processing, we need a low-cost lightweight single board computer. "ODROID-XU4" which is a community-supported development platform is well suited for this purpose. As for the camera, USB WebCam "Logitech C920" can be used. For further abilities and safety, an ultrasonic range finder can be used for obstacle avoidance.

7.2 Experimental Test and Flight Results

In order to verify the feasibility of the proposed design, the HLAV configuration which consists of two large propellers and two small tilting propellers has been built (See Fig. 7.6). This prototype is used for the proof of concept of controllability.

Before working on a bigger prototype introduced in the previous Section 7.1, we needed a medium-sized prototype to test our software and safely check algorithms. As this prototype scales up to larger sizes, a more effective system for heavy lifting will emerge. We have 330Kv (Kv: RPM/V, motor velocity constant) motors and 17-inches propellers in the bigger propulsion system. The smaller propulsion system has 830Kv motors and 9-inches propellers. Servo motors in tilt mechanisms have a torque capacity of 10.3 kg-cm. The tilt mechanism is produced in a 3D printer with strong material.

Control allocation algorithms are realized in PX4 open-source flight control software. The field test is performed using position flight mode. In this mode, when the remote control sticks (roll, pitch, and throttle) are released, i.e. centered, the aerial vehicle keeps the 3-D x, y, z position steady against any disturbance like wind and other forces. When the sticks are outside of the center, roll, pitch, and throttle sticks set translational velocity commands in x, y, and z directions respectively. Yaw stick sets the angular rate command, ψ, in the horizontal plane.

The cascaded control loop structure consists of a translational position loop, translational velocity loop, angular position loop, and angular rate loop. From position control, desired roll and pitch angles (ϕ_d, θ_d) are produced. Attitude control stabilizes the vehicle and executes the desired angle commands. In the control allocation block, desired thrust and torque commands are mapped to rotor/servo parameters. Equilibrium point, $u_0 = \left(\omega_{1,0}^2\ \omega_{2,0}^2\ \omega_{3,0}^2\ \omega_{4,0}^2\ \xi_{1,0}\ \xi_{2,0}\right)^T$, is selected such that, in hover, big rotors carry the 0.9 of total mass and small rotors carry the 0.1 of the total mass. Before the flight, the following parameters are calibrated for safety and performance.

- Gyro and accelerometer bias, alignment
- Magnetometer calibration
- Motor driver PWM input range calibration
- Radio offset calibration
- Current and voltage sensor
- Battery capacity and internal resistance measurement

Figure 7.6: The system used in field flight tests. A video showcasing is accompanied: `https://youtu.be/yRUwUlp7Ucc`.

The aerial vehicle performed hover, and execute velocity commands in a stable manner. The trajectory that is followed can be seen in Fig. 7.7. A video showcasing is accompanied: `https://youtu.be/yRUwUlp7Ucc`. Translational position loop performance are shown in Fig. 7.8, 7.9, 7.10. The position loop is active only when remote control sticks are centered, that is why the reference command in blue color is piecewise. Fig. 7.11, 7.12 and 7.13 show that the HLAV system successfully executes the joystick translational velocity commands. Euler angles attitude tracking control loops are given in Fig. 7.14, 7.15, 7.16 and angular rate loop results are given in Fig. 7.17, 7.18, 7.19. The BLDC motor control commands for rotors are given in Fig 7.20, and tilt-mechanism tilt angle control commands for servo motors are given in Fig 7.21. Power consumption results are presented in Fig 7.22, 7.23. Finally, in Fig 7.24, PSD (Power Spectral Density) estimate of linear vibrations on the vehicle are given. Monitoring, analyzing, and reducing linear vibrations are important requirements in aircraft design since vibrations are one of the most important parameters that determine control stability and navigation performance.

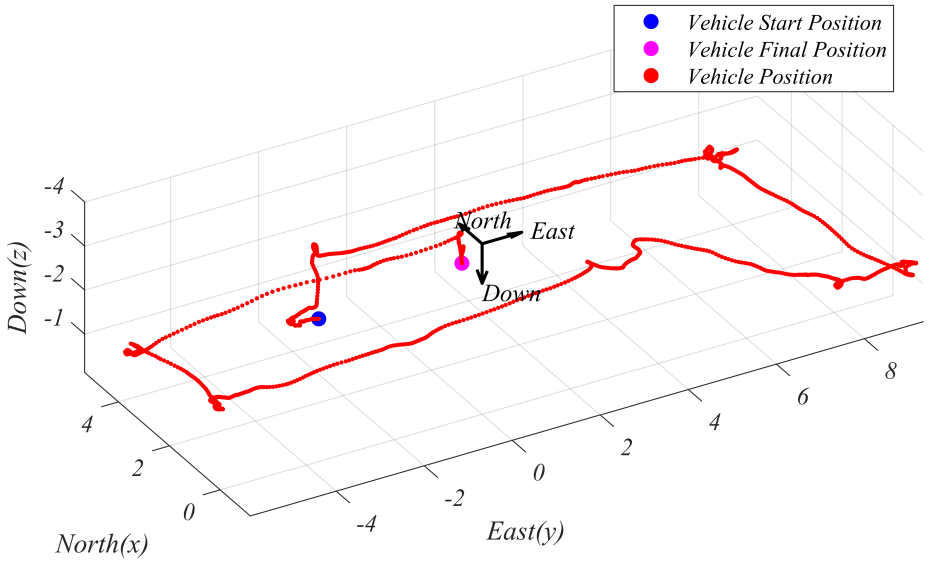

Figure 7.7: Vehicle trajectory in NED frame (meters)

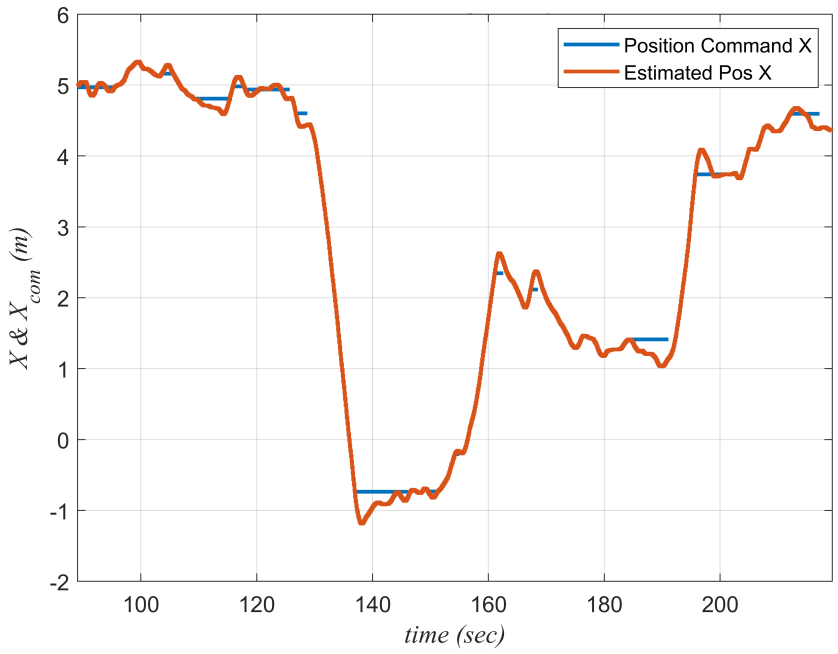

Figure 7.8: Position tracking in NED frame, x

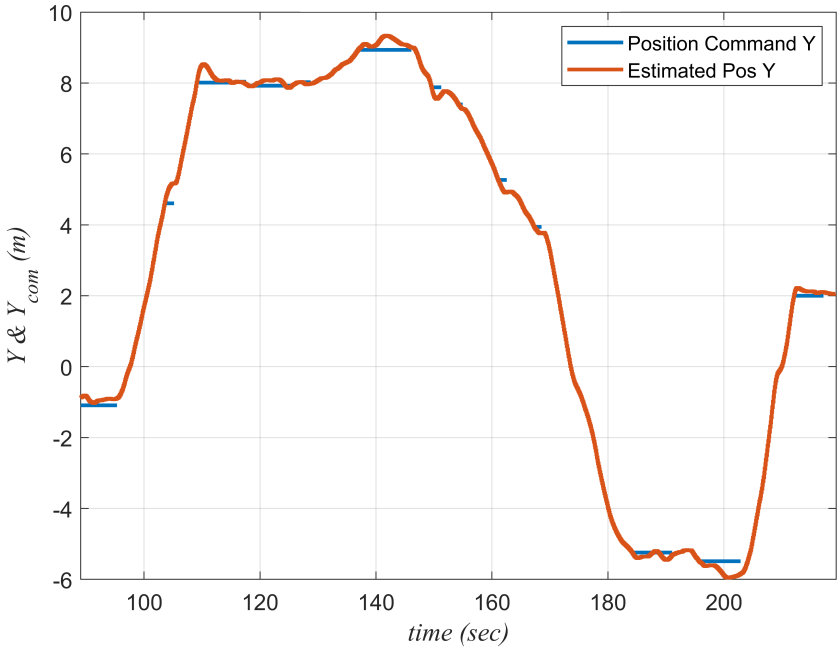

Figure 7.9: Position tracking in NED frame, y

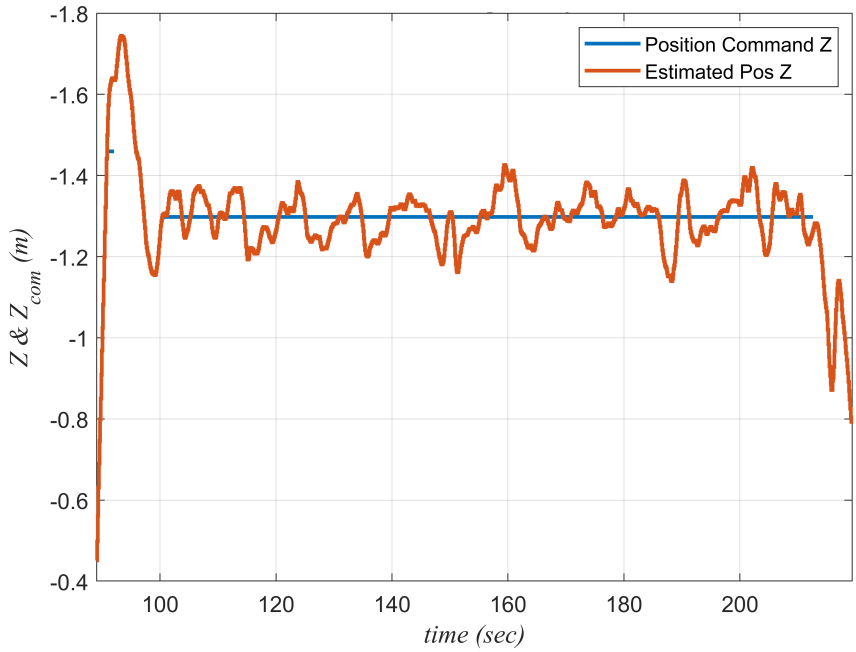

Figure 7.10: Position tracking in NED frame, z

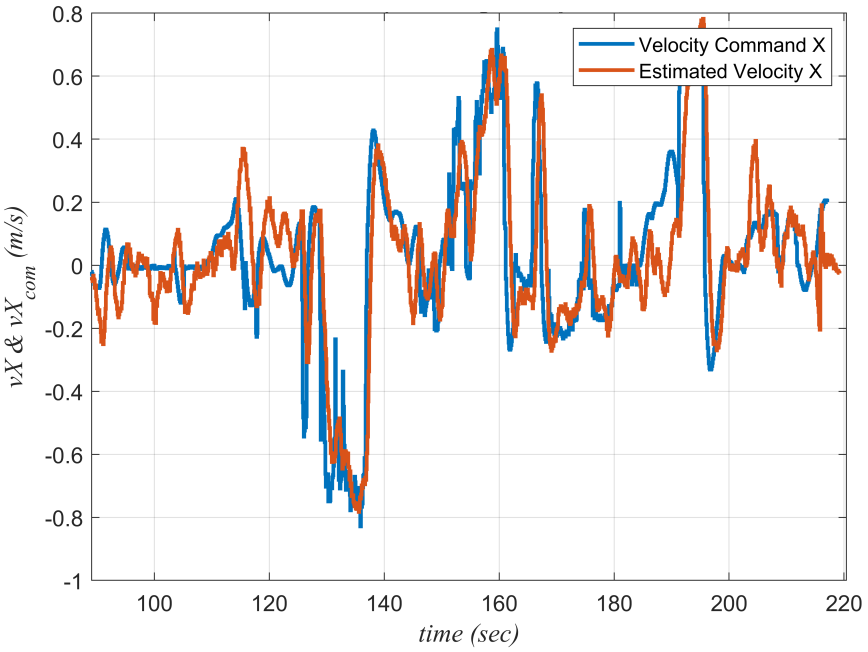

Figure 7.11: Translational velocity tracking, V_x^N

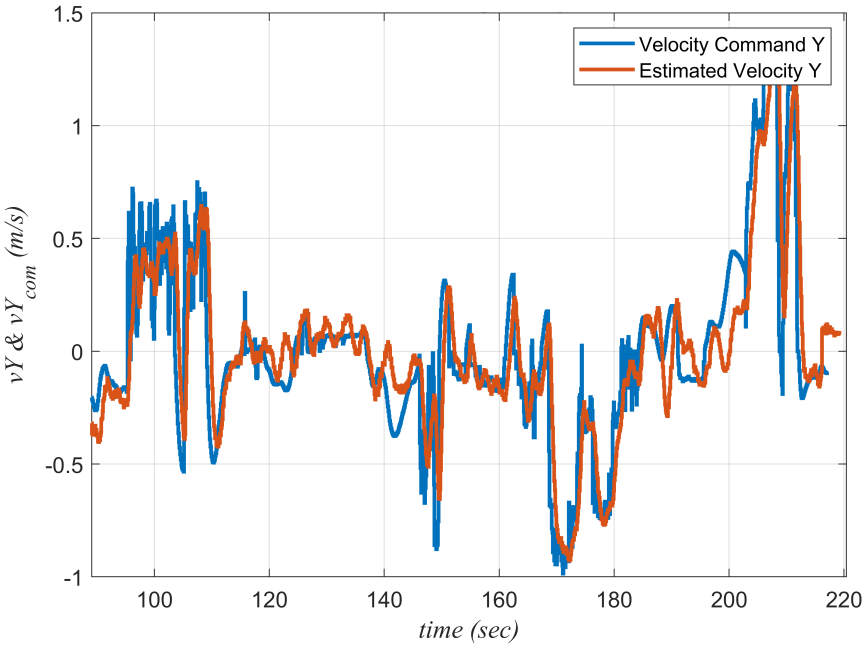

Figure 7.12: Translational velocity tracking, V_y^N

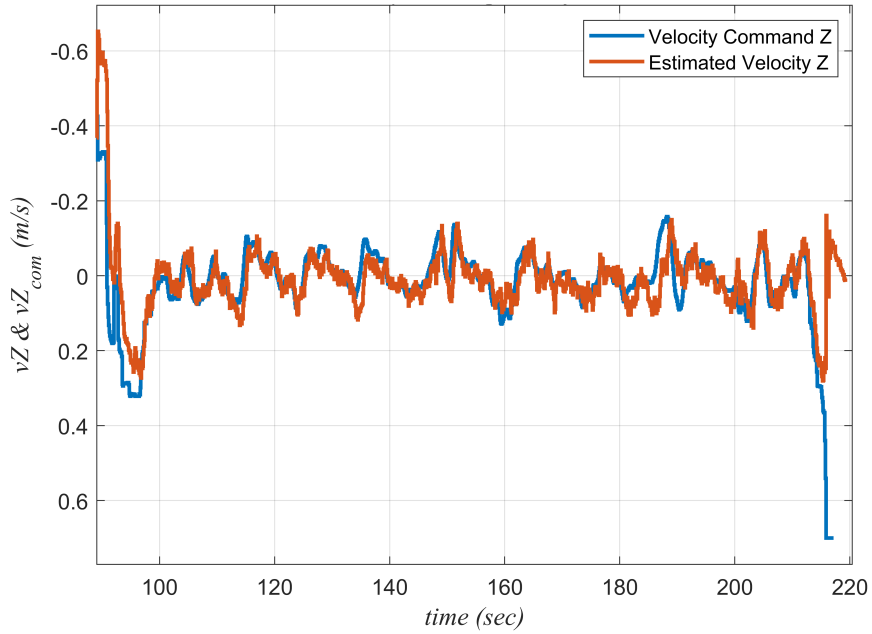

Figure 7.13: Translational velocity tracking, V_z^N

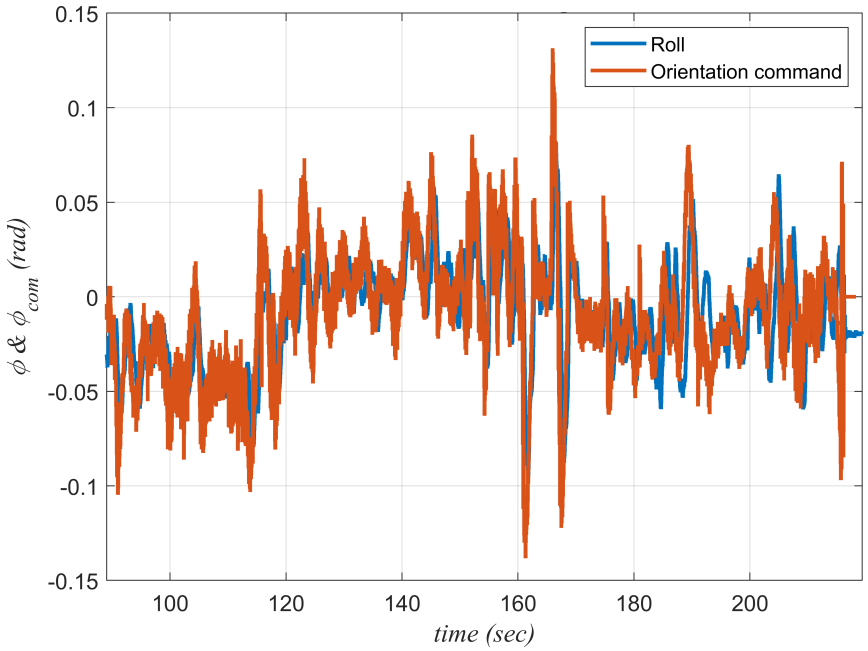

Figure 7.14: Attitude tracking, Roll, ϕ

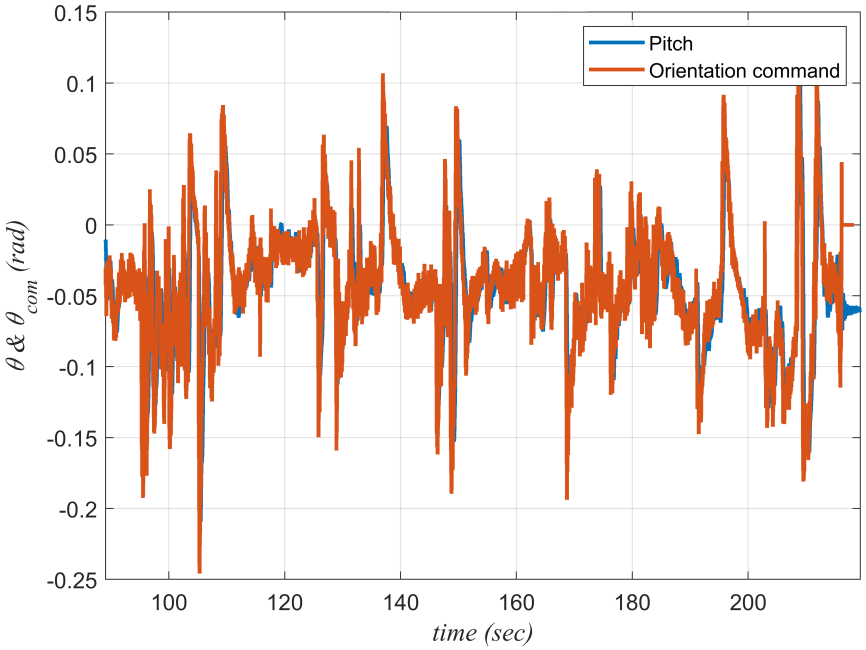

Figure 7.15: Attitude tracking, Pitch, θ

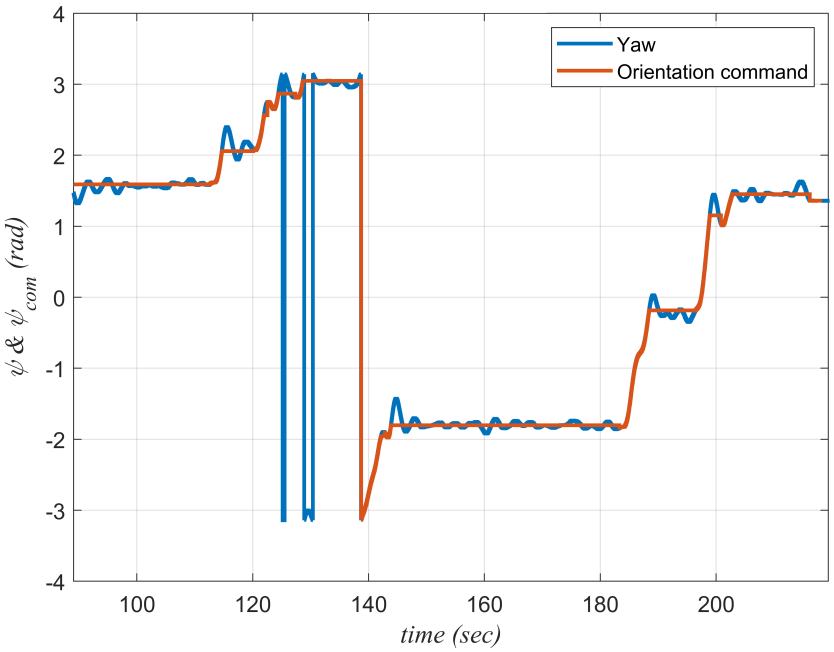

Figure 7.16: Attitude tracking, Yaw, ψ

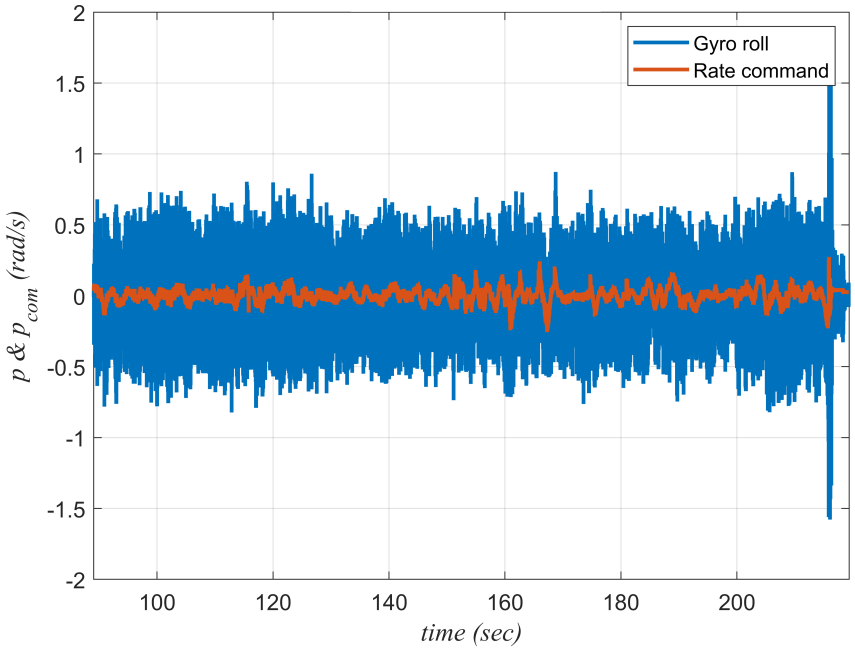

Figure 7.17: Angular rate tracking, Roll, p

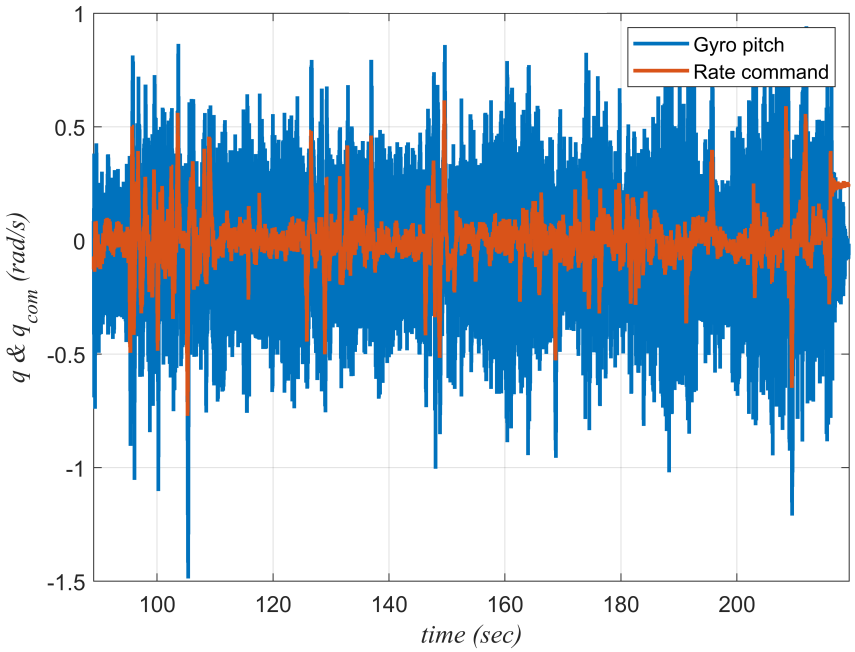

Figure 7.18: Angular rate tracking, Pitch, q

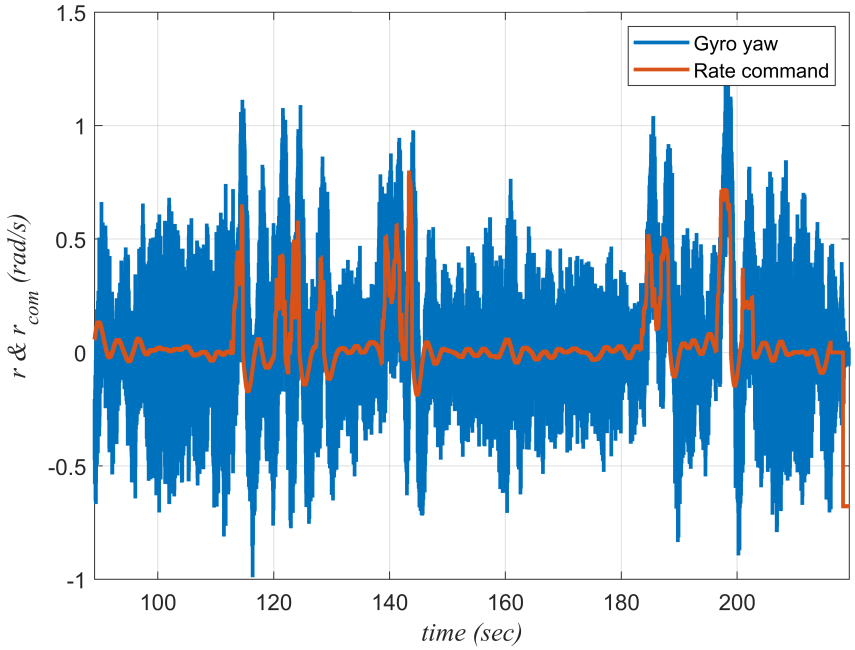

Figure 7.19: Angular rate tracking, Yaw, r

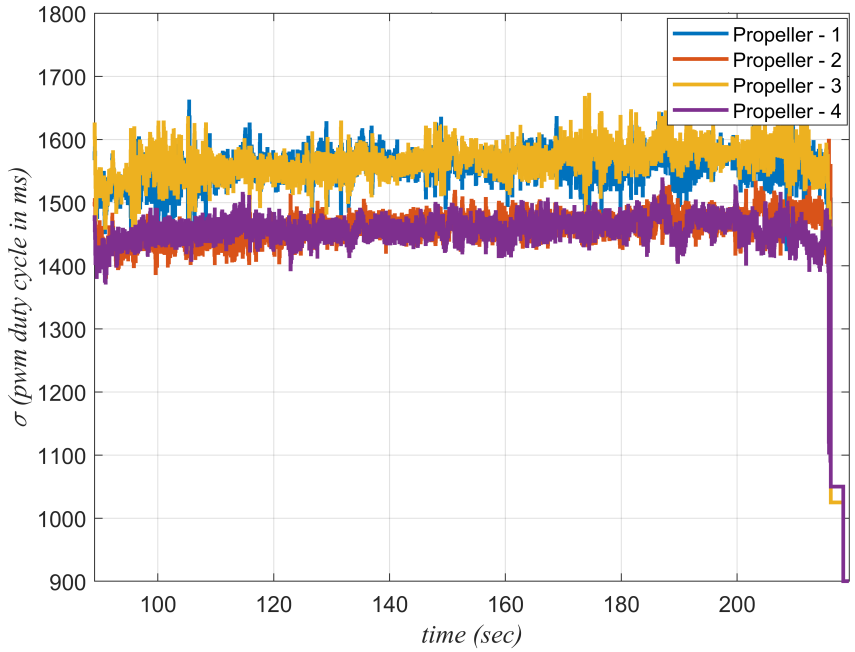

Figure 7.20: BLDC motor control throttle (throttle 1000 min, 2000 max)

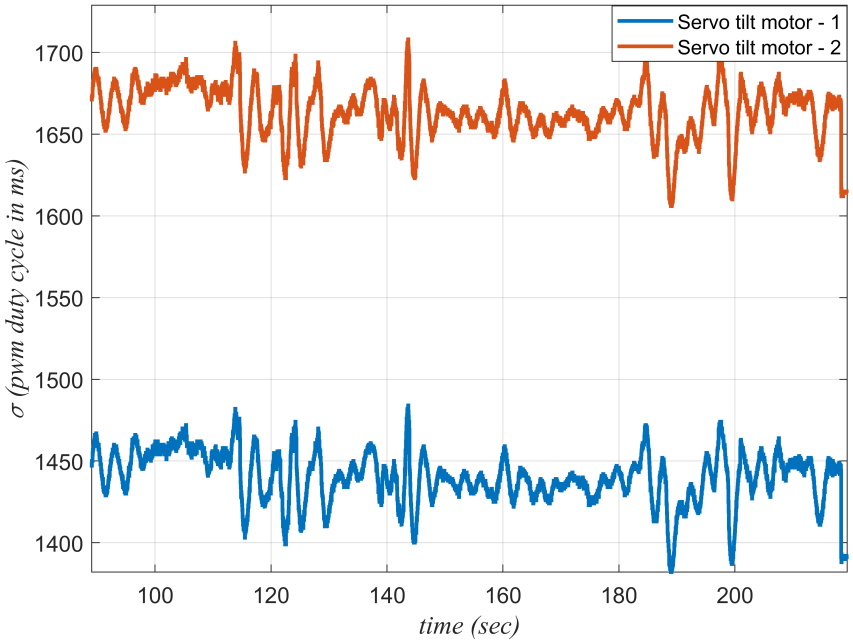

Figure 7.21: Servo tilt motor control (1000 min, 2000 max)

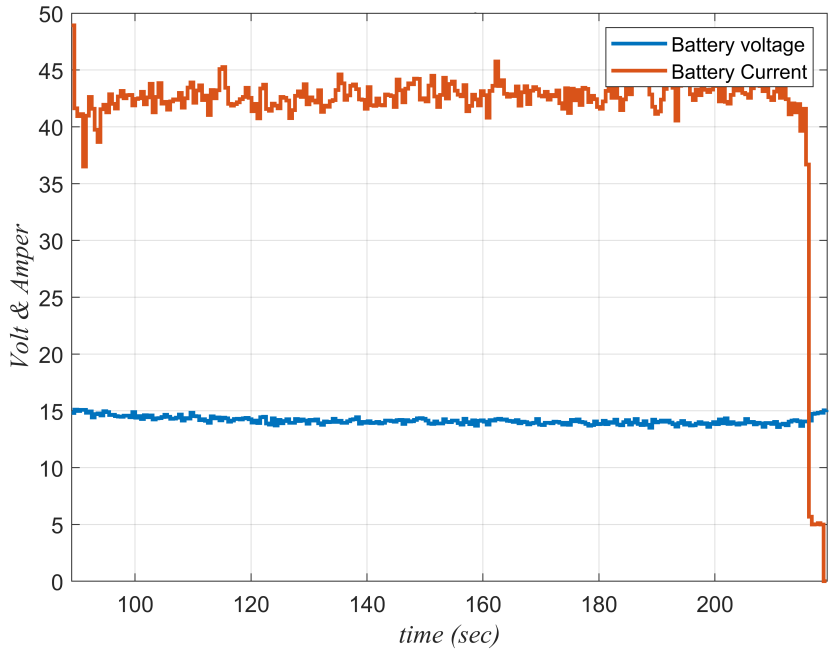

Figure 7.22: Battery

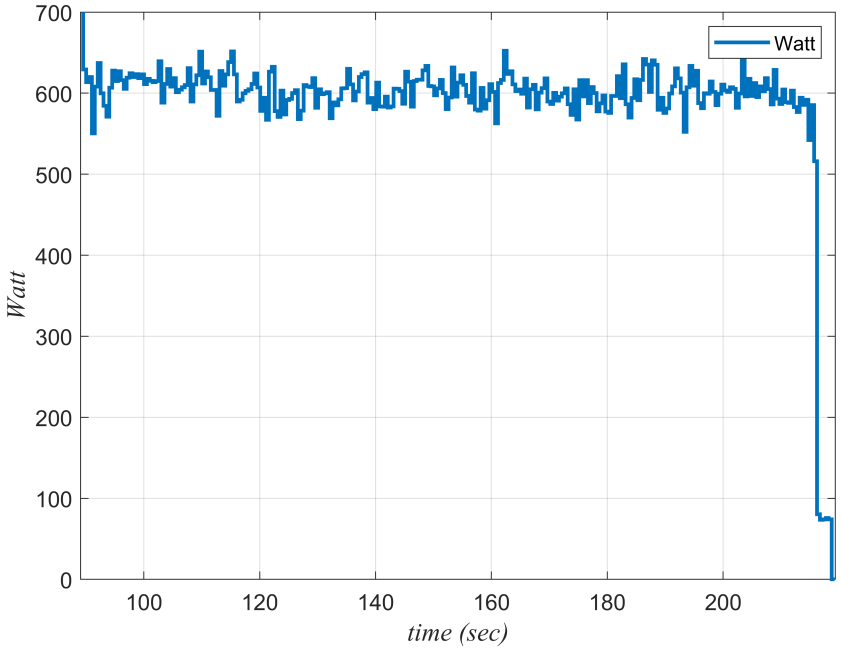

Figure 7.23: Power

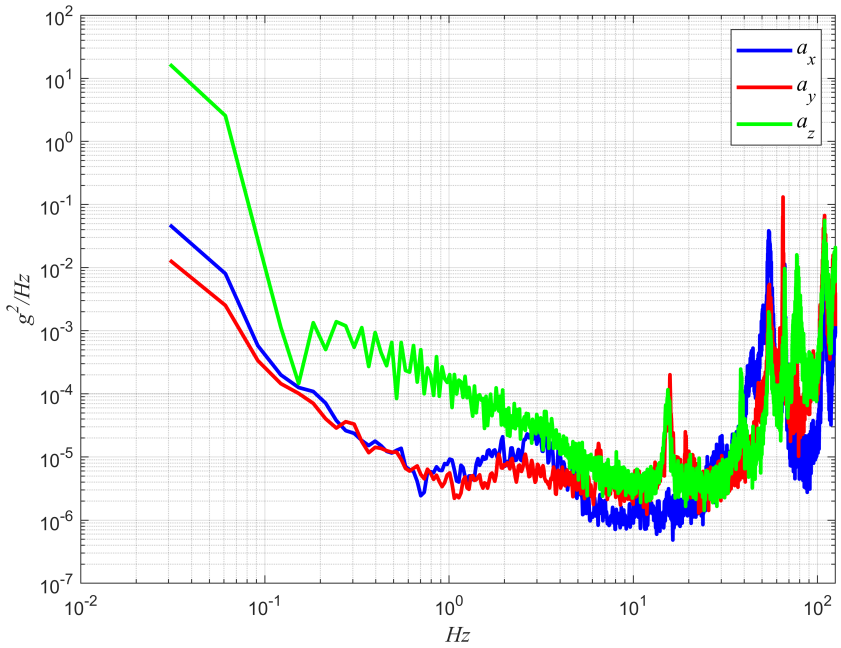

Figure 7.24: PSD Estimate of linear vibrations on vehicle

CHAPTER 8

CONCLUSION AND FUTURE WORK

8.1 Conclusion

In this study, we propose a novel, mechanically robust aircraft design aimed at efficient heavy lifting compared to other common aerial vehicles under certain width constraints. The HLAV performs the task of carrying the main load with two large propellers that are efficient thanks to the greater disk area and includes two small tilting propellers for controllability. This system has a "PPNN" (P: Clockwise, N: Counterclockwise) propeller arrangement to compensate for the reaction torques of equally sized propeller pairs placed on opposite sides. However, conventional quadcopters with the "PPNN" propeller arrangement lose their controllability upon hovering. Therefore, to ensure controllability, servo motors are integrated into the small propellers giving them the ability to tilt.

The nonlinear dynamic model of the HLAV is obtained by the Newton-Euler approach, and the system is linearized at an equilibrium point. Controllability analysis is made in the linear model and it is shown that the system is both observable and controllable. A control allocation algorithm based on the classical pseudo-inverse method has been shown to exploit only a limited range of the HLAV system's flight capabilities. A control allocation strategy based on quadratic programming has been developed to utilize HLAV capacity in maximum performance with optimal power. Open-loop system models, from virtual control to system state transfer functions are estimated using closed-loop system identification tools. High-level controllers are designed with the "loop shaping" method.

To show the feasibility of the HLAV concept, the proposed system is experimentally

verified with a newly designed prototype, and sufficient stability and trajectory tracking performance are achieved. The flight tests have shown that the HLAV is agile, stable, and very responsive to control inputs. Test results are presented.

Key contributions can be summarized as follows;

- Proposed HLAV configuration, a novel design. To the best of our knowledge, this system is unique.
- Derivation of nonlinear dynamic model and controllability analysis of the HLAV.
- A control allocation strategy based on quadratic programming for HLAV, and comparison with the pseudo-inverse method.
- A method development for cogging torque and friction identification and compensation for precise positioning of servo motors that can be used in tilt-rotors.
- Experimental flight tests and validation on the real prototype system, HLAV.

8.2 Future Work

As this prototype is scaled to larger dimensions, a more effective system will emerge for heavy lifting. However, larger sizes have a natural limit. In general, the larger the rotor size, the slower the rotor dynamic response and the lower the control agility. Fortunately, agility is not the HLAV's primary design goal, and the increased weight would help counter the wind disturbance. HLAV opens up new perspectives for the hybrid configuration, where the large propellers are powered directly by a central gasoline engine and the small rotors are battery powered. For future study, it is planned to work on a larger HLAV system, where internal combustion engine propulsion alternatives will be evaluated.

Precise positioning of servo motors that are used in tilt mechanism, is a crucial parameter for reducing vibrations in the HLAV and improve overall flight performance. In this study, it is shown that cogging torque and friction can be identified using position sensors that already exist in the tilt mechanism, so the cost of the system is not

increased. It is presented that by developing feedforward algorithms, with only cogging torque compensation, 30-65% of the tracking error can be removed in a feedback control system. In a future build of HLAV system, instead of choosing off-the-shelf servo motors, we would integrate the servo motor mechanism presented in Chapter 6 where it will be possible to design precise position control loops and apply the friction and cogging torque compensation techniques.

For the HLAV system control, nonlinear constrained control allocation methods can be studied, which is currently a highly promising area of research [20]. The main challenges for nonlinear control allocation algorithms are computationally efficient numerical implementation, verification, and validation.

REFERENCES

[1] Y. Qin, W. Xu, A. Lee, and F. Zhang, "Gemini: A compact yet efficient bi-copter uav for indoor applications," *IEEE Robotics and Automation Letters*, vol. 5, no. 2, pp. 3213–3220, 2020.

[2] H. F. Grip, D. P. Scharf, C. Malpica, W. Johnson, M. Mandic, G. Singh, and L. A. Young, "Guidance and control for a mars helicopter," in *2018 AIAA Guidance, Navigation, and Control Conference*, p. 1849, 2018.

[3] M. Hassanalian and A. Abdelkefi, "Classifications, applications, and design challenges of drones: A review," *Progress in Aerospace Sciences*, vol. 91, pp. 99–131, 2017.

[4] F. Çakıcı and K. Leblebicioğlu, "Control system design of a vertical take-off and landing fixed-wing uav," *IFAC-PapersOnLine*, vol. 49, no. 3, pp. 267–272, 2016.

[5] M. N. Boukoberine, Z. Zhou, and M. Benbouzid, "A critical review on unmanned aerial vehicles power supply and energy management: Solutions, strategies, and prospects," *Applied Energy*, vol. 255, p. 113823, 2019.

[6] G. J. Leishman, *Principles of helicopter aerodynamics with CD extra*. Cambridge university press, 2006.

[7] G. Özdoğan and K. Leblebicioğlu, "Modeling and control of a heavy-lift helicopter consisting of large and small tilting rotors," in *2018 6th International Conference on Control Engineering & Information Technology (CEIT)*, pp. 1–6, IEEE, 2018.

[8] Q. Quan, *Introduction to Multicopter Design and Control*. Springer, 2017.

[9] G. Özdoğan and K. Leblebicioğlu, "Ppnn düzenindeki dört pervaneli robot helikopterin kontrol edilebilirlik analizi," in *TORK*, Türkiye Ulusal Robotik Konferansı, 2018.

[10] C. Viswanathan, R. Longman, and P. Likins, "A degree of controllability definition-fundamental concepts and application to modal systems," *Journal of Guidance, Control, and Dynamics*, vol. 7, no. 2, pp. 222–230, 1984.

[11] G.-X. Du, Q. Quan, B. Yang, and K.-Y. Cai, "Controllability analysis for multirotor helicopter rotor degradation and failure," *Journal of Guidance, Control, and Dynamics*, vol. 38, no. 5, pp. 978–985, 2015.

[12] S. Park, J. Lee, J. Ahn, M. Kim, J. Her, G. Yang, and D. Lee, "Odar: Aerial manipulation platform enabling omnidirectional wrench generation," *IEEE/ASME Transactions on Mechatronics*, vol. 23, no. 4, pp. 1907–1918, 2018.

[13] Y. H. Tan and B. M. Chen, "Thruster allocation and mapping of aerial and aquatic modes for a morphable multimodal quadrotor," *IEEE/ASME Transactions on Mechatronics*, vol. 25, no. 4, pp. 2065–2074, 2020.

[14] H. Dong, Z. Wu, D. Chen, M. Tan, and J. Yu, "Development of a whale-shark-inspired gliding robotic fish with high maneuverability," *IEEE/ASME Transactions on Mechatronics*, vol. 25, no. 6, pp. 2824–2834, 2020.

[15] Y. Chen and J. Wang, "Design and experimental evaluations on energy efficient control allocation methods for overactuated electric vehicles: Longitudinal motion case," *IEEE/ASME Transactions on Mechatronics*, vol. 19, no. 2, pp. 538–548, 2014.

[16] Q. Tan, X. Zhang, H. Liu, S. Jiao, M. Zhou, and J. Li, "Multimodal dynamics analysis and control for amphibious fly-drive vehicle," *IEEE/ASME Transactions on Mechatronics*, vol. 26, no. 2, pp. 621–632, 2021.

[17] M. Allenspach, K. Bodie, M. Brunner, L. Rinsoz, Z. Taylor, M. Kamel, R. Siegwart, and J. Nieto, "Design and optimal control of a tiltrotor micro aerial vehicle for efficient omnidirectional flight," *arXiv preprint arXiv:2003.09512*, 2020.

[18] C. D. Pose, J. I. Giribet, and I. Mas, "Fault tolerance analysis for a class of reconfigurable aerial hexarotor vehicles," *IEEE/ASME Transactions on Mechatronics*, vol. 25, no. 4, pp. 1851–1858, 2020.

[19] W. C. Durham, "Constrained control allocation," *Journal of Guidance, control, and Dynamics*, vol. 16, no. 4, pp. 717–725, 1993.

[20] T. A. Johansen and T. I. Fossen, "Control allocation—a survey," *Automatica*, vol. 49, no. 5, pp. 1087–1103, 2013.

[21] M. Bodson, "Evaluation of optimization methods for control allocation," *Journal of Guidance, Control, and Dynamics*, vol. 25, no. 4, pp. 703–711, 2002.

[22] D. Enns, "Control allocation approaches," in *Guidance, Navigation, and Control Conference and Exhibit*, p. 4109, 1998.

[23] M. W. Oppenheimer, D. B. Doman, and M. A. Bolender, "Control allocation for over-actuated systems," in *2006 14th Mediterranean Conference on Control and Automation*, pp. 1–6, IEEE, 2006.

[24] J. Zhang, P. Bhardwaj, S. A. Raab, S. Saboo, and F. Holzapfel, "Control allocation framework for a tilt-rotor vertical take-off and landing transition aircraft configuration," in *2018 Applied Aerodynamics Conference*, p. 3480, 2018.

[25] O. Härkegård, "Dynamic control allocation using constrained quadratic programming," *Journal of Guidance, Control, and Dynamics*, vol. 27, no. 6, pp. 1028–1034, 2004.

[26] O. Harkegard, "Efficient active set algorithms for solving constrained least squares problems in aircraft control allocation," in *Proceedings of the 41st IEEE Conference on Decision and Control, 2002.*, vol. 2, pp. 1295–1300, IEEE, 2002.

[27] E. Dyer, S. Sirouspour, and M. Jafarinasab, "Energy optimal control allocation in a redundantly actuated omnidirectional uav," in *2019 International Conference on Robotics and Automation (ICRA)*, pp. 5316–5322, IEEE, 2019.

[28] T. Schneider, G. Ducard, K. Rudin, and P. Strupler, "Fault-tolerant control allocation for multirotor helicopters using parametric programming," *rN*, vol. 1, p. r2, 2012.

[29] Q. Zhang, Z. Liu, J. Zhao, and S. Zhang, "Modeling and attitude control of bicopter," in *Aircraft Utility Systems (AUS), IEEE International Conference on*, pp. 172–176, IEEE, 2016.

[30] A. Sanchez, J. Escareno, O. Garcia, and R. Lozano, "Autonomous hovering of a

noncyclic tiltrotor uav: Modeling, control and implementation," *IFAC Proceedings Volumes*, vol. 41, no. 2, pp. 803–808, 2008.

[31] Y. Li, Y. Qin, W. Xu, and F. Zhang, "Modeling, identification, and control of non-minimum phase dynamics of bi-copter uavs," in *2020 IEEE/ASME International Conference on Advanced Intelligent Mechatronics (AIM)*, pp. 1249–1255, IEEE, 2020.

[32] C. Månsson and D. Stenberg, *Model-based design development and control of a wind resistant multirotor UAV*. PhD thesis, LUND UNIVERSITY, 2014.

[33] D.-W. Yoo, H.-D. Oh, D.-Y. Won, and M.-J. Tahk, "Dynamic modeling and control system design for tri-rotor uav," in *Systems and Control in Aeronautics and Astronautics (ISSCAA), 2010 3rd International Symposium on*, pp. 762–767, IEEE, 2010.

[34] K.-J. Barsk, "Model predictive control of a tricopter," Master's thesis, Department of Electrical Engineering, Linköping University, 2012.

[35] M. K. Mohamed and A. Lanzon, "Design and control of novel tri-rotor uav," in *Control (CONTROL), 2012 UKACC International Conference on*, pp. 304–309, IEEE, 2012.

[36] J.-T. Zou, K.-L. Su, and H. Tso, "The modeling and implementation of tri-rotor flying robot," *Artificial Life and Robotics*, vol. 17, no. 1, pp. 86–91, 2012.

[37] S. Driessens and P. Pounds, "The triangular quadrotor: A more efficient quadrotor configuration," *IEEE Transactions on Robotics*, vol. 31, no. 6, pp. 1517–1526, 2015.

[38] M. E. Noudeh, "Design and control of x5 unmanned aerial robot," Master's thesis, Middle East Technical University, 2015.

[39] J. Verbeke, D. Hulens, H. Ramon, T. Goedemé, and J. De Schutter, "The design and construction of a high endurance hexacopter suited for narrow corridors*," in *2014 International Conference on Unmanned Aircraft Systems (ICUAS)*, pp. 543–551, 2014.

[40] G. Özdoğan and K. Leblebicioğlu, "Cogging torque disturbance rejection for a low-cost gimbal motor and a controller design with practical considerations," in *2019 12th Asian Control Conference (ASCC)*, pp. 486–491, IEEE, 2019.

[41] D. Titterton, J. L. Weston, and J. Weston, *Strapdown inertial navigation technology*, vol. 17. IET, 2004.

[42] F. Rinaldi, A. Gargioli, and F. Quagliotti, "Pid and lq regulation of a multirotor attitude: Mathematical modelling, simulations and experimental results," *Journal of Intelligent & Robotic Systems*, vol. 73, no. 1-4, pp. 33–50, 2014.

[43] A. Ansari, A. Prach, and D. S. Bernstein, "Adaptive trim and trajectory following for a tilt-rotor tricopter," in *American Control Conference (ACC), 2017*, pp. 1109–1114, IEEE, 2017.

[44] P. Pounds, R. Mahony, and P. Corke, "Modelling and control of a large quadrotor robot," *Control Engineering Practice*, vol. 18, no. 7, pp. 691–699, 2019.

[45] X. Zhang, X. Li, K. Wang, and Y. Lu, "A survey of modelling and identification of quadrotor robot," in *Abstract and Applied Analysis*, vol. 2014, Hindawi, 2014.

[46] H. Huang, G. M. Hoffmann, S. L. Waslander, and C. J. Tomlin, "Aerodynamics and control of autonomous quadrotor helicopters in aggressive maneuvering," in *2009 IEEE International Conference on Robotics and Automation*, pp. 3277–3282, IEEE, 2009.

[47] W. Johnson, *Helicopter theory*. Courier Corporation, 2012.

[48] R. C. Hibbeler, *Engineering mechanics: statics & dynamics*. Pearson Prentice Hall, 2016.

[49] A. Nanjangud, "Simultaneous low-order control of a nonlinear quadrotor model at four equilibria," in *52nd IEEE Conference on Decision and Control*, pp. 2914–2919, IEEE, 2013.

[50] G. Özdoğan and K. Leblebicioğlu, "Frequency response function measurement and parametric siso system modelling of a gyro-stabilized infrared electro optic gimbal system," *Transactions of the Institute of Measurement and Control*, vol. 38, no. 5, pp. 512–528, 2016.

[51] L. Ljung, "Perspectives on system identification," *Annual Reviews in Control*, vol. 34, no. 1, pp. 1–12, 2010.

[52] M. Jansson, "Subspace identification and arx modeling," *IFAC Proceedings Volumes*, vol. 36, no. 16, pp. 1585–1590, 2003.

[53] R. Pintelon and J. Schoukens, *System identification: A frequency domain approach*. Wiley. com, 2 ed., 2012.

[54] J. Schoukens, R. Pintelon, E. Van Der Ouderaa, and J. Renneboog, "Survey of excitation signals for fft based signal analyzers," *Instrumentation and Measurement, IEEE Transactions on*, vol. 37, no. 3, pp. 342–352, 1988.

[55] T. Oktay, "Performance of minimum energy controllers on tiltrotor aircraft," *Aircraft Engineering and Aerospace Technology: An International Journal*, 2014.

[56] B. Kürkçü, C. Kasnakoğlu, and M. O. Efe, "Disturbance/uncertainty estimator based integral sliding-mode control," *IEEE Transactions on Automatic Control*, vol. 63, pp. 3940–3947, Nov 2018.

[57] M. Baskin and K. Leblebicioglu, "Robust stabilization loop design for gimbaled electro-optical imaging system," *CoRR*, vol. abs/1602.06832, 2016.

[58] J. Hilkert, "Inertially stabilized platform technology concepts and principles," *IEEE Control Systems*, vol. 28, no. 1, pp. 26–46, 2008.

[59] Y. Liu, Z. Zhu, and D. Howe, "Direct torque control of brushless dc drives with reduced torque ripple," *IEEE Transactions on Industry Applications*, vol. 41, no. 2, pp. 599–608, 2005.

[60] J. Hung and Z. Ding, "Design of currents to reduce torque ripple in brushless permanent magnet motors," in *IEE Proceedings B (Electric Power Applications)*, vol. 140, pp. 260–266, IET, 1993.

[61] S. J. Park, H. W. Park, M. H. Lee, and F. Harashima, "A new approach for minimum-torque-ripple maximum-efficiency control of bldc motor," *IEEE Transactions on Industrial Electronics*, vol. 47, no. 1, pp. 109–114, 2000.

[62] H. Le-Huy, R. Perret, and R. Feuillet, "Minimization of torque ripple in brushless dc motor drives," *IEEE Transactions on industry Applications*, pp. 748–755, 1986.

[63] S. Hwang and D. Lieu, "Reduction of torque ripple in brushless dc motors," *IEEE Transactions on Magnetics*, vol. 31, no. 6, pp. 3737–3739, 1995.

[64] Z. Zhu and D. Howe, "Influence of design parameters on cogging torque in permanent magnet machines," *IEEE Transactions on energy conversion*, vol. 15, no. 4, pp. 407–412, 2000.

[65] M. Piccoli and M. Yim, "Cogging torque ripple minimization via position based characterization.," in *Robotics: Science and Systems*, 2014.

[66] H.-S. Ahn, Y. Chen, and H. Dou, "State-periodic adaptive compensation of cogging and coulomb friction in permanent magnet linear motors," in *American Control Conference, 2005. Proceedings of the 2005*, pp. 3036–3041, IEEE, 2005.

[67] B. Kürkçü and C. Kasnakoğlu, "Robust autopilot design based on a disturbance/uncertainty/coupling estimator," *IEEE Transactions on Control Systems Technology*, pp. 1–8, 2018.

[68] B. Kürkçü and C. Kasnakoğlu, "Robust temperature control of a thermoelectric cooler via μ-synthesis," *Journal of Electronic Materials*, vol. 47, pp. 4421–4429, Aug 2018.

[69] A. Bellini, S. Bifaretti, and S. Costantini, "A digital speed filter for motion control drives with a low resolution position encoder," *Automatika*, vol. 44, no. 12, p. 6774, 2003.

[70] E. Sincar, T. Balkan, and B. E. Platin, "Compensation of friction effects in gyrostabilized motion platforms," in *American Control Conference (ACC), 2015*, pp. 3242–3248, IEEE, 2015.

[71] C. H. Rivetta and S. Hansen, "Friction model of the 2.5-mts sdss telescope," in *Telescope Control Systems III*, vol. 3351, pp. 466–478, International Society for Optics and Photonics, 1998.

[72] K. Johanastrom and C. Canudas-De-Wit, “Revisiting the lugre friction model,” *IEEE control Systems*, vol. 28, no. 6, pp. 101–114, 2008.

[73] Ø. Magnussen, M. Ottestad, and G. Hovland, “Multicopter design optimization and validation,” *Modeling, Identification and Control*, vol. 36, no. 2, p. 67, 2015.

APPENDIX A

CONTROLLABILITY ANALYSIS OF PPNN PROPULSOR ARRANGEMENT

Appendix A presents the controllability analysis of the previous version of HLAV configuration. With the motivation explained in Section 1.1, the HLAV system is proposed to increase the flight time durability and payload capacity of existing solutions with robust mechanics design. Before we arrived at the HLAV system, we studied several types of vehicle structures. For example, whether we need servo motors in the HLAV system has been decided as a result of the analysis made in this chapter. The main difference between the HLAV system and the system described here is that the system does not have servo motors, so we may assume ξ_1 and ξ_2 angles as 0 and fixed. We analyze the controllability using linear analysis and checking the controllability degree. It is found that indeed the PPNN configuration with no servo motor aerial vehicle is not controllable. This result revealed the necessity of using the tilt-rotor mechanism and led to the development of the HLAV system to its current state.

A.1 Discussion

Before arriving at the HLAV system proposed in this thesis and adding the tilt mechanisms, the previous configuration we considered is given in Figure A.1.

The rotation directions of the propellers of conventional quadcopters are in the PNPN (P: clockwise, N: counterclockwise) order (See Fig. A.2). In our proposed design, the rotation order of the propellers must be PPNN. Because at the balance point in the air, the PPNN arrangement is needed for the reaction torques of the opposite large propellers and the reaction torques of the opposite small propellers to cancel each

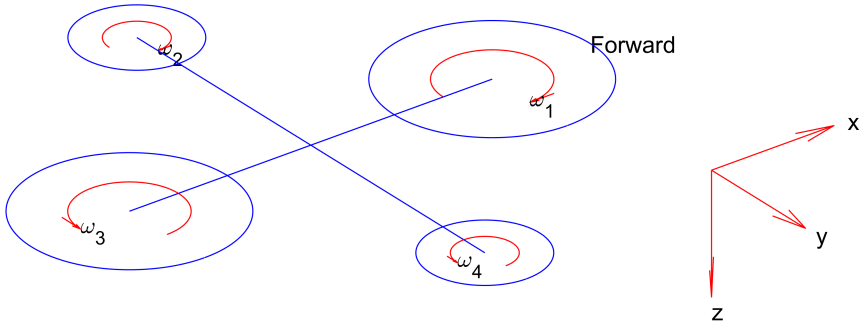

Figure A.1: Previous version of HLAV Configuration - No tilt mechanism

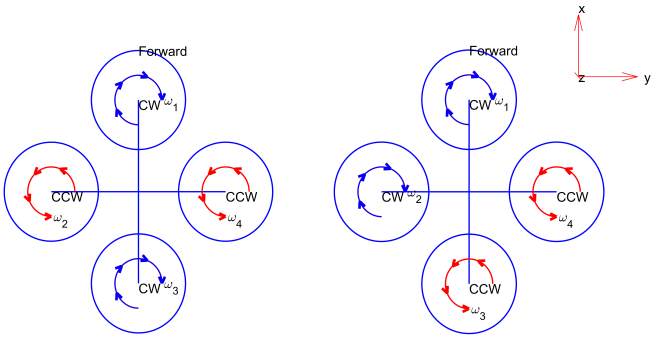

Figure A.2: Left Figure: PNPN layout, Right Figure: PPNN layout

other out.

However, when we analyzed this design with classical methods, we found that the system could not be controlled and can not hover. It is found out that the degree of controllability is 0. These results are also valid for four equally sized propeller robot helicopters. Helicopters with 'PPNN' propeller arrangement cannot be controlled without giving up an axis (e.g. yaw axis).

A.2 Controllability analysis with the classical method

In this section, the dynamic model and nonlinear equations of the system are derived, the system is linearized at the equilibrium point and the controllability matrix is obtained. We used [8, 34] resources to obtain the dynamic model.

A.2.1 Dynamic Model

We mostly follow the equations, results and assumptions presented in Chapter 2 and 3. For convenience, some of them are repeated here.

- The first propeller rotates in the positive direction with respect to the z-axis with an angular velocity of ω_1. Its position is located in the xy plane at 0 degrees from the x-axis.
- The second propeller rotates in the positive direction with respect to the z-axis with an angular velocity of ω_2. Its position is located in the xy plane, at -90 degrees from the x-axis.
- The third propeller rotates in the negative direction with respect to the z-axis with an angular velocity of ω_3. Its position is in the xy plane, 180 degrees from the x-axis.
- The fourth propeller rotates in the negative direction with respect to the z-axis with an angular velocity of ω_4. Its position is located in the xy plane at +90 degrees from the x-axis.

Propellers one and three are larger than propellers two and four, so they produce more thrust.

Below are the explanations of some of the symbols we use in the following sections;

- K_{t_b} : Thrust coefficient of big rotors ($N\,s^2/rad^2$).
- K_{t_s} : Thrust coefficient of small rotors ($N\,s^2/rad^2$).
- K_{m_b} : Torque coefficient of big rotors ($Nm\,s^2/rad^2$).
- K_{m_s} : Torque coefficient of small rotors ($Nm\,s^2/rad^2$).
- d_b : Distance between big rotor and the body center (m)
- d_s : Distance between small rotor and the body center (m)
- $\boldsymbol{C}_\alpha$: $\cos(\alpha)$, $\boldsymbol{S}_\alpha$: $\sin(\alpha)$, $\boldsymbol{T}_\alpha$: $\tan(\alpha)$

- $R_i(\alpha)$: Rotation matrix about one of the axes of a coordinate system ($i = x,\ y,\ z$) by an angle α.

The assumptions we used in modeling the air vehicle are as follows;

- Rigid body assumption for modeling
- The primary axes of the vehicle correspond to the principal axes of inertia.
- The mass is symmetrically distributed; i.e., products of inertia are considered negligible. Mass and the moments of inertia are constant; $J = \begin{bmatrix} \mathrm{I_{xx}} & 0 & 0 \\ 0 & \mathrm{I_{yy}} & 0 \\ 0 & 0 & \mathrm{I_{zz}} \end{bmatrix}$

The thrust and reaction torques of the propellers from 1 to 4 in the body frame are modeled as follows;

$$\begin{aligned} f_1^b &= \begin{bmatrix} 0 \\ 0 \\ -\mathrm{K_{t_b}}\,\omega_1^2 \end{bmatrix} \quad f_2^b = \begin{bmatrix} 0 \\ 0 \\ -\mathrm{K_{t_s}}\,\omega_2^2 \end{bmatrix} \\ f_3^b &= \begin{bmatrix} 0 \\ 0 \\ -\mathrm{K_{t_b}}\,\omega_3^2 \end{bmatrix} \quad f_4^b = \begin{bmatrix} 0 \\ 0 \\ -\mathrm{K_{t_s}}\,\omega_4^2 \end{bmatrix} \end{aligned} \tag{A.1}$$

$$\begin{aligned} M_1^b &= \begin{bmatrix} 0 \\ \mathrm{K_{t_b}}\,\mathrm{d_b}\,\omega_1^2 \\ -\mathrm{K_{m_b}}\,\omega_1^2 \end{bmatrix} \quad M_2^b = \begin{bmatrix} \mathrm{K_{t_s}}\,\mathrm{d_s}\,\omega_2^2 \\ 0 \\ -\mathrm{K_{m_s}}\,\omega_2^2 \end{bmatrix} \\ M_3^b &= \begin{bmatrix} 0 \\ -\mathrm{K_{t_b}}\,\mathrm{d_b}\,\omega_3^2 \\ \mathrm{K_{m_b}}\,\omega_3^2 \end{bmatrix} \quad M_4^b = \begin{bmatrix} -\mathrm{K_{t_s}}\,\mathrm{d_s}\,\omega_4^2 \\ 0 \\ \mathrm{K_{m_s}}\,\omega_4^2 \end{bmatrix} \end{aligned} \tag{A.2}$$

Total thrust acting on the mass center on body coordinate system is given by;

$$\begin{aligned} F_{ext}^{b} &= \sum_{i=1}^{4} F_{i}^{b} \\ &= \begin{bmatrix} 0 \\ 0 \\ -\mathrm{K}_{\mathrm{t_b}}\,\omega_1^2 - \mathrm{K}_{\mathrm{t_b}}\,\omega_3^2 - \mathrm{K}_{\mathrm{t_s}}\,\omega_2^2 - \mathrm{K}_{\mathrm{t_s}}\,\omega_4^2 \end{bmatrix} \end{aligned} \tag{A.3}$$

Total torques acting on the mass center on body coordinate system is given by;

$$\begin{aligned} M_{ext}^{b} &= \sum_{i=1}^{4} M_{i}^{b} \\ &= \begin{bmatrix} \mathrm{K}_{\mathrm{t_s}}\,\mathrm{d_s}\;(\omega_2^2 - \omega_4^2) \\ \mathrm{K}_{\mathrm{t_b}}\,\mathrm{d_b}\;(\omega_1^2 - \omega_3^2) \\ \mathrm{K}_{\mathrm{m_b}}\,\omega_3^2 - \mathrm{K}_{\mathrm{m_b}}\,\omega_1^2 - \mathrm{K}_{\mathrm{m_s}}\,\omega_2^2 + \mathrm{K}_{\mathrm{m_s}}\,\omega_4^2 \end{bmatrix} \end{aligned} \tag{A.4}$$

Euler angles of ϕ, θ, ψ describe the roll, pitch and yaw angles from body to earth coordinate system. Direction cosine matrix from body to earth is defined as;

$$\begin{aligned} C_b^e &= R_z(\psi)R_y(\theta)R_x(\phi) \\ &= \begin{bmatrix} \boldsymbol{C}_\psi\,\boldsymbol{C}_\theta & \boldsymbol{C}_\psi\,\boldsymbol{S}_\phi\,\boldsymbol{S}_\theta - \boldsymbol{C}_\phi\,\boldsymbol{S}_\psi & \boldsymbol{S}_\phi\,\boldsymbol{S}_\psi + \boldsymbol{C}_\phi\,\boldsymbol{C}_\psi\,\boldsymbol{S}_\theta \\ \boldsymbol{C}_\theta\,\boldsymbol{S}_\psi & \boldsymbol{C}_\phi\,\boldsymbol{C}_\psi + \boldsymbol{S}_\phi\,\boldsymbol{S}_\psi\,\boldsymbol{S}_\theta & \boldsymbol{C}_\phi\,\boldsymbol{S}_\psi\,\boldsymbol{S}_\theta - \boldsymbol{C}_\psi\,\boldsymbol{S}_\phi \\ -\boldsymbol{S}_\theta & \boldsymbol{C}_\theta\,\boldsymbol{S}_\phi & \boldsymbol{C}_\phi\,\boldsymbol{C}_\theta \end{bmatrix} \end{aligned} \tag{A.5}$$

We can transform the force vector to earth coordinate system as follows;

$$F_{ext}^{e} = C_b^e F_{ext}^{b} \tag{A.6}$$

$$= \begin{bmatrix} -\left(\boldsymbol{S}_\phi\,\boldsymbol{S}_\psi + \boldsymbol{C}_\phi\,\boldsymbol{C}_\psi\,\boldsymbol{S}_\theta\right)\,\Delta \\ \left(\boldsymbol{C}_\psi\,\boldsymbol{S}_\phi - \boldsymbol{C}_\phi\,\boldsymbol{S}_\psi\,\boldsymbol{S}_\theta\right)\,\Delta \\ -\boldsymbol{C}_\phi\,\boldsymbol{C}_\theta\,\Delta \end{bmatrix} \tag{A.7}$$

The following simplification term is used here.

$$\Delta = \left(\mathrm{K}_{\mathrm{t_b}}\,\omega_1^2 + \mathrm{K}_{\mathrm{t_b}}\,\omega_3^2 + \mathrm{K}_{\mathrm{t_s}}\,\omega_2^2 + \mathrm{K}_{\mathrm{t_s}}\,\omega_4^2\right)$$

A.2.2 Nonlinear Model

We would like to derive the nonlinear function $\dot{x} = f(x, u)$ where the input vector is $u \in \mathbb{R}^{4\times 1}$, and the state vector $x \in \mathbb{R}^{12\times 1}$. We derive dynamics in a hybrid frame

of reference, consisting of position and translational velocity quantities in e-frame, attitude in Euler angles, and angular rate quantities in b-frame as follows;

$$u = [\omega_1^2\ \omega_2^2\ \omega_3^2\ \omega_4^2]^T \tag{A.8}$$

$$x = [\underbrace{x^e\ y^e\ z^e}_{pos}\ \underbrace{\phi\ \theta\ \psi}_{angle}\ \underbrace{V_x^e\ V_y^e\ V_z^e}_{vel}\ \underbrace{p^b\ q^b\ r^b}_{angular\ vel}\ ]^T \tag{A.9}$$

The output vector comprises variables of particular interest that can be physically measured or are required to behave in a specific manner. In our system, we will be able to measure angular rates (p, q, r) using a gyroscope, yaw orientation (ψ^e) using a magnetometer, and earth position (x, y, z) using GPS. Then our measurement function can be defined as a 7×1 vector;

$$\begin{aligned} y &= h(x) \\ &= [x^e\ y^e\ z^e\ \psi\ p^b\ q^b\ r^b]^T \end{aligned} \tag{A.10}$$

Differential translation equations;

$$\begin{bmatrix} \dot{x} \\ \dot{y} \\ \dot{z} \end{bmatrix} = \begin{bmatrix} V_x \\ V_y \\ V_z \end{bmatrix} \tag{A.11}$$

Translation dynamic model;

$$\dot{\mathbf{V}}^e = \begin{bmatrix} \dot{V}_x \\ \dot{V}_y \\ \dot{V}_z \end{bmatrix} = \begin{bmatrix} 0 \\ 0 \\ g \end{bmatrix} + \frac{1}{m} F_{ext}^e \tag{A.12}$$

$$= \begin{bmatrix} -\frac{\left(\boldsymbol{S}_\phi \boldsymbol{S}_\psi + \boldsymbol{C}_\phi \boldsymbol{C}_\psi \boldsymbol{S}_\theta\right)\left(\mathrm{K_{t_b}}\,\omega_1^2 + \mathrm{K_{t_b}}\,\omega_3^2 + \mathrm{K_{t_s}}\,\omega_2^2 + \mathrm{K_{t_s}}\,\omega_4^2\right)}{m} \\ \frac{\left(\boldsymbol{C}_\psi \boldsymbol{S}_\phi - \boldsymbol{C}_\phi \boldsymbol{S}_\psi \boldsymbol{S}_\theta\right)\left(\mathrm{K_{t_b}}\,\omega_1^2 + \mathrm{K_{t_b}}\,\omega_3^2 + \mathrm{K_{t_s}}\,\omega_2^2 + \mathrm{K_{t_s}}\,\omega_4^2\right)}{m} \\ g - \frac{\boldsymbol{C}_\phi \boldsymbol{C}_\theta\left(\mathrm{K_{t_b}}\,\omega_1^2 + \mathrm{K_{t_b}}\,\omega_3^2 + \mathrm{K_{t_s}}\,\omega_2^2 + \mathrm{K_{t_s}}\,\omega_4^2\right)}{m} \end{bmatrix} \tag{A.13}$$

Transformation matrix between angular body rates and Euler-rates can be derived as

follows;

$$\begin{aligned}
\begin{bmatrix} p \\ q \\ r \end{bmatrix} &= \begin{bmatrix} \dot{\phi} \\ 0 \\ 0 \end{bmatrix} + R_x(-\phi) \begin{bmatrix} 0 \\ \dot{\theta} \\ 0 \end{bmatrix} + R_x(-\phi)R_y(-\theta) \begin{bmatrix} 0 \\ 0 \\ \dot{\psi} \end{bmatrix} \\
&= \begin{bmatrix} \dot{\phi} \\ 0 \\ 0 \end{bmatrix} + \begin{bmatrix} 1 & 0 & 0 \\ 0 & C_\phi & S_\phi \\ 0 & -S_\phi & C_\phi \end{bmatrix} \begin{bmatrix} 0 \\ \dot{\theta} \\ 0 \end{bmatrix} + \\
&\quad \begin{bmatrix} 1 & 0 & 0 \\ 0 & C_\phi & S_\phi \\ 0 & -S_\phi & C_\phi \end{bmatrix} \begin{bmatrix} C_\theta & 0 & -S_\theta \\ 0 & 1 & 0 \\ S_\theta & 0 & C_\theta \end{bmatrix} \begin{bmatrix} 0 \\ 0 \\ \dot{\psi} \end{bmatrix} \\
&= \underbrace{\begin{bmatrix} 1 & 0 & -S_\theta \\ 0 & C_\phi & C_\theta S_\phi \\ 0 & -S_\phi & C_\phi C_\theta \end{bmatrix}}_{R_r} \begin{bmatrix} \dot{\phi} \\ \dot{\theta} \\ \dot{\psi} \end{bmatrix}
\end{aligned} \tag{A.14}$$

We have obtained transformation matrix, R_r. Now we take the inverse of R_r to obtain euler-rates from body angular rates. Note that $R_r^{-1} \neq R_r^T$.

$$\begin{bmatrix} \dot{\phi} \\ \dot{\theta} \\ \dot{\psi} \end{bmatrix} = R_r^{-1} \begin{bmatrix} p \\ q \\ r \end{bmatrix} \tag{A.15}$$

$$= \begin{bmatrix} 1 & \boldsymbol{S}_\phi \boldsymbol{T}_\theta & \boldsymbol{C}_\phi \boldsymbol{T}_\theta \\ 0 & \boldsymbol{C}_\phi & -\boldsymbol{S}_\phi \\ 0 & \frac{\boldsymbol{S}_\phi}{\boldsymbol{C}_\theta} & \frac{\boldsymbol{C}_\phi}{\boldsymbol{C}_\theta} \end{bmatrix} \begin{bmatrix} p \\ q \\ r \end{bmatrix} \tag{A.16}$$

$$= \begin{bmatrix} p + \frac{\boldsymbol{S}_\theta \left(r \boldsymbol{C}_\phi + q \boldsymbol{S}_\phi \right)}{\boldsymbol{C}_\theta} \\ q \boldsymbol{C}_\phi - r \boldsymbol{S}_\phi \\ \frac{r \boldsymbol{C}_\phi + q \boldsymbol{S}_\phi}{\boldsymbol{C}_\theta} \end{bmatrix} \tag{A.17}$$

The orientation dynamic model can be obtained as follows (ignoring the gyroscopic

torques of the propellers);

$$\dot{\mathbf{\Omega}}^b = \begin{bmatrix} \dot{p} \\ \dot{q} \\ \dot{r} \end{bmatrix} = J^{-1}(-\mathbf{\Omega}^b \times (J\mathbf{\Omega}^b) + M^b_{ext}) \tag{A.18}$$

$$= \begin{bmatrix} \frac{\mathrm{K_{t_s}\,d_s\,\omega_2^2 - K_{t_s}\,d_s\,\omega_4^2 + I_{yy}\,q\,r - I_{zz}\,q\,r}}{\mathrm{I_{xx}}} \\ \frac{\mathrm{K_{t_b}\,d_b\,\omega_1^2 - K_{t_b}\,d_b\,\omega_3^2 - I_{xx}\,p\,r + I_{zz}\,p\,r}}{\mathrm{I_{yy}}} \\ -\frac{\mathrm{K_{m_b}\,\omega_1^2 - K_{m_b}\,\omega_3^2 + K_{m_s}\,\omega_2^2 - K_{m_s}\,\omega_4^2 - I_{xx}\,p\,q + I_{yy}\,p\,q}}{\mathrm{I_{zz}}} \end{bmatrix} \tag{A.19}$$

Here, the moment of inertia matrix J is defined as;

$$J = \begin{bmatrix} \mathrm{I_{xx}} & 0 & 0 \\ 0 & \mathrm{I_{yy}} & 0 \\ 0 & 0 & \mathrm{I_{zz}} \end{bmatrix} \tag{A.20}$$

Summing up all the equations derived above, the nonlinear model can be expressed by (A.21);

$$f(x,u) = \begin{bmatrix} \dot{x}^e \\ \dot{y}^e \\ \dot{z}^e \\ \dot{\phi} \\ \dot{\theta} \\ \dot{\psi} \\ \dot{V}_x^e \\ \dot{V}_y^e \\ \dot{V}_z^e \\ \dot{p}^b \\ \dot{q}^b \\ \dot{r}^b \end{bmatrix} = \begin{bmatrix} V_x \\ V_y \\ V_z \\ p + \frac{\boldsymbol{S}_\theta\left(r\,\boldsymbol{C}_\phi + q\,\boldsymbol{S}_\phi\right)}{\boldsymbol{C}_\theta} \\ q\,\boldsymbol{C}_\phi - r\,\boldsymbol{S}_\phi \\ \frac{r\,\boldsymbol{C}_\phi + q\,\boldsymbol{S}_\phi}{\boldsymbol{C}_\theta} \\ -\frac{\left(\boldsymbol{S}_\phi\,\boldsymbol{S}_\psi + \boldsymbol{C}_\phi\,\boldsymbol{C}_\psi\,\boldsymbol{S}_\theta\right)\varDelta_1}{m} \\ \frac{\left(\boldsymbol{C}_\psi\,\boldsymbol{S}_\phi - \boldsymbol{C}_\phi\,\boldsymbol{S}_\psi\,\boldsymbol{S}_\theta\right)\varDelta_1}{m} \\ g - \frac{\boldsymbol{C}_\phi\,\boldsymbol{C}_\theta\,\varDelta_1}{m} \\ \frac{\mathrm{K_{t_s}\,d_s\,\omega_2^2 - K_{t_s}\,d_s\,\omega_4^2 + I_{yy}\,q\,r - I_{zz}\,q\,r}}{\mathrm{I_{xx}}} \\ \frac{\mathrm{K_{t_b}\,d_b\,\omega_1^2 - K_{t_b}\,d_b\,\omega_3^2 - I_{xx}\,p\,r + I_{zz}\,p\,r}}{\mathrm{I_{yy}}} \\ -\frac{\varDelta_2 - \mathrm{I_{xx}}\,p\,q + \mathrm{I_{yy}}\,p\,q}{\mathrm{I_{zz}}} \end{bmatrix} \tag{A.21}$$

The following simplification terms are used here.

$$\varDelta_1 = \left(\mathrm{K_{t_b}}\,\omega_1^2 + \mathrm{K_{t_b}}\,\omega_3^2 + \mathrm{K_{t_s}}\,\omega_2^2 + \mathrm{K_{t_s}}\,\omega_4^2\right)$$

$$\varDelta_2 = \mathrm{K_{m_b}}\,\omega_1^2 - \mathrm{K_{m_b}}\,\omega_3^2 + \mathrm{K_{m_s}}\,\omega_2^2 - \mathrm{K_{m_s}}\,\omega_4^2$$

A.2.3 Linearization

There exist a equilibrium point in the hover position. The state and input vectors of this equilibrium point are:

$$\begin{aligned} x_0 &= (x_0\ y_0\ z_0\ 0\ 0\ \psi_0\ 0\ 0\ 0\ 0\ 0\ 0)^T \\ u_0 &= \left(\omega_{1,0}^2\ \omega_{2,0}^2\ \omega_{3,0}^2\ \omega_{4,0}^2\right)^T \end{aligned} \tag{A.22}$$

Here, $\omega_{1,0} = \omega_{3,0}$ and $\omega_{2,0} = \omega_{4,0}$. In equilibrium point, first derivatives of the states are equal to zero;

$$f(x_0, u_0) \equiv 0 \tag{A.23}$$

Then the nonlinear model given in (A.10), and (A.21) can be linearized around the equilibrium point as follows;

$$A = \frac{\partial f(x_0, u_0)}{\partial x} \quad B = \frac{\partial f(x_0, u_0)}{\partial u} \quad C = \frac{\partial h(x_0)}{\partial x} \tag{A.24}$$

with the following dynamics;

$$\dot{z} = Az + Bv \tag{A.25}$$

$$z = x - x_0 \tag{A.26}$$

$$v = u - u_0 \tag{A.27}$$

Then, A, B and C matrices are obtained as follows;

$$A = \begin{bmatrix} 0 & 0 & 0 & 0 & 0 & 0 & 1 & 0 & 0 & 0 & 0 & 0 \\ 0 & 0 & 0 & 0 & 0 & 0 & 0 & 1 & 0 & 0 & 0 & 0 \\ 0 & 0 & 0 & 0 & 0 & 0 & 0 & 0 & 1 & 0 & 0 & 0 \\ 0 & 0 & 0 & 0 & 0 & 0 & 0 & 0 & 0 & 1 & 0 & 0 \\ 0 & 0 & 0 & 0 & 0 & 0 & 0 & 0 & 0 & 0 & 1 & 0 \\ 0 & 0 & 0 & 0 & 0 & 0 & 0 & 0 & 0 & 0 & 0 & 1 \\ 0 & 0 & 0 & -\frac{\boldsymbol{S}_{\psi_0}\,\Delta}{m} & -\frac{\boldsymbol{C}_{\psi_0}\,\Delta}{m} & 0 & 0 & 0 & 0 & 0 & 0 & 0 \\ 0 & 0 & 0 & \frac{\boldsymbol{C}_{\psi_0}\,\Delta}{m} & -\frac{\boldsymbol{S}_{\psi_0}\,\Delta}{m} & 0 & 0 & 0 & 0 & 0 & 0 & 0 \\ 0 & 0 & 0 & 0 & 0 & 0 & 0 & 0 & 0 & 0 & 0 & 0 \\ 0 & 0 & 0 & 0 & 0 & 0 & 0 & 0 & 0 & 0 & 0 & 0 \\ 0 & 0 & 0 & 0 & 0 & 0 & 0 & 0 & 0 & 0 & 0 & 0 \\ 0 & 0 & 0 & 0 & 0 & 0 & 0 & 0 & 0 & 0 & 0 & 0 \end{bmatrix} \tag{A.28}$$

The following simplification terms are used here.

$$\Delta = \left(\mathrm{K_{t_b}}\,\omega_{1,0}^2 + \mathrm{K_{t_b}}\,\omega_{3,0}^2 + \mathrm{K_{t_s}}\,\omega_{2,0}^2 + \mathrm{K_{t_s}}\,\omega_{4,0}^2\right)$$

$$B = \begin{bmatrix} 0 & 0 & 0 & 0 \\ 0 & 0 & 0 & 0 \\ 0 & 0 & 0 & 0 \\ 0 & 0 & 0 & 0 \\ 0 & 0 & 0 & 0 \\ 0 & 0 & 0 & 0 \\ 0 & 0 & 0 & 0 \\ 0 & 0 & 0 & 0 \\ -\frac{\mathrm{K_{t_b}}}{m} & -\frac{\mathrm{K_{t_s}}}{m} & -\frac{\mathrm{K_{t_b}}}{m} & -\frac{\mathrm{K_{t_s}}}{m} \\ 0 & \frac{\mathrm{K_{t_s}\,d_s}}{\mathrm{I_{xx}}} & 0 & -\frac{\mathrm{K_{t_s}\,d_s}}{\mathrm{I_{xx}}} \\ \frac{\mathrm{K_{t_b}\,d_b}}{\mathrm{I_{yy}}} & 0 & -\frac{\mathrm{K_{t_b}\,d_b}}{\mathrm{I_{yy}}} & 0 \\ -\frac{\mathrm{K_{m_b}}}{\mathrm{I_{zz}}} & -\frac{\mathrm{K_{m_s}}}{\mathrm{I_{zz}}} & \frac{\mathrm{K_{m_b}}}{\mathrm{I_{zz}}} & \frac{\mathrm{K_{m_s}}}{\mathrm{I_{zz}}} \end{bmatrix} \tag{A.29}$$

$$C = \begin{bmatrix} 1 & 0 & 0 & 0 & 0 & 0 & 0 & 0 & 0 & 0 & 0 & 0 \\ 0 & 1 & 0 & 0 & 0 & 0 & 0 & 0 & 0 & 0 & 0 & 0 \\ 0 & 0 & 1 & 0 & 0 & 0 & 0 & 0 & 0 & 0 & 0 & 0 \\ 0 & 0 & 0 & 0 & 0 & 1 & 0 & 0 & 0 & 0 & 0 & 0 \\ 0 & 0 & 0 & 0 & 0 & 0 & 0 & 0 & 0 & 1 & 0 & 0 \\ 0 & 0 & 0 & 0 & 0 & 0 & 0 & 0 & 0 & 0 & 1 & 0 \\ 0 & 0 & 0 & 0 & 0 & 0 & 0 & 0 & 0 & 0 & 0 & 1 \end{bmatrix} \tag{A.30}$$

The origin of the input signal of the linear system ($v = \mathbf{0}_{4x1}$, (A.27)) is an interior point of the control constraint set. Therefore, we can apply the classical controllability techniques to the system. When we analyze the controllability and observability matrices using the "MATLAB symbolic toolbox", it is observed that the system is observable (full rank), but not controllable (not full rank).

$$\begin{aligned} \text{Rank} \begin{bmatrix} C \\ CA \\ CA^2 \\ \vdots \\ CA^{11} \end{bmatrix} &= 12 \\ \text{Rank} \begin{bmatrix} B & AB & A^2B & \dots & A^{11}B \end{bmatrix} &= 10 \\ &\neq 12 \end{aligned} \tag{A.31}$$

A.3 Degree of Controllability

Determining whether a system can be controlled by the classical method is not enough in practice by itself. The result is binary, either yes or no. However, in this system, for example, if we extended the length of one of the arms of the robot skeleton by ϵ, the system would be controllable in theory. But in practice, we would need infinite bandwidth motors and lag-free sensors to control it. So we need to measure the degree of controllability. This concept has been discussed in the literature in detail [10]. It is possible to find the degree of controllability analytically with the algorithm suggested in the reference [11]. In this section, we analyze the degree of controllability by visualizing the ACS (attainable control set).

Now we define the degree of controllability of air vehicle robots. The linear dynamic equation is given in (A.25), as $\dot{z} = Az + Bv$. Here v represents the linearized input signal. We can define a vector 12×1 with $u_f = B\,v$ where we can manipulate the state vector. The first eight elements of this vector will be zero due to the contents of matrix B given in (A.29). The 9th element controls the ascending acceleration of the system, and the 10th, 11th and 12th elements control the angular accelerations in 3 axes. In this case, we get the accelerations (1 axis translational, 3 axes rotational) that we can apply to the system with the last 4 elements (elements 9 to 12) of the vector u_f. We can define the space of these applicable accelerations with $\Gamma \subset \mathbb{R}^4$.

$$\Gamma = \{u_f(9:12) | u_f = B\,v, v \in [u_{min} - u_0,\, u_{max} - u_0] \subset \mathbb{R}^4\} \tag{A.32}$$

We assume that the elements of our input signal are in the range $u_{min} - u_0 \leq v \leq u_{max} - u_0$. We define $\partial\Gamma$ as the bounds of Γ. In this case, we can express the degree of controllability, $\rho(\partial\Gamma)$, as follows.

$$\rho(\partial\Gamma) \triangleq \min\{\|\beta\|, \beta \in \partial\Gamma\} \tag{A.33}$$

The equation (A.33) specifies a problem formulation that searches the boundaries of the acceleration space ($\partial\Gamma$) that we can apply to the system in all directions within limits. The distance of the boundary point closest to 0 is defined as the degree of controllability. The greater the degree of controllability from zero, the more controllable the system is. 0 means the system is uncontrollable. The bigger the $\rho(\partial\Gamma)$ value, the more controllable the system is. Here, the first element of Γ has the unit m/s^2 and the other 3 elements have the unit rad/s^2. Therefore, the first element needs to be normalized with respect to the other elements.

We can apply the method we described above to our system with the parameters given in Table A.1.

Equilibrium point, $u_0 = \left(\omega_{1,0}^2\ \omega_{2,0}^2\ \omega_{3,0}^2\ \omega_{4,0}^2\right)^T$ can be selected as described by (A.34). Here, the α parameter indicates that 0.85 of the total weight will be carried by large propellers and 0.15 by small propellers.

Table A.1: System parameters

Description	***Parameter***	***Assumed Value***	***Unit***
Total mass	m	3.5	kg
Principal moment of inertia	I_{xx}	0.06	kg·m^2
Principal moment of inertia	I_{yy}	0.12	kg·m^2
Principal moment of inertia	I_{zz}	0.21	kg·m^2
Distance from mass center	d_b	0.4	m
Distance from mass center	d_s	0.5	m
Thrust coefficient	K_{t_b}	8.5668e-05	N·s^2/rad^2
Torque coefficient	K_{m_b}	1.3465e-06	Nm·s^2/rad^2
Max angular velocity	$\omega_{\max_{1,3}}$	600	rad/s
Thrust coefficient	K_{t_s}	1.5133e-05	N·s^2/rad^2
Torque coefficient	K_{m_s}	1.7889e-07	Nm·s^2/rad^2
Max angular velocity	$\omega_{\max_{2,4}}$	770	rad/s

$$
\begin{aligned}
\alpha &= 0.85 \\
\omega_{1,0}^2 &= \alpha \frac{mg}{2\,K_{t_b}} \\
\omega_{2,0}^2 &= (1-\alpha) \frac{mg}{2\,K_{t_s}} \\
\omega_{3,0}^2 &= \alpha \frac{mg}{2\,K_{t_b}} \\
\omega_{4,0}^2 &= (1-\alpha) \frac{mg}{2\,K_{t_s}}
\end{aligned}
\tag{A.34}
$$

The reachable acceleration space is 4-D. For the sake of visualization, we can show the 3-axis rotational acceleration space formed by input combinations that do not create vertical acceleration of the input signals (net force is zero in the z-axis, $f_z = 0$) in 3 dimensions with Fig. A.3. As can be seen from the figure, the accessible acceleration space is a plane passing through the origin. Therefore, we do not have control authority in the directions that are not parallel to the plane. Therefore, the degree of controllability defined by (A.33) is 0.

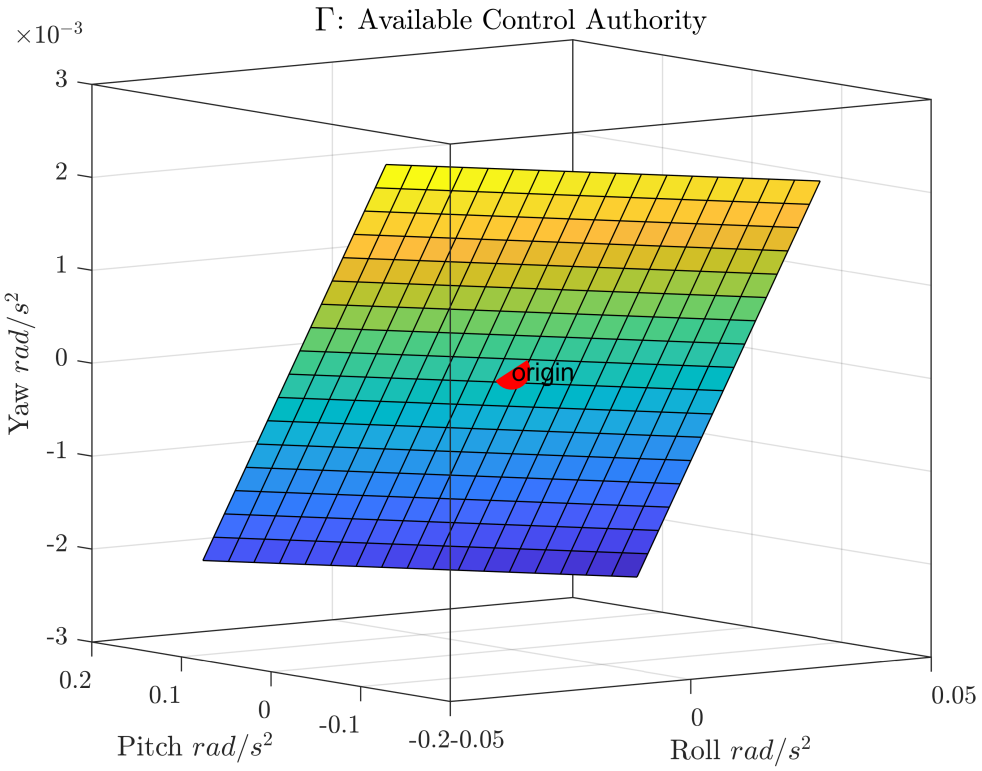

Figure A.3: PPNN Available Control Authority

CURRICULUM VITAE

PERSONAL INFORMATION

Surname, Name: Özdoğan, Gökhan
Nationality: Turkish (TC)
Date and Place of Birth: 1988, Erzincan
Marital Status: Married
E-mail: gokhan.ozdogan@metu.edu.tr

EDUCATION

Degree	Institution	Year of Graduation
MS	Electrical and Electronics Engineering, METU	2014
BS	Electrical and Electronics Engineering, METU	2011
High School	Eskişehir Fatih Fen Lisesi	2006

PROFESSIONAL EXPERIENCE

Year	Place	Enrollment
2011-present	ASELSAN/MGEO, ANKARA	Lead Design Engineer

PUBLICATIONS

Journal Publications

1. G. Özdogan and K. Leblebicioğlu, "Frequency response function measurement and parametric siso system modelling of a gyro-stabilized infrared electro optic gimbal system," Transactions of the Institute of Measurement and Control, vol.

38, no. 5, pp. 512–528, 2016

2. G. Özdoğan and K. Leblebicioğlu, "Design, modeling and control allocation of a heavy-lift aerial vehicle consisting of large fixed rotors and small tilt-rotors,". *(Under Review)*

3. G. Özdoğan and K. Leblebicioğlu, "Optimization based control allocation of a heavy-lift aerial vehicle consisting of large fixed rotors and small tilt-rotors,". *(Under preparation)*

International Conference Publications

1. G. Özdoğan and K. Leblebicioğlu, "Modeling and control of a heavy-lift helicopter consisting of large and small tilting rotors," in 2018, 6th International Conference on Control Engineering & Information Technology (CEIT 2018), IEEE, İstanbul, Turkey, 25-27 October 2018, pp. 1–6.

2. G. Özdoğan and K. Leblebicioğlu, "Cogging torque disturbance rejection for a low-cost gimbal motor and a controller design with practical considerations," in 2019, 12th Asian Control Conference (ASCC 2019). IEEE, Kitakyushu, Japan, 9-12 June 2019, pp. 486–491. *(Shimemura Young Author Prize, 1st Place)*

National Conference Publications

1. G. Özdoğan, K. Leblebicioğlu, "Cayro stabilize dört eksen gimbal yapılı elektro optik sistemin modellenmesi," 7. Savunma Teknolojileri Kongresi (SAVTEK 2014), Orta Doğu Teknik Üniversitesi Ankara, 25-27 Haziran 2014.

2. G. Özdoğan, K. Leblebicioğlu, "Gyro stabilize gimbalin frekans bölgesinde modellenmesi ve analizi," Otomatik Kontrol Türk Milli Komitesi Ulusal Toplantısı (TOK 2014), Kocaeli, 11-13 Eylül, 2014.

3. G. Özdoğan, D. Genlik, K. Leblebicioğlu, "Jeodezik koordinat pozisyon ölçümlerinden kalman süzgeci ile hedef hız kestirimi ve gimbal sisteminde uygulaması," Otomatik Kontrol Türk Milli Komitesi Ulusal Toplantısı (TOK 2016), Eskişehir, 29 Eylül - 1 Ekim, 2016.

4. G. Özdoğan, K. Leblebicioğlu, “PPNN düzenindeki dört pervaneli robot helikopterin kontrol edilebilirlik analizi,” Türkiye Robot Bilim Konferansı (TORK 2018), Boğaziçi Üniversitesi İstanbul, 12-14 Nisan 2018.

5. G. Özdoğan, K. Leblebicioğlu, “PPNN düzenindeki iki servo motorlu dört pervaneli robot helikopterin modellenmesi ve kontrolü,” 9. Savunma Teknolojileri Kongresi (SAVTEK 2018), Orta Doğu Teknik Üniversitesi Ankara, 27-29 Haziran 2018.

6. G. Özdoğan, K. Leblebicioğlu, “İki büyük iki küçük pervaneli ve iki servo motorlu ağır yük kaldıran helikopterin modellenmesi, tasarımı ve kontrolü,” Otomatik Kontrol Türk Milli Komitesi Ulusal Toplantısı (TOK 2018), Kayseri, 12-14 Eylül 2018.